2003

Manufacturing and analysis of a LIGA heat exchanger for the surface of a tube: a cooling simulation of the leading edge region of a turbine blade

Christophe Marques
Louisiana State University and Agricultural and Mechanical College, cmarque@lsu.edu

MANUFACTURING AND ANALYSIS OF A LIGA HEAT EXCHANGER FOR THE SURFACE OF A TUBE: A COOLING SIMULATION OF THE LEADING EDGE REGION OF A TURBINE BLADE

A Dissertation

Submitted to the Graduate Faculty of the
Louisiana State University and
Agricultural and Mechanical College
in partial fulfillment of the
requirements for the degree of
Doctor of Philosophy
in

The Department of Mechanical Engineering

by
Christophe Marques
Diplôme d'ingénieur en Génie Mécanique Développement, INSA de Lyon, France, 1996
M.S., Louisiana State University, 1997
May 2003

DEDICATION

In Loving Memory of

My Grand Mother Lurdes (1909-1999)

My Uncle Walter (1939-2000)

My Uncle Fernando (1942-2002)

My "American Dad" Mike (1945-2002)

ACKNOWLEDGEMENTS

During the past four years, I have found myself very fortunate. I have been surrounded with exceptional individuals who have played an upbeat role in my life academically, but more than anything else, personally. Since it is hard to mention all of them, who ever might be missing, please know that I have not forgotten you and that you also deserve my recognition!

First and foremost I feel like expressing my gratitude to Dr. Kevin Kelly, my outstanding graduate advisor / coach / mentor for having been so supportive, for inspiring me to stretch myself over my limits and for his never-ending enthusiasm.

In addition, I am privileged that Dr. Michael Tom, Dr. Sumanta Acharya, Dr. Michael Murphy, Dr. Dimitris Nikitopoulos and Dr. Srinath Ekkad accepted the invitation to be part of my committee. I thank you for all your suggestions and assistance. I would also like to show my appreciation to Dr. Gregory Gusik who was designated by the graduate school and who showed a genuine interest in my research project. I presume that if am at this stage, I must have passed all of the final requirements! For that reason I thank all my graduate committee for admitting me into their extraordinary world; the world of Doctors of Philosophy!!!!

I am grateful to the Defense Advanced Research Project Agency (DARPA) for providing the bulk of the funding for this research. I am also grateful to the Center for Advanced Microstructures and Devices (CAMD), which receives funding from the State

of Louisiana. CAMD was indispensable in carrying out certain parts of the LIGA process.

I was very privileged that my most important machining tasks were done by the great and talented Paul Rodriguez and Fred McKenzie at the Chemical Engineering Machine Shop as well as John Parker at the Mezzo Systems Inc. Machine Shop. Also I thank Barry Savoy and Ed Martins at the LSU Mechanical Engineering Machine Shop for their nice contribution.

I cannot forget that some of the companies who worked toward my project usually contributed beyond the boundaries of their expected tasks. I appreciate the special attention from Jerry Beeney at HITEC Corp., Rodney at Douglas Engineering Co., and Paul Abrahams at TSCI Corp.

For their friendly assistance on my research, I would like to thank Yohannes Desta (one of the brightest people I know), Tao Wang, Ryan Turner and David Milanes. I would also like to include goofballs Jason Tuma and Charles Becnel for contributing to a great and pleasant atmosphere in Dr. Kelly's research team.

In addition, I have received a lot of support from my close friends. Manami, Anne, Erin, Judy, Susan, Maria-Alejandra and Debbie for being so wonderful to me! Sam, Yannick, Olivier and Victor (Vive la Bourgogne!) for being some of the nicest French friends I have ever had! Luckily, the new generation of French students which now includes Lucie is maintaining a very nice mood around the halls of CEBA. My close American friends Steve, Michael and Kevin thank you so much for having been there!

Finally, I am for ever appreciative of my family. I am blessed with an exemplary mom, dad and brother. Pascal, having allowed me to be an uncle to Marie-Amélie is definitely the nicest graduation present.

TABLE OF CONTENTS

LIST OF TABLES

LIST OF FIGURES

ABSTRACT

Fabricating nickel micro heat exchangers directly on planar or non-planar metal surfaces has been demonstrated using the LIGA micromachining process. These heat exchangers can effectively control the temperature of surfaces in high heat flux applications. Of particular interest is the temperature control of gas turbine engine components. The locations in the gas turbine engine where improved, efficient cooling is required includes gas turbine blades, stator vanes, the turbine disk, and the combustor liner. In this dissertation, the primary application of interest is the use of such heat exchangers to cool airfoils such as turbine blades. In the first part of the study, the manufacturing and testing procedures of a flat configuration parallel plate micro pin fin heat exchanger are described. The pin fin array geometry investigated is staggered, with pin diameters of 500 μm, height to diameter ratios of 1.0 and spacing to diameter ratios of 2.5. Pressure loss and heat transfer experimental results for $4{,}000 \leq Re \leq 20{,}000$ are reported and a Nu-Re correlation is provided. Favorable comparisons with studies on similar pin fin patterns tested at a larger scale are revealed. The flat micro pin fin heat exchanger performance is concluded to always exceed the parallel plate (smooth channel) counterpart by a factor of 1.35 to 1.78 in the Reynolds number range studied. An analytic model based on these experimental results is described and used to make predictions for cooling effectiveness values attaining 0.72 in a gas turbine blade cooling application. In the second part of the study, the feasibility to fabricate a micro pin fin heat exchanger on a simple airfoil, with a leading edge approximated by a cylinder, is demonstrated. The

corresponding pin fin array geometry used is in-line, with pin diameters of 200 μm, height to diameter ratios of 2.5 and spacing to diameter ratios of 5. Heat transfer tests performed in a high temperature rig at gas Reynolds numbers near 10,000 are reported. Cooling effectiveness values ranging from 0.70 to 0.88 are obtained for coolant to mainstream gas mass ratios from 1% to 4 % and coolant to mainstream gas temperature ratios from 1.62 to 2.26.

CHAPTER 1 : INTRODUCTION

1.1 Background

Improving the performance of gas turbine systems has been achieved by increasing the turbine rotor inlet gas temperatures and pressures. Associated with this is an increased heat load on the turbine components. Operating temperatures are now reported at 2500°F (1350°C) [16], which is above the maximum allowable blade metal temperature of modern superalloys.

Therefore gas turbine designers have invested their efforts into two parallel research approaches. The first is the improvement in blade materials by the development of new alloys (superalloys) capable of withstanding higher temperatures and by development of thermal barrier coatings. The current state-of-the-art superalloy turbine surface temperatures are near 2100°F (1150°C) [12]. The other aspect of on-going research, which is the primary interest of the present study, is the development of more effective cooling techniques aimed at decreasing the average temperature of metal and maintain acceptable blade life and durability.

While the major goal of the turbine-cooling designer is to keep at metal at the lowest temperature possible, the following issues are of major concern: I) Minimal use of compressed coolant in order to reduce the penalty to the overall engine cycle [41]; II) A uniform airfoil temperature distribution in order to minimize internal thermal stresses, unfavorable factor to blade life span.

Consequently, different types of successful cooling schemes allowing the blade to withstand actual turbine operating temperatures have been developed.

Convective cooling and film cooling are the two major configurations in use. In the case of convective cooling, the temperature of the blade is decreased by the sole use of an internal coolant flow. The heat from the blade is passed to the coolant as it flows through intricate passages within the airfoil. For this cooling configuration, heat transfer can be augmented with devices such as ribs, pimples, pedestals and impingement jets [17]. As for film cooling, the method consists in injecting cool compressed air over the outer surface of the blade though holes or slots, which supplies a protective layer of cool fluid between the blade surface and the hot gases [44]. As depicted in Figure 1-1, the coolant supplied for film cooling is drawn from the blade internal cooling passages [43]. Therefore, this cooling method is actually a combination of external and internal (convective) cooling.

Cooling techniques, preferably internal, can be also combined with the use of thermal barrier coating materials applied to the surface of the blade, which can reduce the amount of coolant by a factor up to 8 according to many references on thermal barrier coatings [17].

In order to quantify the performance of a cooling scheme, the following figure of merit, called cooling effectiveness ε, is defined:

$$\varepsilon = \frac{T_G - T_W}{T_G - T_C}$$

Equation 1-1

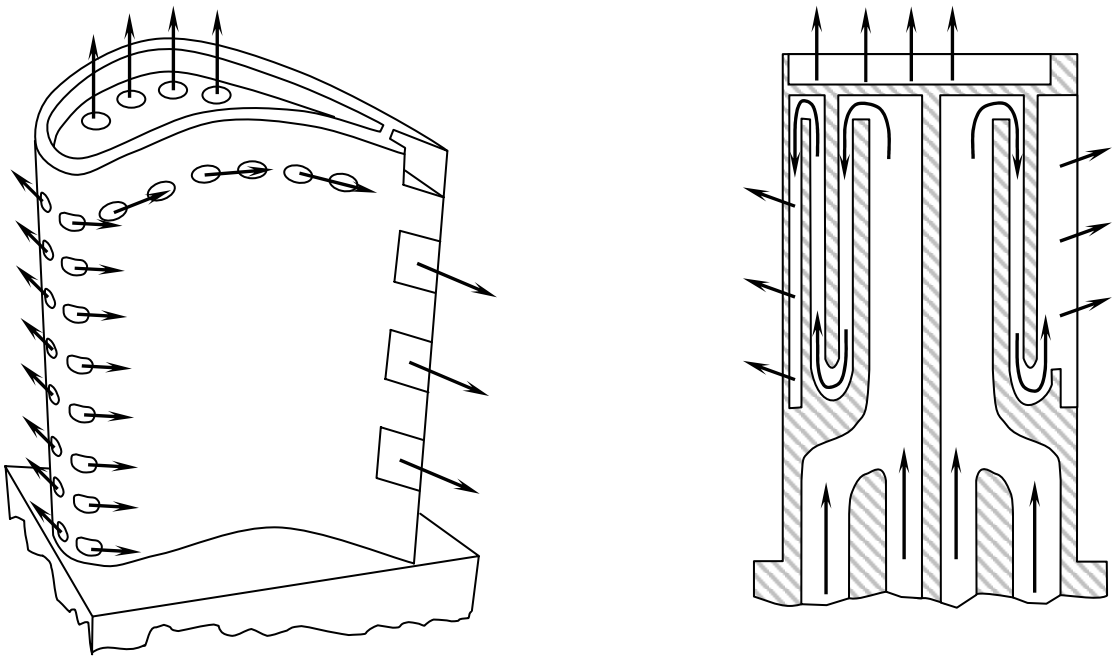

Figure 1-1: Film cooling in a turbine blade [10]

In Equation 1-1, T_G is the temperature of the hot gases flowing across the blade, T_W is the blade outer surface temperature and T_C is the inlet temperature of the compressed coolant. It appears that ε can range from 0, which is the worst cooling scheme situation when $T_W=T_G$, to 1.0, which is the best possible scenario when $T_W=T_C$. In advanced gas turbine engines, the typical value for the overall cooling effectiveness ranges from 0.3 to 0.7 [33] . Important factors influencing the cooling effectiveness are the coolant-to-hot mainstream temperature ratio T_C/T_G (associated with the coolant-to-hot mainstream density ratio), the pressure ratio P_C/P_G (associated with the mass flux ratio which is also called blowing ratio) and the geometry of the cooling scheme [16].

The counterpart to the increase of heat transfer associated with increasing complexity of internal cooling schemes is an augmentation in friction losses. This penalty has to be included in the assessment of the performance. Therefore, an overall thermal performance parameter η is defined as:

$$\eta = \frac{\left(Nu/Nu_o\right)}{\left(f/f_o\right)^{0.3}}$$

Equation 1-2

Nu and *f* are respectively average values of the Nusselt number and friction factor of the cooling scheme studied. The values with the subscripts are associated with a reference case, which can be the smooth channel configuration. Values of η greater than 1.0 mean that the geometry studied has a better performance than the reference geometry.

Companies such as Allison Advanced Development Company (AADC) and General Electric (GE) have studied advanced airfoil fabrication techniques in order to improve cooling efficiencies.

In the 1960's AADC introduced an airfoil fabrication process based on the use of Lamilloy®. As shown in Figure 1-2, this composite material is an assembly of stacked porous sheets, which is subsequently shaped to the airfoil geometry and welded. Transpiration cooling allows removing the heat from the blade. Over the years, Lamilloy® has successfully been used to manufacture exhaust nozzle liners, engine exhaust liners and several generations of airfoils.

In 1995, GE presented an unconventional airfoil fabrication process permitting the use of a "double wall" advanced cooling concept [12], [13]. This scheme, claimed to provide 15-25% reductions in cooling airfoil requirements without a rise in surface temperature, is produced using EBPVD (electron beam physical vapor deposition). This method allows the accurate positioning of cooling channels with respect to the wall of the blade. An engine turbine blade produced using this method is depicted in Figure 1-3. Another major advantage is the possibility to make each wall of the double walled airfoil with a different alloy chosen according to their respective heat load.

The "double-wall" concept introduced by G.E. and Lamilloy® introduced by AADC have been the inspiration of a research effort using LIGA micro machining techniques at Louisiana State University among the MEMS (Micro Electro Mechanical Systems) researchers. Some studies in MEMS at LSU have shown since 1997 the possible use of modified LIGA processes to manufacture microstructural devices able to enhance heat transfer on planar and non-planar surfaces in different applications [37], [38]. In particular, it was proved that pure Nickel cylindrical microstructures (or micro posts) with heights of 500 μm and diameters of 200 μm could be electroformed on the surface of a ¾ inch diameter Nickel cylinder. Such structures are shown in Figure 1-4.

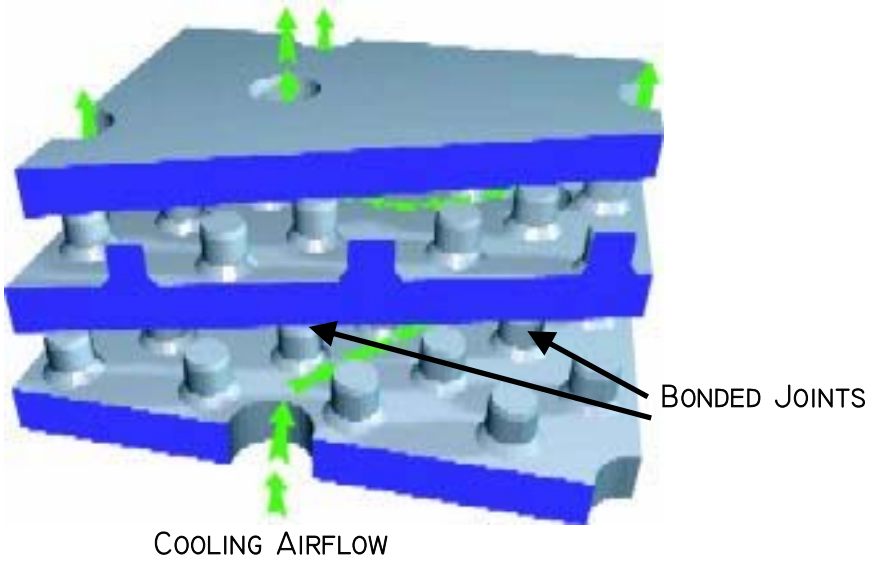

Figure 1-2: Lamilloy® concept for advanced cooling systems [19].

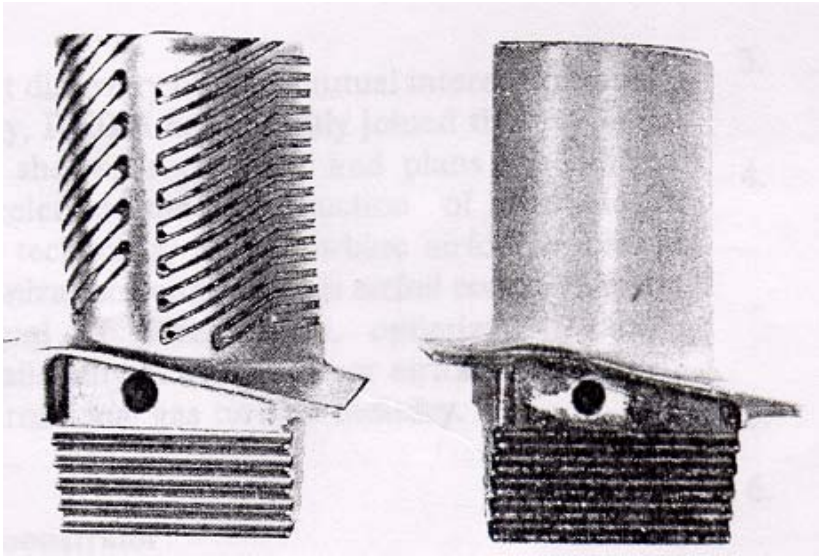

Figure 1-3: Left: Spar casting; Right: Finished blade after skin deposition [12]

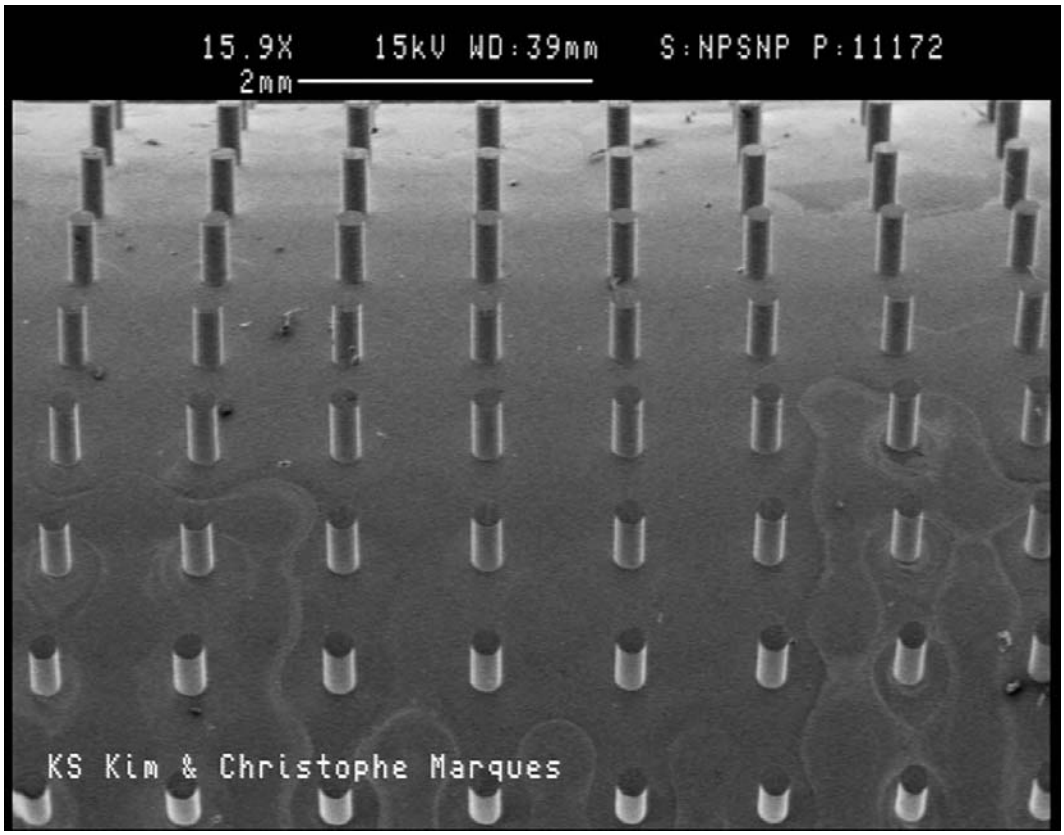

Figure 1-4: Micro posts on a tube (500 μm high, 200 μm diameter, 1000 μm spaced)

The average heat transfer coefficient on such a surface was augmented by 40% at Reynolds numbers neighboring 1100. Some work done later at L.S.U. [10] showed that it was possible to electroform a 800 μm thick shroud supported by a 500 μm high and 200 μm diameter field of micro posts on the surface of a flat plate. In many references [6],[7],[8],[9],[34],[39],[40],[42],[46], it appears that the presence of a pin fins array in a channel has the ability to enhance heat transfer greatly. That concept is already used in the internal cooling channel present in the trailing edge of some turbine blades. The reasons why fins enhance heat transfer are numerous: I) their presence increases the wetted surface area available to heat transfer; II) they promote higher turbulence levels by breaking up boundary layers which causes mixing and creates higher convective heat transfer coefficients; III) the wetted surface area associated with the fins (where the flow configuration is typically referred as “cylinder in cross-flow” by Zhukauskas [49]) is characterized by high convective heat transfer coefficients associated with the cylinder in cross flow configuration.

The interest of this study is naturally to use modified LIGA techniques to build a micro heat exchanger (a shroud supported by micro pin fins) around a cylinder, where the flow conditions simulate those taking place at the leading edge region of a turbine blade. Such a heat exchanger could be an alternative to the existing techniques in use for turbine blade cooling.

1.2 Literature Review

The purpose of this literature survey is to find research information related to the context of present study.

There are several references that deal with quantifying heat transfer and/or pressure drop across arrays of circular pin fins. Since the early 80's, a lot of conducted research has been motivated by the fact that banks of pin fins are used in the internal cooling channels at the trailing edge of turbine blades. In that case, pin fin height to diameter ratios (h/d) are usually on the order of unity due to manufacturing constraints of internally cooling turbine blades [34]. Major fundamental research studying geometrical parameters was conducted by authors such as Zhukauskas [49], Van Fossen [46], Metzer [39],[40] and Chyu [7],[8],[9]. Important geometrical parameters are:

- Pin height to diameter ratio: a study from Armstrong and Winnstanley (1987) stated that short pins fin arrays (h/d≈1) generally produce lower heat transfer than their long-cylinder counterparts ("cylinder in cross-flow").
- Array orientation (in-line or staggered): Chyu's 1990 [7] and 1999 [8] work showed that overall heat transfer coefficients were 10 to 20% higher at Re greater than 20,000 for staggered than in-line arrangements. However in-line arrays produce less pressure drop than staggered arrays. Both configurations provide higher heat transfer and pressure drop compared to a simple channel.
- Effect of fin shape: It was found by Chyu et al. (1996) that cubic or diamond-shaped pin elements are more effective for heat transfer than circular pins. It is explained that sharp edges induce excessive vortex shedding and higher turbulence mixing than circular elements [9]. Chyu's study did not make pressure drop results available.

- Effect of lateral flow ejection in pin fin channels. Lau [34] found that the Nusselt number increases with Reynolds number and decreases with as the ejection ratio increases. Friction factor has a strong dependence on ejection ratio.
- Effect of gap atop an array of fins (or partial length pin fins): Chyu [9] found that relatively low gap gives average heat transfer coefficient comparable to no gap configuration. Arora 1990 [2] found that the friction factor decreases with increasing clearance.
- Effect of channel convergence: Brigham 1984 [6] found that constant width channel configurations have lower Nusselt numbers than constant height channels. The effect is due to the change in pin fin length. In that study flow acceleration was found to have a negligible effect.

Research studies on pin fins have predominantly focused on staggered arrays with height to diameter ratios close to 1.0, spacing to diameter ratios lower than 2.5, rows numbers less than 10 and pin diameters usually greater than 5 mm. Boundary conditions are most of the time isothermal on both endwalls.

In order to compare and validate the results of the present study, a micro pin fin heat exchanger will be made with a similar pattern and design as pin fin heat exchanger which results have been reported by other authors, but with significantly smaller scale.

In all the publications, the pin length to diameter ratio is within a range where the plates (or endwalls) influence heat transfer over the pins, and vice-versa. In Chyu's work in 1990 [7] , it is mentioned that for cylinder arrays were h/d is of the order of unity, the interaction cylinder-endwall is strong. As opposed to the case with long cylinders were endwall effects are almost non-existent and where the heat transfer on the cylinder

surface dominates. Chyu describes that for crossflow over a perfectly straight cylinder, the flow characteristic near the cylinder-endwall junction is dominated by a horseshoe vortex, which produces high levels of turbulence resulting in high heat transfer in the region. In 1999 Chyu concluded that the convection heat transfer coefficient at the endwall-fluid interface is only about 10 to 20 % less than the values at the post-fluid interface and much greater, by a scale factor of about 4, than would exist if the posts were not present (in the case of parallel plates) for Reynolds numbers (based on maximal velocity and pin fin diameter) from 5,000 to 25,000.

No studies have provided any mathematical model explaining the physics of heat transfer or friction losses. This is due to the fact that for cylinder arrays were *h/d* is of the order of unity, the interaction between cylinder and endwall is very strong [7] making reliable analytical or numerical models for pin fin heat exchangers inexistent. All studies conducted present empirical heat transfer results (using the least-squares method) by curve fitting to correlations such as:

$$Nu / \mathrm{Pr}^{0.4} = A \cdot \mathrm{Re}^{B}$$

Equation 1-3

Key conclusions from the survey are as follows:

- Geometry is a crucial parameter for heat transfer and friction factors.
- Mathematical models for heat transfer or friction drag have not been developed yet for micro pin fin exchangers
- Heat transfer models are usually empirically correlated in a specific format
- LIGA has not been used for making pin fin heat exchangers for turbine blade cooling applications

- No heat exchangers with pin fin diameters lower than 1.0 mm [42] has been produced so far
- Some of the studies in the literature can be used as a source of comparison with the present study.

1.3 Research Goals

The motivation to manufacture a LIGA based heat exchanger for a turbine blade comes from: I) Our experience with the LIGA process; II) The knowledge of the fact that arrays of pin fins (such as the ones described in the previous section) can be very effective for heat transfer; III) The LIGA technology has, according to the literature survey, never been used before in this type of application; IV) Our interest to improve existing cooling schemes used for turbine blades.

The goals of the present doctoral research are proposed as follows:

- Manufacture and test a flat micro heat exchanger with a staggered array of pin fins in order to measure the overall thermal performance with respect to the Reynolds number of the coolant. The reference case is the flow through a parallel plate heat exchanger without pin fins. Those preliminary results can demonstrate the expected benefits of the micro heat exchanger.
- Customize the pin fin heat exchanger to fit the shape of a cylinder where the flow conditions approximate those at the leading edge of a turbine blade. The performance versus the Reynolds number is determined. The micro heat exchanger cooling effectiveness can be compared to that of other turbine blade cooling schemes.

To accomplish the first of these goals, a simple 5 cm x 5 cm flat channel heat exchanger with a staggered array of micro pin fins 500 μm high, 500 μm diameter and 1250 μm apart in both directions was made using a modified LIGA process. This pure Nickel heat exchanger was tested using an apparatus allowing a uniform heat flux on the top plate and a coolant flow between the plates. A similar experiment with a smooth channel (parallel plates with a gap of 500 μm and no micro pin fins) was also performed in order to validate the testing apparatus and also to provide a reference case for the calculation of the overall thermal performance. In both cases, using air as a coolant, the temperature of the top plate (at constant heat flux) and the pressure drop (at no heat flux) were determined for different ranges of coolant mass flow rates. The overall Nusselt number and the friction factor as a function of the Reynolds number are provided and compared to similar studies conducted by other authors. By using a heat transfer model and by processing the results of this experiment, the performance of this cooling scheme was determined as a function of the Reynolds number.

To satisfy the second goal, a new modified LIGA technique was developed to build a shroud around a ¾ inch tube. The shroud is supported by an in-line array of micro pin fins 500 μm high, 200 μm diameter and 1000 μm apart in both directions. A testing facility was built to quantify the performance of this heat exchanger. In the testing procedure, the heat exchanger is exposed to burner rig high temperature gases while internal cooling airflow is provided. The temperatures of the tube, the shroud, the coolant and the mainstream gases were recorded for varying mass flow rates of coolant and varying temperature of hot combustion gases. The cooling effectiveness of this heat exchanger versus coolant-to-hot mainstream mass flow rate ratio and versus coolant-to-

hot mainstream temperature ratio is determined and compared to values associated with other turbine blade cooling schemes.

The outline of this dissertation is given as follows: Chapter 2 describes the manufacturing process of the flat metal micro heat exchanger while Chapter 3 focuses on the experimental study of this heat exchanger. Chapter 4 reports the manufacturing method of the tube heat exchanger whereas Chapter 5 deals with the corresponding experimental study. Chapter 6 provides a conclusion for this doctoral study and recommendations for upcoming research.

CHAPTER 2 : FABRICATION OF THE FLAT METAL MICRO HEAT EXCHANGER

Performance tests of a flat heat exchanger such as the one described in the introduction require the manufacturing of an array of micro posts connecting two parallel plates. The process permitting the fabrication of the heat exchanger uses a modified LIGA technique developed at LSU. This fabrication process is presented in this chapter.

2.1 Design Specifications

The desired heat exchanger configuration is as depicted in Figure 2-1. A uniform heat flux is applied to the upper surface of the heat exchanger. An adiabatic boundary condition characterizes the lower surface. In the case of the pin fin heat exchanger, an array of micro posts is used to separate the parallel plates. For the comparative heat transfer case involving parallel plates without pin fins, five shims located at the corners and at the center of the heat exchanger are used as spacers. In both cases, the coolant with fully developed flow conditions is injected between the upper and lower plates.

As mentioned in the introduction, in order to compare and validate the results of the present study, the pin fin array configuration chosen here is characterized by geometric parameters similar to the values most researched and reported in the literature [7],[8],[34],[39],[40]. Typically the pin arrays are staggered with height to diameter ratios close of 1.0, spacing to diameter ratios of 2.5 in both streamwise and spanwise direction. Therefore the following parameters characterize the array studied in this chapter:

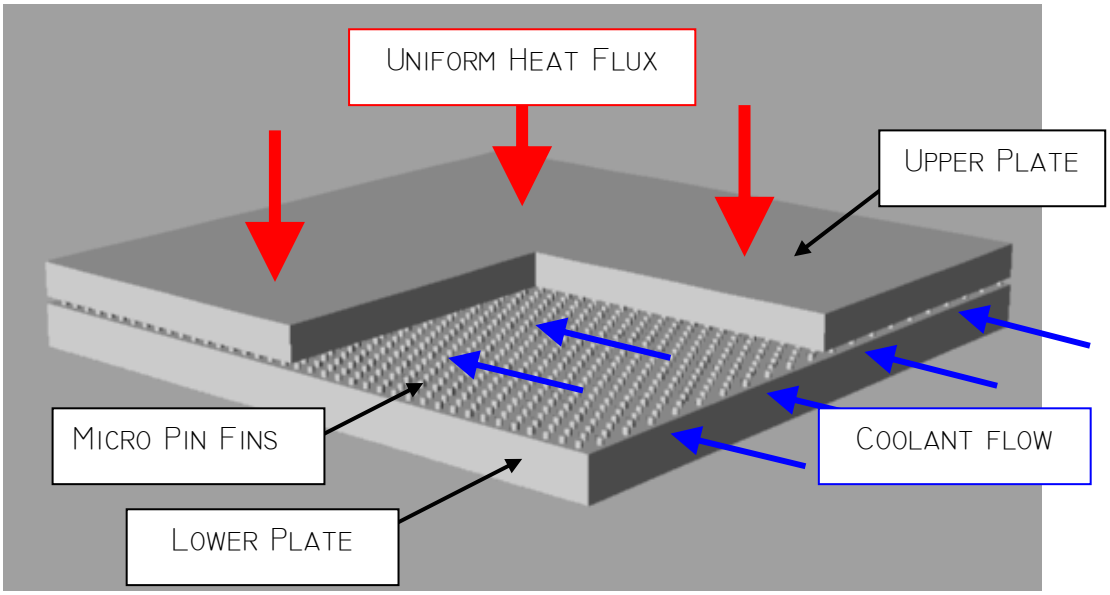

Figure 2-1: Flat metal micro heat exchanger flow configuration.

- Array arrangement: staggered
- Pin diameter: 500 μm
- Pin height: 500 μm
- Streamwise pin center-to-center spacing: 1250 μm
- Spanwise pin center-to-center spacing: 1250 μm

Limitations inherent to the X-ray exposure facility at the time manufacturing was performed, dictated that the lateral dimensions of the array be set to 5 cm (2 inches) in both streamwise and spanwise directions. Arbitrarily the upper plate and lower plate thickness were set respectively to 2.54 mm (0.1 inch) and 3.18 mm (1/8 inch).

Due to the manufacturing method used, the pin array and the top plate are a continuous metal part made of pure electroplated Nickel. The choice of Nickel as electroplated material is justified not only by its excellent mechanical and corrosion properties but also by the author's competence in Nickel electroplating. However, the upper plate used for the heat exchanger without fins is made of stainless steel 316. In both cases, with or without pins, the lower plate is made of stainless steel 316.

The following sections describe the manufacturing process that allowed creating the heat exchangers.

2.2 Overview of the Conventional LIGA Process

LIGA stands for X-ray LIthography, electroforming (German: Galvanoformung), and molding (German: Abformung). As explained in reference [37], this technology, as used at Louisiana State University (LSU), is based on bonding a sheet of poly(methyl methacrylate) (PMMA) resist to a conductive substrate [4],[5],[15], [36]. The thickness of the PMMA is typically equal to the desired height of the microstructure.

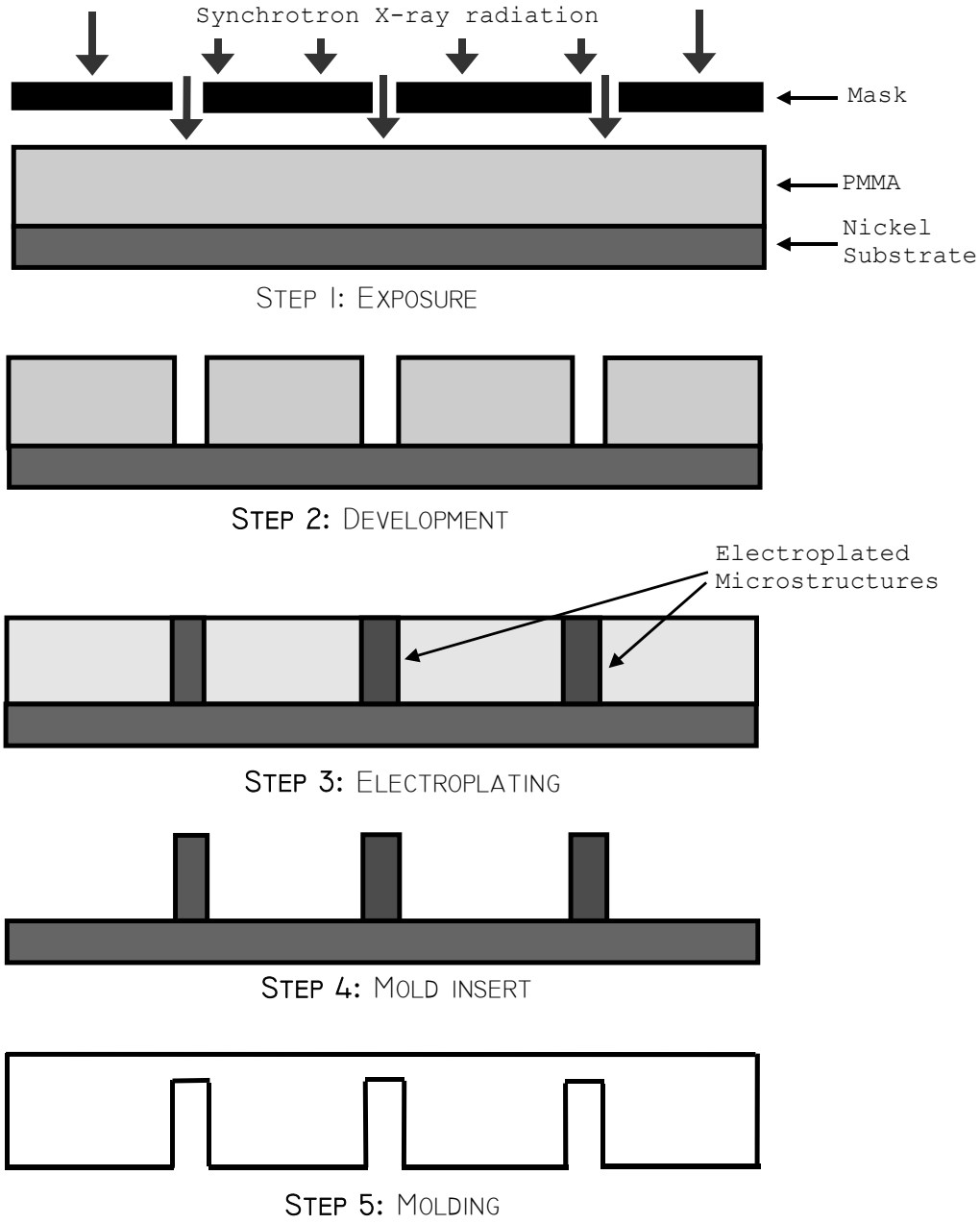

Figure 2-2: The steps of the LIGA process.

The PMMA-substrate laminate is first positioned behind a mask, and then exposed to a collimated synchrotron X-ray beam as shown in Step 1 of Figure 2-2. The molecular weight of the PMMA decreases in the irradiated areas as a result of exposure. After the PMMA sheet is exposed to the proper radiation dose, it is immersed in a developer, which selectively dissolves the irradiated areas with low molecular weights (Step 2 of Figure 2-2).

The resulting PMMA template is used to electroplate microstructures on the substrate as depicted in Step 3 of Figure 2-2. After removal of the PMMA, the metal microstructures may represent the final product (Step 4 of Figure 2-2). Otherwise, they may serve as a mold that can be inserted into an injection molding machine to repeatedly reproduce a secondary polymer template with a geometry identical to the primary PMMA template (Step 5 of Figure 2-2).

2.3 Manufacturing Procedure (Modified LIGA)

The traditional LIGA micro machining process described in Section 2.2 was modified in order to fabricate the micro heat exchanger. The modified version is summarized in Figure 2-3. A description of SU-8 photo resist, used to replace PMMA, and the manufacturing procedure steps followed to create the final product are presented in the following sub-sections.

2.3.1 The Benefits of SU-8 Resist Versus PMMA for LIGA

PMMA has been the most commonly used photo resist for deep X-ray lithography. It allows replicating microstructures with superior quality with respect to accuracy and sidewall roughness. Nevertheless, PMMA is very insensitive to X-rays

since the minimum exposure dose needed for proper development is high, which suggests that PMMA is a not a good candidate for rapid prototyping.

During the past two years, SU-8 resist (available commercially from MicroChem Corp. [24]), originally designed for UV exposure, has been proven to have comparable accuracy to PMMA for deep X-ray lithography. The main advantage of SU-8 resist is its relatively high sensitivity to X-ray radiation. SU-8 differs from PMMA by the fact that sufficient exposure generates internal cross-linking which makes the resist insoluble into SU-8 solvents. Therefore SU-8 is called a negative tone resist whereas PMMA is called a positive tone resist.

Some recent research published by CAMD researchers [29] has allowed characteristic doses of SU-8 X-ray exposure to be available in the literature. Table 2-1 shows a comparison between SU-8 and PMMA. The minimum dose that completes the cross-linking reaction so that SU-8 withstands the development is 20 J/cm^3. The minimum dose needed to completely dissolve PMMA in developer is 3500 J/cm^3, which is 175 times greater. Consequently the use of SU-8 permits the exposure time to be divided by a factor of 175. Another advantage of SU-8 is that the damaging dose to development dose ratio for SU-8 is over 500 and only 5.7 for PMMA. Therefore reaching the damaging dose is a greater concern when using PMMA than it is when using SU-8.

However, choosing SU-8 resist versus PMMA brings two major drawbacks. The first is related to handling SU-8 coated substrates. Uncontrolled exposure from the illuminating light has to be completely avoided due to the high sensitivity of the resist [29]. The second, according to Table 2-1, is that the threshold dose value above which SU-8 becomes insoluble is as low as 0.05 J/cm^3. In practice, the surface of the resist

located under the absorber layer of the X-Ray mask should never exceed the threshold dose value. Therefore, this value is a very important parameter in designing an X-ray mask for SU-8 exposure and dictates the minimal thickness of absorber layer (gold is the metal used in our case).

Table 2-1: Comparison of characteristic dose values of SU-8 and PMMA resist [29]

Resist	**PMMA**	**SU-8**
Damage dose (J/cm^3)	20,000	>10,000
Development dose (J/cm^3)	3,500	20
Threshold dose (J/cm^3)	100	0.05

2.3.2 X-ray Mask for SU-8 Exposure

Fabrication of an X-ray mask requires knowledge of the resist tone used in the subsequent LIGA steps. The choice being SU-8, a negative resist, the geometry of the absorber located on the X-ray mask should be an array of 500 μm disks (if the choice were PMMA, the mask would feature the complementary shape, an array of 500 μm holes). In addition, four "L" shaped markers are incorporated at each corner of the square pattern of micro disks. The markers will serve as a reference in positioning the electroplated sample during the final machining step and will be removed during that process.

X-ray masks are produced using UV lithography of a photoresist coated graphite membrane. Consequently, the process requires the fabrication of a UV mask for exposing the resist coated graphite. Since the photoresist used is a negative tone, the UV mask

absorber features are 500 μm absorber disks. Gold electroplating is subsequently performed inside the developed micropatterns.

The next subsections provide a description of the manufacturing stages.

2.3.2.1 Generation of a CAD Drawing for the Pattern Generator

A CAD drawing containing all the geometric coordinates of the micro patterns is created on AutoCAD. The drawing is the input to a software controlling a pattern generator. A pattern generator is a machine only capable of "flashing" UV light with rectangular patterns of limited dimension (4 μm x 4 μm minimum) and orientation onto a photosensitive plate [1]. The rectangles must title the desired shape. Even though overlapping is allowed, as few rectangles as possible should be used to minimize processing time. The 500 μm disks have been approximated by rotating 8 times, with respect to their center, rectangles with lateral dimensions of 98 μm x 490 μm. A copy of the AutoCAD drawing created and a detailed view of a micro disk approximated by overlapping rectangles are provided in Appendix A.

2.3.2.2 UV Photomask Manufacturing

The wafer used for making the UV photomask is as a 0.09 inch thick and 5 inch square soda lime glass plate, coated with a 1000 Å low reflective chrome layer and covered with 1 μm thick negative resist coating. Typically, exposure of the wafer is carried by the GCA Mann 3600 pattern generator available at CAMD. After development of the unexposed resist, the wafer is immersed in a chrome etching solution which goal is to remove the chrome uncovered by the previous development process.

Due to a UV lamp intensity calibration problem on the CAMD pattern generator, the quality of produced samples was unsatisfactory. Therefore, the photomask was created by LSI Photomask, a specialized company [21].

2.3.2.3 X-Ray Mask Substrate Preparation

The X-ray mask substrate is a laminate successively composed of a 4.5 inch diameter glass plate, a 200 μm thick round graphite sheet (available from the company Poco Graphite Inc. [25]), and 55 μm layer of SU-8 2025 resist. First, the graphite is bonded to a clean glass plate using SJR5740 spun coated 40 seconds at 3000 RPM. Baking 30 minutes at 95ºC is carried out after ramping the temperature from 60ºC and is followed by ramping the temperature down to 60ºC. Then the graphite is polished successively with 400, 600 and 800 grit polishing disks, cleaned with isopropyl alcohol and dehydrated 30 minutes in an oven at 100ºC. Finally, SU-8 2025 is spun-coated onto the graphite at 1000 RPM for 20 seconds and baked 30 minutes at 95ºC (by following the temperature ramping procedure described earlier). The 55 μm thick layer of SU-8 resist corresponds to the maximal thickness of gold absorber.

2.3.2.4 UV Exposure and Development

The ORIEL UV exposure station located at CAMD, which provides a wavelength range from 220 to 450 nm, is used as a UV light source. Prior to clamping the manufactured UV photomask plate (described earlier) and the SU-8 coated wafer together, a few drops of glycerin are inserted to fill the gap between them. The presence of glycerin ensures that air, which would cause diffraction of UV light, is completely removed. The SU-8 coated wafer is then exposed to UV with a dose of 400 mJ/cm^2 (value indicated by MicroChem Corp.) which corresponds to a 16 second long exposure

at a UV light intensity of 25 mW/cm^2. Baking for 10 minutes at 95ºC by ramping the temperature if followed by development in SU-8 developer for 5 minutes and a careful rinsing procedure. Additional details concerning SU-8 processing will be provided in Section 2.3.4.

2.3.2.5 Gold Electroplating and Finalization

The 55 μm deep cavities created by the previous exposure and development are partially filled with gold by electroplating in Techni Gold 25E (a ready to use gold plating solution available from Technic Inc.). Pulse current electroplating is performed with the conditions given in Table 2-2, at a plating rate of approximately 3 to 4 μm per hour. A thickness of gold ranging from 33 to 40 μm was produced by 9 hours of electroplating. Immersion in acetone is used to debond the gold plated graphite from the 4.5 inch glass plate.

Using JB weld glue, the graphite sheet is finally mounted and attached to an aluminum ring, producing an X-ray mask with dimensions compatible with the CAMD X-Ray exposure beamlines.

Table 2-2: Gold electroplating conditions.

Temperature	pH	Agitation	Current cycle	Current density	Polarity	Operating mode
45°C	6.0	Medium	100 ms ON 100 ms OFF	2 mA/cm^2	Negative	Galvanostatic

2.3.3 Substrate Preparation

The substrate is the conductive material onto which Nickel parts are electroformed. The thickness and diameters of the substrate are respectively 0.25 inch

and 4.5 inch. The material used is stainless steel 316, a relatively inexpensive metal. Manufacturing costs are also kept minimal by the fact that the Nickel parts are released from the substrate at the end of the process which allows recycling the stainless steel.

The two criteria needed for preparing the substrate are the following:

1. The bond between the Nickel parts and the substrate has to be strong enough to prevent internal stresses built into the growing metal from detaching the Nickel from the stainless steel substrate. Increasing the surface roughness by sandblasting can contribute to this condition.
2. At the same time, the bond between the Nickel parts and the substrate needs to be weak enough for the Nickel parts to be released easily from the substrate at the end of the process. This means that the use of a Wood Strike bath, which typically insures a strong bond between Nickel and stainless steel, is not advisable in this case.

In order to fulfill the two conditions above, the following procedure has been established:

- Surface grind both sides of the substrate (to ensure flatness)
- Sandblast the surface of interest (in order to increase roughness)
- Soak in ultrasonic bath with diluted detergent (for soil removal)
- Rinse successively with tap water, de-ionized water, acetone, de-ionized water and isopropyl alcohol
- Dehydrate the sample 30 minutes in a convection oven at 80ºC.

The prepared substrate is placed in a protective container until the SU-8 casting step is started.

2.3.4 SU-8 Casting

Prior to X-ray exposure, the resist is bonded onto the surface of the substrate in a UV filtered light environment. SU-8 resist can be purchased from MicroChem Corp. [24] among a choice of solutions with different viscosities depending on the desired spun-coated film thickness. Once SU-8 is applied onto the substrate, a pre-baking step is required to evaporate the solvents and turn the resist into a solid (step 1, Figure 2-3).

The desired thickness of SU-8 resist is 500 μm which corresponds to the height of the microstructures. Typically, SU-8 samples with a thickness lower than 800 μm can be created by single or multiple spin-coating [29]. However, due to the weight of the stainless steel substrate, spin-coating cannot be considered. A SU-8 casting apparatus which allows producing samples attaining thickness values neighboring 3000 μm has been manufactured. The apparatus permits the use of heavy substrates and simplifies multiple spin-coating procedures into a one step process.

The casting apparatus showed in Figure 2-4 is utilized as follows. A 1 cm thick, 10 cm in diameter PVC ring and the prepared stainless steel substrate are clamped between two aluminum plates. The upper plate has a 3.5 cm diameter through hole. The lower plate is anchored to an aluminum block in which a cartridge heater and a thermocouple haves been imbedded. A temperature controller connected to the cartridge heater and the thermocouple maintains the temperature of the aluminum block constant.

Once the temperature displayed by the controller attains the programmed value of 105ºC, an excess amount of NANO™ SU-8 2075 photo resist is poured onto the middle of the stainless steel plate. A protective glass cover is placed and remained onto the top plate during the 20 hour long baking process.

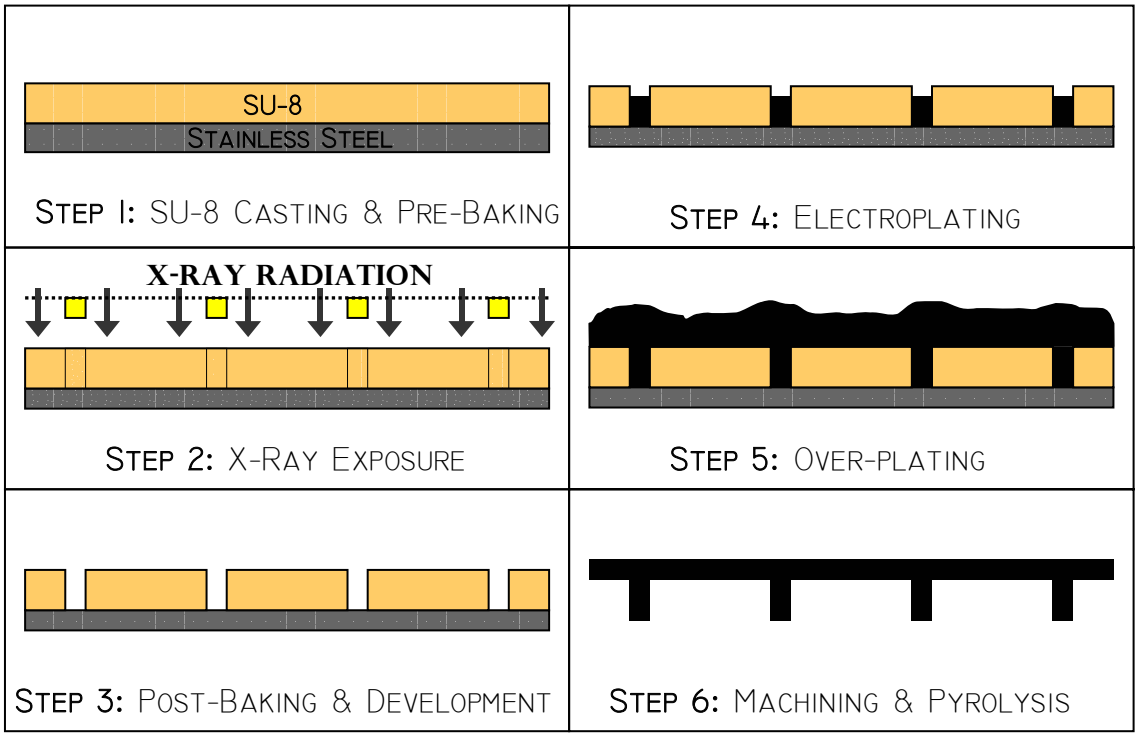

Figure 2-3: A modified version of the LIGA manufacturing process

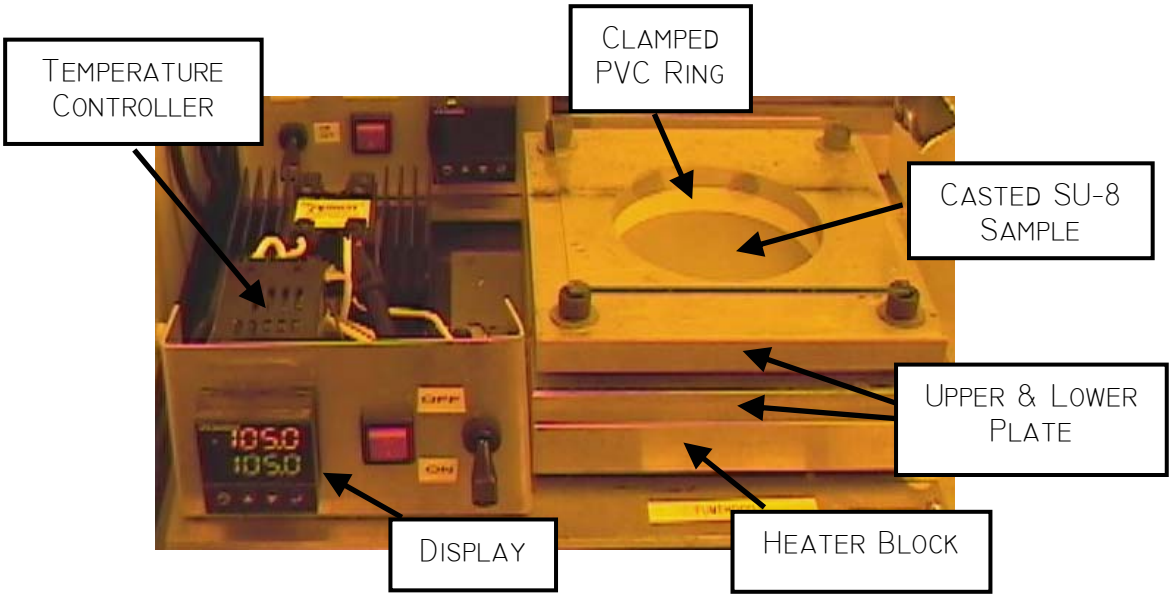

Figure 2-4: SU-8 casting apparatus

Subsequently, the SU-8 coated stainless steel substrate is disassembled from the casting apparatus and separated from the PVC ring.

The final step of SU-8 casting consists in reducing the thickness of the post baked SU-8 to the desired value. Two options are possible:

1. Use the CAMD fly cutting machine.
2. Using the Mezzo Systems, Inc. machine shop which lathe or CNC milling machine can be set up for thinning SU-8 coated samples [23].

In the fabrication of the pin fin heat exchanger, the second option was used and produced a SU-8 thickness of 500±8 μm.

2.3.5 SU-8 Exposure

The SU-8 coated stainless steel substrate was lithographically patterned at the Center for Advanced Microstructures and Devices (CAMD), an electron storage ring operating since 1993 and optimized for X-ray lithography (step 2, Figure 2-3).

As explained in Section 2.3.1, in order to ensure a good quality exposure, two important requirements have to be met. The first requirement is that the minimum dose of energy absorbed in the exposed regions exceeds 20 J/cm^3. This minimum absorption dose in exposed regions will allow complete cross-linking in the subsequent step of LIGA. The second requirement is that the side of the SU-8 which is located under the gold absorber does not exceed 0.05 J/cm^3 the threshold dose value for SU-8.

The total amount of radiation that needs to be applied to the sample can be calculated using available computer programs such as DoseSim. The code used in these programs incorporates models based on the law of absorption of radiant energy. SU-8 was exposed at CAMD with the XRLM-3 beamline, when the energy was 1.3 GeV. The

scan length was 2.5 inches, which was purposely set to a greater value than the lateral dimensions of the SU-8 resist in order to ensure full coverage of the mask. For a thickness of 500 μm, the required dose is 52 mA*min/cm. Therefore the total dose was 330 mA*min for 2.5 inches of scan length and represented approximately 3.3 min of exposure for an average storage ring current of 100 mA. According to the computer program, the maximal dose absorbed under the Gold absorber is 0.017 J/cm^3 which meets the second exposure requirement for SU-8.

After exposure was completed the sample was sheltered from ambient light inside a container wrapped in aluminum foil.

2.3.6 SU-8 Post Exposure Baking and Development

Post exposure baking is essential to complete the cross-linking reaction within the SU-8 resist and critical to the ultimate quality of the microstructures [24] (step 3, Figure 2-3).

Therefore, the SU-8 coated substrate was placed in a convection oven preheated to 65°C. The temperature was first ramped up to 95°C, maintained at this value for 22 minutes and then ramped down to 65°C. The reason for a gradual change in the surrounding temperature is to ensure that minimal internal stresses are created within the resist. Finally the sample was removed from the oven and allowed to cool to room temperature.

Since SU-8 is a negative resist, the development consists in dissolving the regions that were unexposed to radiation during the X -Ray lithography step. The solvent used is NANO™ SU-8 Developer manufactured by MicroChem Corp. [24].

Immersion time is a function of the thickness of resist. For a 500 μm sample 50 minutes are sufficient. Subsequent soaking in isopropyl alcohol allows rinsing SU-8 developer. It also allows visualizing the eventual presence of SU-8 residues which would be turned into a white color by isopropyl alcohol. If development were incomplete, the sample would directly be immersed again in NANO™ SU-8 Developer. Finally the sample is rinsed with de-ionized water and dehydrated at 80˚C in a convection oven for 30 minutes. There is no longer the need to protect the sample from white light illumination.

The developed sample is protected until the electroplating step.

2.3.7 Nickel Electroplating

Fundamentals of electrochemistry are beyond the scope of this dissertation and will not be covered. However, an overview covering principles of electroplating can be found in reference [37]. This section will only provide the electroplating procedure.

2.3.7.1 Pre-electroplating Procedure

Typically the sample has to be arranged prior to electroplating. Preparation involves I) anchoring an electrical connection to the substrate II) insulating the entire conductive surface of the substrate from the electroplating solution with the exception of the SU-8 holes III) vacuuming the air located in the SU-8 micro features. In order to eliminate leakage problems and simplify the sample preparation procedure, a sample holder and a vacuum plate have been designed and built. The corresponding pictures and description are supplied in Appendix B. The benefits from the sample holder are given as follows:

1. Reliable electrical connection to the electroplating setup

2. Accurate control of the total plating surface area
3. Adaptability to variable thickness of SU-8 coated substrates
4. Use of electroplating masking tape is eliminated or minimal
5. Vacuum is only applied to the top surface of the holder, in cavity where the sample is located. This reduces vacuuming time and eliminates the need for a voluminous vacuum vessel that would accommodate all the parts.

After placing the SU-8 coated substrate into the holder, the outer surfaces of the assembly are cleaned with isopropyl alcohol in order to minimize further contamination of the plating bath.

At this stage, the SU-8 patterns are filled with air, which is an obstacle to electroplating. In order to remove the air, the SU-8 sample located in the recess of the substrate holder is covered with a low surface tension solution made of 5 g/l of lauryl sulfate. Once the cavity is half filled with the solution and covered with the vacuum plate, the air trapped into the SU-8 holes is removed with a vacuum pump and replaced with lauryl sulfate solution. Applying 4 vacuum cycles instead of just 1 and shaking the holder can ease air removal significantly.

2.3.7.2 Electroplating Procedure

The electrolyte is a 6-liter Nickel sulfamate bath [3] composed of Nickel sulfamate and Boric acid with Lauryl sulfate sodium salt, a wetting agent, as single additive. The composition of the electroplating bath, which is given in Table 2-3, was optimized in order to minimize internal stresses within the range of current densities used. Operating conditions during the electroplating process are summarized in Table 2-4.

After filtering and setting the pH of the solution, the sample holder is placed into the bath carefully. The stainless steel substrate is the working electrode. A titanium basket filled with sulfurized Nickel noodles (and covered with a cotton pocket in order to prevent breakdown particles from depositing in the solution) serves as counter electrode. The connections are wired to a general-purpose potentiostat (Amel Instruments, Model 2051). A transparent cover is placed onto the bath to prevent electrolyte evaporation during the electroplating process.

Table 2-3: Composition of the Nickel sulfamate bath.

Compound	Formula	Concentration (g/l)
Nickel sulfamate	$Ni(SO_3NH_2)_2 \cdot 4H_2O$	450
Boric acid	H_3BO_3	37.5
Lauryl sulfate, sodium salt	$C_{12}H_{25}O_4SNa$	3

Table 2-4: Nickel sulfamate electroplating conditions.

Temperature	pH	Agitation	Filter porosity	Current density	Polarity	Operating mode
55°C	4.0	300 RPM	1.6 μm	20 mA/cm^2	Negative	Galvanostatic

Like in the case of gold electroplating, the total surface to electroplate is 3.16 cm^2. To keep the value of the current density to 20 mA/cm^2, the electroplating current is set to 63 mA. By assuming a 100% efficient electroplating process, it is possible to relate the thickness h (in μm), time t (in minutes) and current density j (in mA/cm^2) of the electroplated deposit using the relation $t*j = 47.61*h$ [37]. Therefore 20 hours is an estimation of the time necessary to fill the micro patterns (step 4, Figure 2-3).

After approximately 20 hours of electroplating, pure Nickel has filled the SU-8 features. Then electroplated metal starts growing in all directions like mushrooms as shown in Figure 2-5 over the upper surface of SU-8. The over-plating process, which is inspected visually using a bore-scope, causes the area of the working electrode to increase. To maintain the current density to the desired value, the total current is gradually increased to the final value of 500 mA which corresponds to a surface area of 25 cm^2 (a 5 cm x 5 cm square). The electroplating process is sustained for six days in order to build over-plated material exceeding the thickness of 2.54 mm, the value set in the heat exchanger specifications (step 5, Figure 2-3).

At the end of the electroforming process, the sample is removed from the holder and stored until further processing is started.

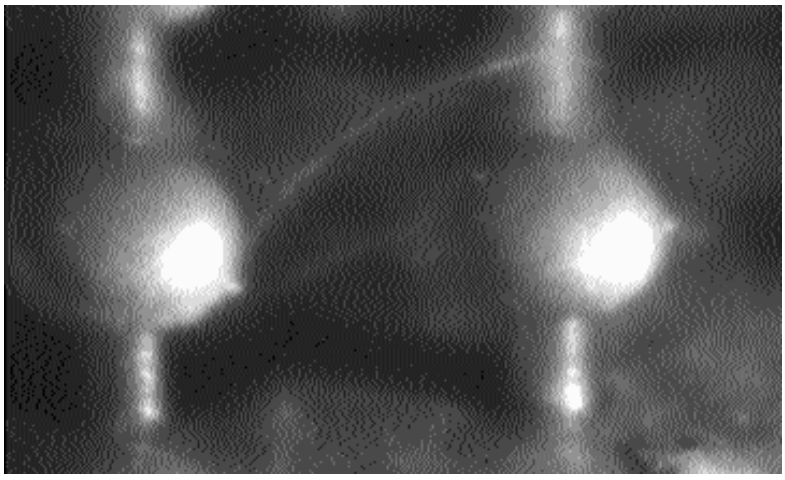

Figure 2-5: Mushrooms shaped microstructures

2.3.8 Post Processing Steps

The sample is processed to its final state according to the following two steps (step 6, Figure 2-3):

2.3.8.1 Machining

First, the electroplated part of the sample is carefully de-anchored from the stainless steel substrate. The SU-8 resist layer remains part of the sample in order to protect the microstructures. The over-plated layer of metal is machined by a skilled technician using a CNC milling machine. The overall thickness and lateral dimensions of the sample are reduced to the specifications of the heat exchanger.

2.3.8.2 SU-8 Removal

Exposed and post baked SU-8 resist is extremely difficult to strip [24]. At this stage, pyrolysis is the only SU-8 removal method found to be successful. In order to this, the electroplated sample was placed in an oven. The temperature was ramped from 25ºC to 500ºC, maintained at 500ºC for one hour and then ramped down to 25ºC.

Pictures and measurements of the sample were taken. Results are presented in the next section.

2.4 Results

Pictures of the Nickel micro pin fin heat exchanger have been produced with a stereo microscope. Figure 2-6 and Figure 2-7 show respectively an overall and detailed view of the micro posts. Figure 2-8 displays a 3-D tilted view of the microstructures.

Using a Nikon optical microscope, the height, diameter and spacing of the micro post have been measured. The overall dimensions of the sample found using a micrometer and a digital caliper are compiled in Table 2-5. Relative roughness (based on

the hydraulic diameter of the micro channel which is twice the height) is estimated to be lower than 0.001.

Table 2-5: Final dimensions of the flat micro pin fin heat exchanger

Feature	pin height	pin diameter	x axis post spacing	y axis post spacing	overall thickness
Dimension (µm)	500	500	1250	1250	2540
Tolerance (±%)	3	1.5	0.4	0.4	1.5

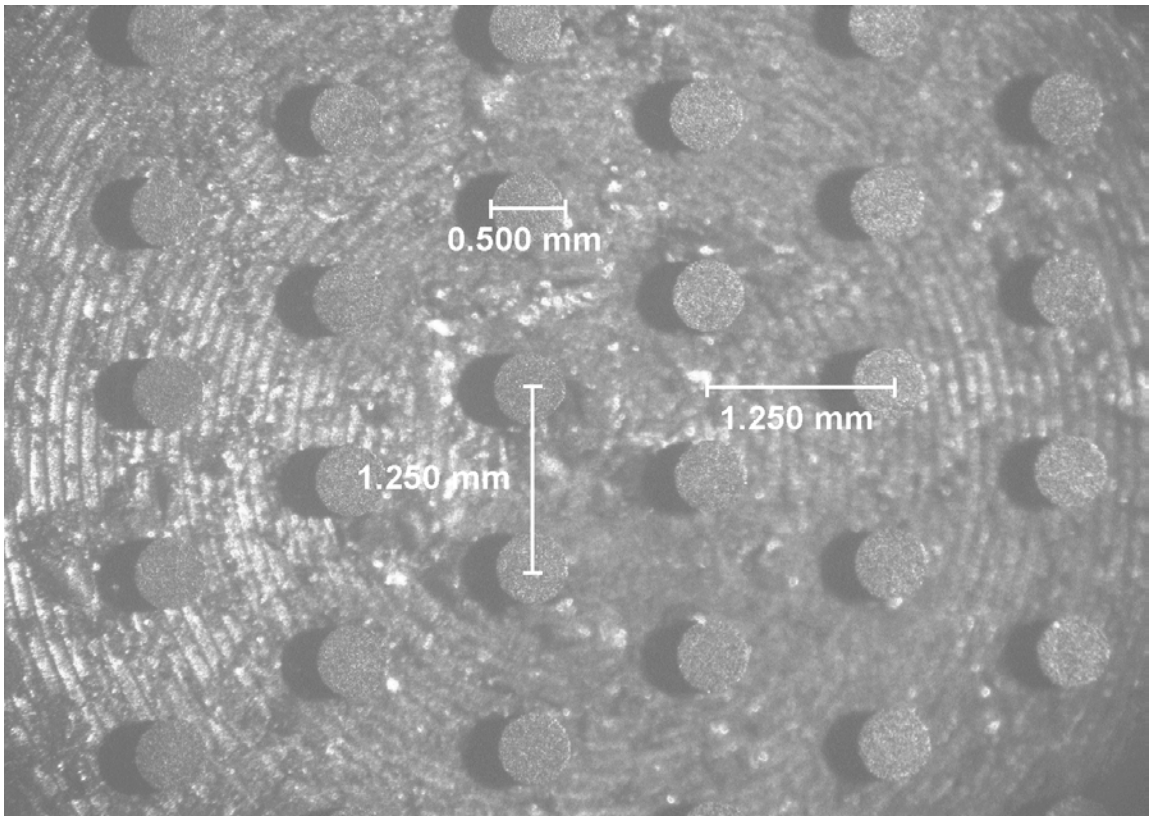

Figure 2-6: Overall view of the Nickel micro pin fin heat exchanger

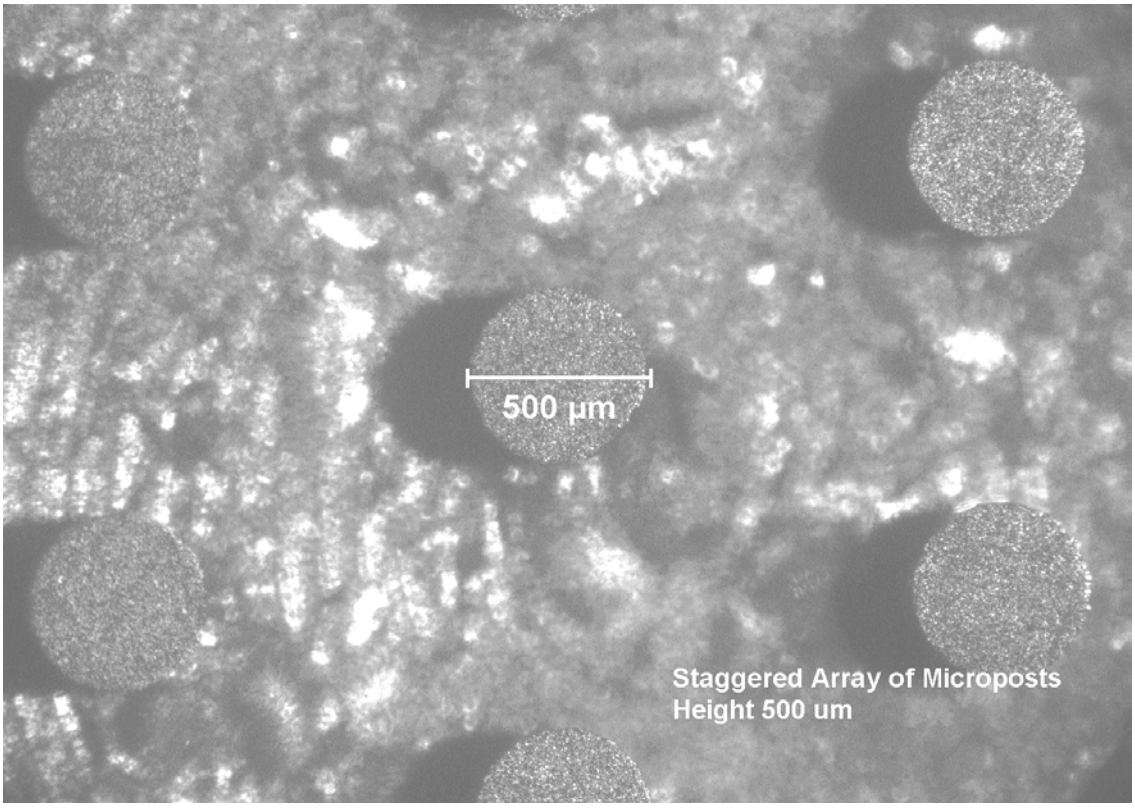

Figure 2-7: Detailed view of the Nickel microstructures

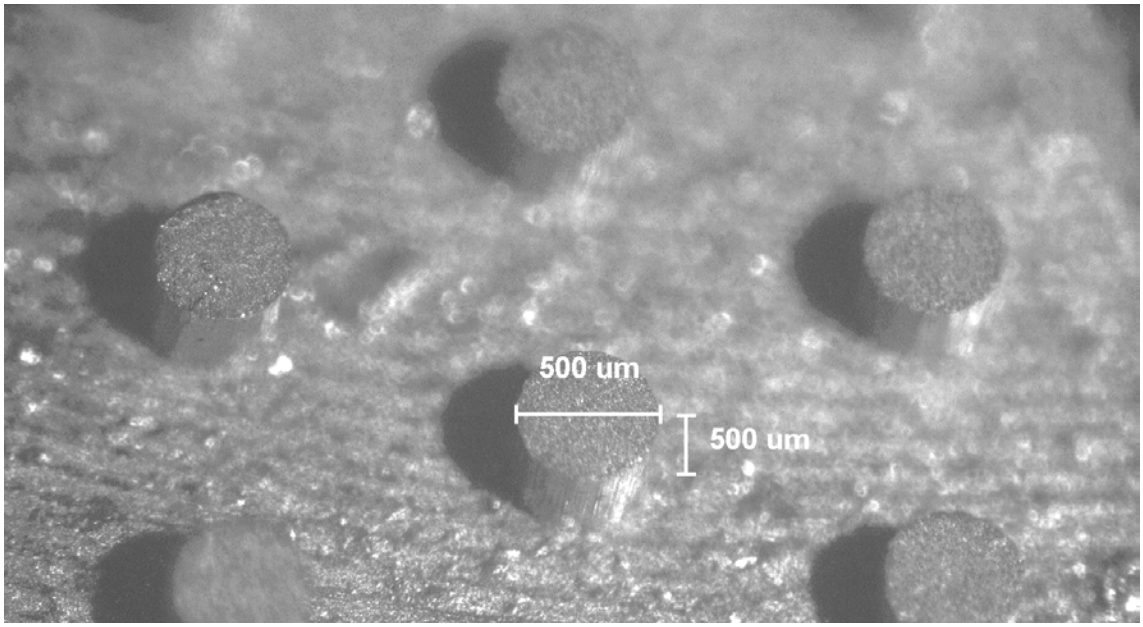

Figure 2-8: 3-D tilted view of the Nickel microstructures

CHAPTER 3 : EXPERIMENTAL STUDY OF THE FLAT METAL MICRO HEAT EXCHANGER

The manufactured heat exchanger described in Chapter 2 and a similar heat exchanger without the micro posts (or smooth channel) were used in a test procedure. The experimental results from the smooth channel configuration allowed validating the reliability of the testing apparatus and were used to estimate the enhancement due to the presence of the posts. Experiments at Reynolds numbers from 4,000 to 20,000 were conducted with air as a coolant.

3.1 Experimental Apparatus Design

The desired heat exchanger configuration depicted in Figure 2-1, lead to the design and construction of an experimental apparatus.

3.1.1 Important Design Aspects

The experimental apparatus has to deliver a coolant flow to the 500 μm tall heat exchanger and a given heat flux to the top surface. A modular jig permitting swapping the different heat exchangers to be tested was conceived. The lower half of the jig guides the coolant flow into channel of different heights and includes a recess housing the lower plate composing the heat exchanger. The upper half of the jig is a cover plate that includes the heating block and a recess allowing accurate positioning of the heat exchanger in the right location.

The important parameters of the design, shown in the AutoCAD drawings provided in Appendix C, are listed as follows:

- The velocity profile of the coolant entering the heat exchanger has to be fully developed. A 500 μm channel with enough hydrodynamic development length (30 times the hydraulic diameter [28]) is included upstream from the heat exchanger section. A 500 μm channel with enough length (18 times the hydraulic diameter [7]) was also added downstream from the heat exchanger to minimize exit effects.
- Heat leakage from the heating block into the upper half of the apparatus, other than the upper plate of the heat exchanger, and the ambient air have to be minimal and quantified. This aspect was solved by optimizing the material selection of the two solids, minimizing their contact surface area, and by using a layer of insulator around the heating block. Using a finite element model allowed estimating the rate of heat leakage.
- The pressurized coolant should not leak through either the contact area between the heating block and the upper half of the apparatus, or through the contact area between the upper and lower half of the apparatus. An O-ring was used to seal the upper and lower half together. A special gasket described in the next section was used around the heating block.

The material selection described in the next section was primordial to optimizing the design of the testing apparatus.

3.1.2 Material Selection

The apparatus is comprised of the following materials:

3.1.2.1 Aluminum 6061-T6

This metal was used to manufacture the heating block. The thermal conductivity is 165 W/mK [47], [22] and varies within ±10% as a function of temperature during the

subsequent experiments. The high thermal conductivity value of this material allows the temperature gradients within the heating block to be low. As a consequence, Aluminum is ideal to conduct heat to the heat exchanger while maintaining low temperatures in the heating block.

3.1.2.2 Virgin PEEK (PolyEtherEther-Ketone)

PEEK is a high performance engineering thermoplastic used a lot in medical and electronic industries. It was chosen to manufacture the upper and lower body parts of the apparatus. It has excellent mechanical properties and withstands up to 480°F (250°C) which is greater than the highest temperature within the heating block. The thermal conductivity is 0.25 W/mK, a relatively low value which makes this material a good insulator and minimizes the heat leakage rate.

3.1.2.3 Superflex^{TM} Clear RTV Silicone Adhesive sealant

This silicone, purchased from Loctite Corp., was used as a sealant between the heating block and the upper part of the apparatus. Its low viscosity allows accurate positioning and a thin coating thickness while and its high heat capability allows withstanding the temperature of the heater block.

3.1.2.4 Stainless Steel 316

This metal was used to manufacture the lower plate used for both micro pin fin and parallel plate heat exchangers as well as the upper plate and shims used to create the parallel plate heat exchanger. The temperature dependant thermal conductivity is around 13.5 W/mK and remains within ± 10 % [45] in the range of use.

3.1.2.5 Calsil (Calcium Silicate)

This material was used to insulate the aluminum block from the ambient air. The thermal conductivity is as low 0.047 W/mK.

3.1.3 Finite Element Analysis

In order to predict the heat leakage rate from the heating block into the surrounding PEEK and Calsil materials, a finite element model solving the three dimensional steady state heat equation was performed on ANSYS 5.7. The maximal heat losses occur when the parallel plate heat exchanger without posts is tested at the lowest flow rate (Re=4000) because the thermal resistance between the aluminum block and the coolant reaches its highest value. As shown in the detailed analysis presented in Appendix D, for the range of Reynolds number tested ($4000 \leq Re \leq 20000$) the parallel plate heat exchanger experiments undergo heat losses from 5.5 to 10.5 %.

Subsequently in this chapter, it will be seen that experimental results associated with the micro pin fin heat exchanger yield heating block temperatures equal to or lower than the lowest temperatures associated with the parallel plate heat exchanger. Consequently, for the pin fin heat exchanger, the thermal resistance to the coolant is lower meaning that the heat losses must be always lower than 5.5 %.

3.1.4 Description of the Experimental Apparatus

The heat exchanger is sandwiched between the lower and upper halves of the experimental apparatus, which are screwed together as depicted in Figure 3-1. After flowing through a pressure regulator and a filter, the coolant enters a 5 cm diameter and 2 cm deep reservoir machined into one end of the lower half of the PEEK apparatus (Figure 3-2) and flows through a channel with rectangular cross section (5.0 cm wide and 3.2 mm

high). The volumetric flow rate of the coolant is measured with a 2-25 SCFM (standard cubic foot per minute) range direct-reading spring-loaded flow meter.

The channel height decreases to 500 μm (equal to the gap between the plates of the micro heat exchanger) a distance of 3.1 cm upstream of the entrance to the micro heat exchanger (Figure 3-2). Recesses in both the upper and lower halves of the experimental apparatus are machined to accommodate the thickness of both the upper and lower plates of the heat exchanger (Figure 3-2). These recesses allow the inner surfaces of the top and bottom plates of the heat exchanger to be flush with the upper and lower surfaces of the channel.

Energy is transferred to the coolant through the upper surface of the heat exchanger which is tightly clamped to the bottom surface of the heating block. A 100 μm thick layer of thermally conductive silicone paste (OMEGATHERM® 201 with thermal conductivity of 2.3 W/mK, from Omega Engineering Inc.) is used as a thermal joint at that interface in order to minimize the contact resistance. The energy is supplied by four 120V-250W electric resistance cartridge heaters inserted into the aluminum block located directly above the heat exchanger (Figure 3-1). The total electrical power can be varied using a potentiometer and monitored using a digital wattmeter/multimeter (Model 380660 from Extech Instruments). The cross section of the heating block increases from 4.83 cm by 4.83 cm in the upper side to 5 cm by 5 cm in the lower side to match the top surface of the heat exchanger. The heaters are located within the block a sufficient distance from the heat exchangers to insure one dimensional conduction heat transfer within the block. In addition, the aluminum block is insulated to ensure that a very large percentage of the electrical energy is transferred to the coolant.

The 500 μm height of the channel remains constant through the longitudinal span of micro heat exchanger until 3.8 mm downstream of the heat exchanger (Figure 3-2). At this point the height of the flow channel increases again to 3.2 mm before emptying into a downstream reservoir with same dimensions as the upstream reservoir.

The inlet and exit temperatures of the coolant can be measured by thermocouples located, respectively, in the upstream and downstream reservoir. Thermocouple measurements can also be taken at two elevations within the aluminum block that houses the heaters as shown in Figure 3-1. All the thermocouples are connected to a handheld digital thermometer via a multi-point switchbox, which allows 6 inputs at the same time. Pressure taps located 1.3 cm upstream and downstream of the heat exchanger provide the static pressure drop. The pressure difference between the taps is quantified using a differential pressure transducer coupled to a strain gage meter. The upstream and downstream reservoir gage pressures as well as the upstream tap gage pressure are measured using spring loaded pressure gages.

3.2 Experimental Procedure

A series of experiments were conducted with both the pin fin heat exchanger and the parallel plate heat exchanger with compressed air used as a coolant. Results were obtained as a function of volumetric flow rate corresponding to a range of Reynolds numbers from 4,000 to 20,000. Each flow rate was set and maintained to the desired value using the pressure regulator.

As for the heat transfer experiments, at each flow rate, the output power from the four resistance heaters was set to approximately 100 Watts by adjusting power with the potentiometer connected to the wattmeter.

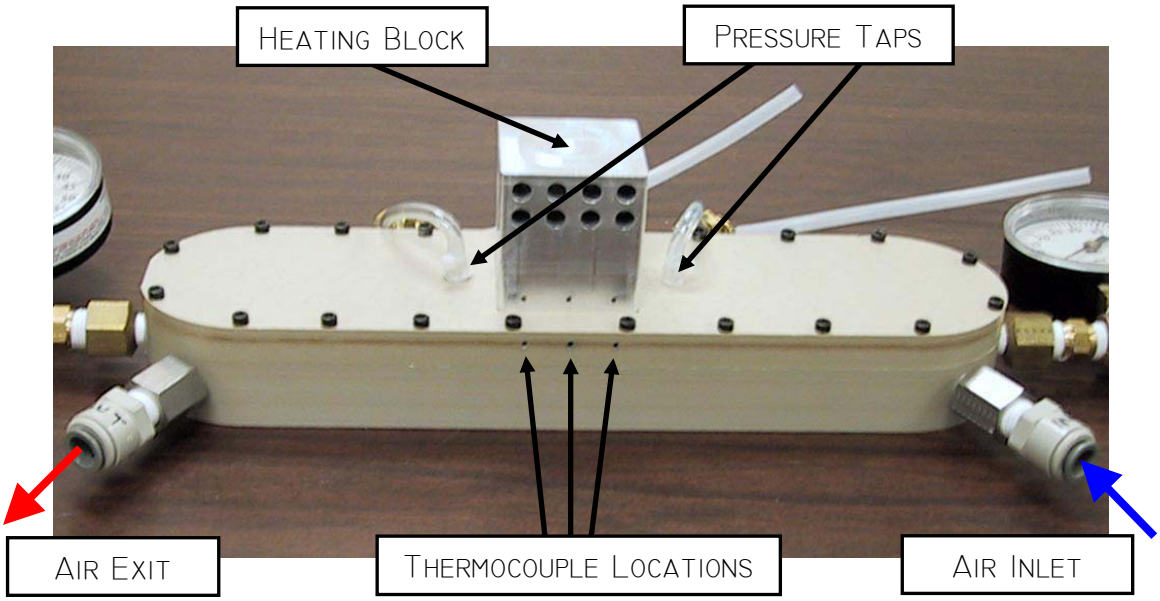

Figure 3-1: Assembled Apparatus

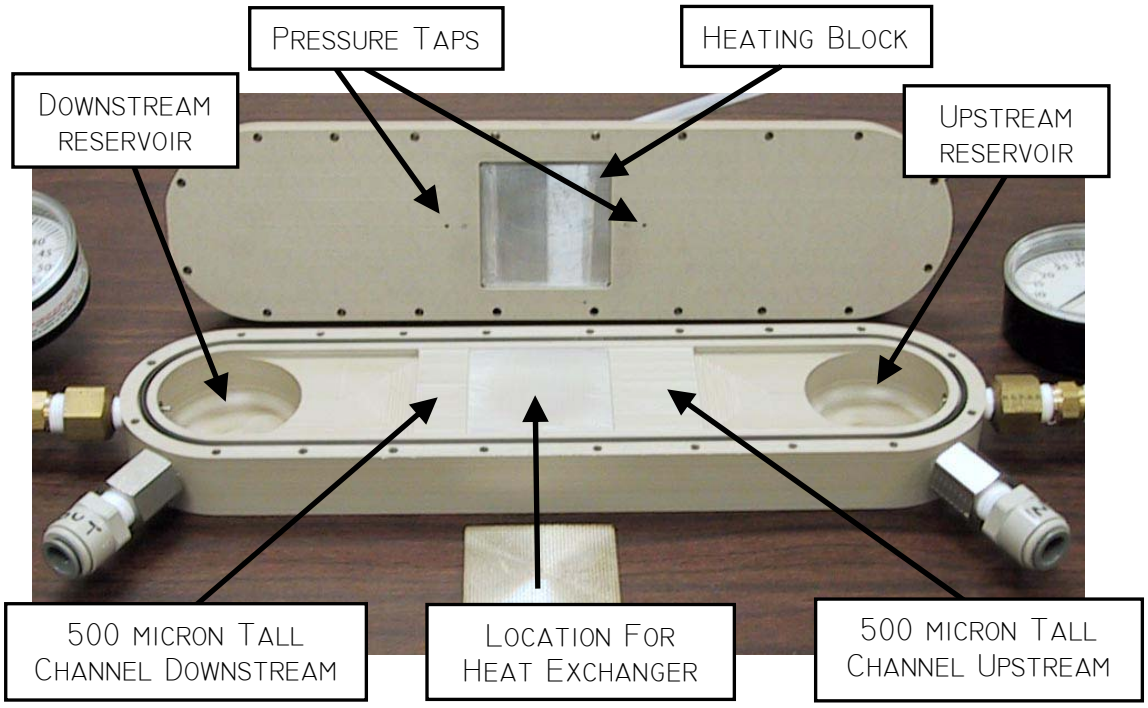

Figure 3-2: Open view of apparatus

Therefore, a constant flux boundary condition was produced through the top surface of the heat exchangers.

For a given heat exchanger configuration, flow rate, pressure and temperature data acquisition was executed after steady state conditions were attained (at steady state, the monitored temperature at center of the heating block becomes constant). The pressures and temperatures of the coolant were recorded in all instrumented locations mentioned in the previous section.

Thermocouple measurements were taken at two elevations within the aluminum block. These measurements are used to quantify the flux through the top plate. It is noted that only the temperatures at the center of the heating block were recorded for the reasons that follow. The two extreme temperature distributions within the heater correspond to the case where the flow rate is highest with the micro pin fin heat exchanger (case 1) and the case where the flow rate is lowest with parallel plates (case 2). In both cases the temperatures in the block at the highest elevation (elevation 2) were constant within ±0.2ºC (±0.5%). At the lowest elevation (elevation 1), they increase linearly by a rate of 0.3ºC/cm but the center value represents the arithmetic average temperature. At elevation 1 the temperature varies in the spanwise direction from the center of the block outward by 0.3ºC/cm for case 1 and 0.2ºC/cm for case 2. Therefore using the center temperature value at elevation 1 approximates the average temperature by ±0.5ºC (±1.0%). As a conclusion, when using the center block temperatures, the approximation leads to a systematic error lower than 1.0% for both elevations and allows reducing the experimenting time by a factor of 9.

When it comes to pressure loss experiments, the data acquisition procedure is

similar to above, except that all temperatures and pressures of the coolant were recorded adiabatically (without any heat flux). For that reason, the temperatures within the heating block were not recorded.

3.3 Data Reduction

Positions where pressure and temperature are measured in the upstream and downstream reservoir are respectively labeled locations (1) and (4). The pressure taps situated 1.3 cm upstream and downstream from the heat exchanger are respectively labeled locations (2) and (3).

In the heat exchanger, the properties of the coolant such as specific heat C_p, density ρ, thermal conductivity k and dynamic viscosity μ are evaluated at the film temperature T_f defined as:

$$T_f = \frac{T_w + T_b}{2}$$

Equation 3-1

T_w is the temperature of the top plate at the coolant-plate interface. This value is determined indirectly with the method explained further in Section 3.3.2.2.

T_b, the bulk temperature of the coolant, is approximated as shown in Equation 3-2 by the arithmetic average of T_2 and $T_{3\text{-}tot}$, which are respectively the coolant static temperature at the inlet and the coolant total temperature at the exit of the heat exchanger. $T_{3\text{-}tot}$ is defined as the sum of the static temperature T_3 at the outlet of the heat exchanger and the dynamic temperature change through the heat exchanger as written in Equation 3-3. V and C_p are respectively the velocity and the specific heat at constant pressure of the coolant.

$$T_b = \frac{T_2 + T_{3-tot}}{2}$$

Equation 3-2

$$T_{3-tot} = T_3 + \frac{1}{2 \cdot Cp}\left(V_3^2 - V_2^2\right)$$

Equation 3-3

The choice of $T_{3\text{-}tot}$ versus T_3 for the calculation of T_b can be justified two different ways:

- The first way is modeled in Appendix E with the case of highest coolant flow rate in the case of the pin fin heat exchanger where kinetic energy effects are greatest (since the velocity change through the heat exchanger is the greatest). It can be qualitatively seen that the actual changes of bulk temperature can be better approximated by the changes in total temperature than by a linear variation from T_2 to T_3.
- The second way to explain the use of $T_{3\text{-}tot}$ versus T_3 is related to the fact that the heat exchangers transfer energy into the coolant not only in the form of internal energy but also in the form of kinetic energy. In the subsequent calculations of the convective heat transfer coefficient, the only way to account for the increase in kinetic energy is to use total temperatures instead of static temperatures.

Note can be made that Chyu's studies, which involve the naphthalene sublimation technique and the heat/mass transfer analogy, do not face effects analogue to the kinetic energy effects of the present study because naphthalene bulk densities do not vary much.

The values of T_2 and T_3 are determined indirectly as shown in the following paragraph.

T_2 the inlet temperature of the coolant differs from T_1, due to kinetic energy effects. Equation 3-4 is found by applying the first law of thermodynamics at steady state conditions between locations (1) and (2) in the absence of dissipative effects. h and $\dot{m}$ are respectively the specific enthalpy and the mass flow rate of the coolant.

$$\dot{m}\left((h_2 - h_1) + \frac{1}{2}\left(V_2^2 - V_1^2\right)\right) = 0$$

Equation 3-4

Equation 3-5 and Equation 3-6 are derived by using the assumptions that air is an ideal gas characterized by the constant R and the fact that C_p is unvarying.

$$h_2 - h_1 = Cp(T_2 - T_1)$$

Equation 3-5

$$V_2 = \frac{\dot{m}RT_2}{A_2P_2}$$

Equation 3-6

Admitting that V_2 is much larger than V_1, since the cross sectional area of the flow at location A_1 is a relatively large compared to location A_2, combining Equation 3-4 through Equation 3-6 and solving for T_2 yield Equation 3-7:

$$T_2 = \frac{-2 \cdot C_P + \sqrt{(2 \cdot C_P)^2 - 4 \cdot \left(\frac{\dot{m}R}{A_2P_2}\right)^2 \cdot (-2 \cdot C_P T_1)}}{2 \cdot \left(\frac{\dot{m}R}{A_2P_2}\right)^2}$$

Equation 3-7

Using the same steps as above between locations (3) and (4) yields Equation 3-8.

$$T_3 = \frac{-2 \cdot C_P + \sqrt{(2 \cdot C_P)^2 - 4 \cdot \left(\frac{\dot{m}R}{A_3 P_3}\right)^2 \cdot (-2 \cdot C_P T_4)}}{2 \cdot \left(\frac{\dot{m}R}{A_3 P_3}\right)^2}$$

Equation 3-8

Note is made that P_3 is equal to P_2-ΔP_{23}, ΔP_{23} being the pressure drop measured between locations (2) and (3). In addition, the mass flow rate $\dot{m}$ is the product of volumetric flow rate $\dot{V}$ in SCFM read directly on the flowmeter and the density of air ρ_o at standard conditions (pressure of 1 atmosphere and temperature of 70ºF).

3.3.1 Reynolds Number

The Reynolds number *Re* used herein and defined in Equation 3-9 is based on the average velocity V in the channel and the hydraulic diameter of the micro channel D_h, which is twice the height H of the gap.

$$\mathrm{Re} = \frac{\rho \cdot V \cdot D_h}{\mu} \qquad \text{with} \qquad D_h = 2 \cdot H$$

Equation 3-9

Care must be taken when comparing results to studies from other authors. The hydraulic diameter is sometimes based on the pin diameter and the maximum velocity V_{max} which takes place where the cross sectional area is minimal (between columns of posts). Using the mass flow rate of coolant $\dot{m}$ and the maximal cross sectional area of the flow in the heat exchanger A, Equation 3-9 can be re-arranged as:

$$\mathrm{Re} = \frac{\dot{m} \cdot D_h}{A \cdot \mu}$$

Equation 3-10

3.3.2 Convective Heat Transfer Coefficient and Nusselt Number

The average convective heat transfer coefficient h is defined in this study as:

$$h = \frac{Q}{A_{heat} \cdot (T_w - T_b)}$$

Equation 3-11

Q is the total amount of heat transferred to the coolant and A_{heat} the surface area of the upper side of the heat exchanger, not the total wetted surface area actually available for heat transfer. Therefore A_{heat} is the same for both tested heat exchangers.

The average Nusselt number defined below customarily presents the convective heat transfer coefficient in the dimensionless form:

$$Nu = \frac{h \cdot D_h}{k}$$

Equation 3-12

In order to determine the heat transfer coefficient the unknowns Q and T_w have to be determined for each coolant, flow rate and heat exchanger configuration.

3.3.2.1 Determination of *Q*

Q can be easily determined by three different ways. First, it can be given by the reading on the wattmeter $Q_{electric}$, which corresponds to the heat provided by the heaters.

Another way to determine Q is to use the temperatures measured above the heat exchanger at elevations (1) and (2), referred to as T_{bot} and T_{top} in Figure 3-3. These temperatures, coupled with the known thermal conductivity of the metal k_{Al}, cross section of the aluminum block A_{heat} and the distance between the two elevations $d_{top\text{-}bot}$, provide

the necessary inputs to Equation 3-13 to calculate the rate of heat transferred to the upper surface of the heat exchanger $Q_{conduction}$.

$$Q_{conduction} = \frac{A_{\text{heat}} \cdot k_{\text{Al}} \cdot \left(T_{top} - T_{bot}\right)}{d_{\text{top-bot}}}$$

Equation 3-13

A final, rough method to calculate the energy supplied to the coolant is Equation 3-14. However, at low Reynolds numbers of coolant, the volumetric flow rate is relatively small relative to the uncertainty of the measurement and this method becomes unreliable.

$$Q_{convection} = \dot{\text{m}} \cdot C_p \cdot \left(T_4 - T_1\right)$$

Equation 3-14

3.3.2.2 Determination of T_w

The last unknown, T_w, is found using the following method. A one-dimensional series of thermal resistances connect the horizontal plane with thermocouple holes at elevation (1) and the coolant. The validity of the one-dimensional heat transfer model is verified in the finite element study presented in Appendix E. As depicted in Figure 3-3, this series consists of:

- a conduction resistance through the aluminum R_{Al}
- a contact resistance at the heat exchanger/aluminum interface $R_{contact}$ through the thin layer of thermally conductive silicone paste
- a conductive resistance through the Nickel (or Stainless steel) upper plate of the heat exchanger R_{Ni} (or R_{SS})
- an effective convective resistance at the heat exchanger-coolant interface $R_{convection}$.

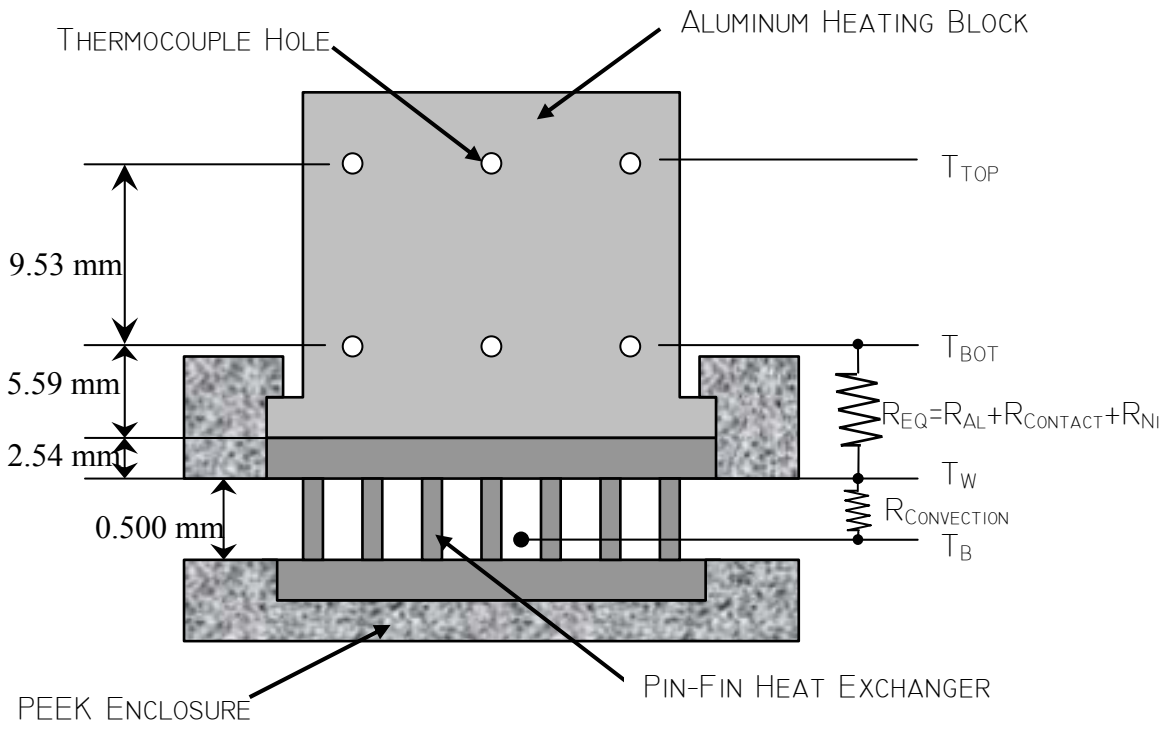

Figure 3-3: Schematic of thermal resistances within the heat exchanger

The first three of these resistances do not vary with flow rate and are summed in Equation 3-15 into a single equivalent resistance R_{eq}.

$$R_{eq} = \frac{l_{Al}}{k_{Al}} + \frac{l_{silicone}}{k_{silicone}} + \frac{l_{Ni}}{k_{Ni}} \qquad (\text{or } R_{eq} = \frac{l_{Al}}{k_{Al}} + \frac{l_{silicone}}{k_{silicone}} + \frac{l_{SS}}{k_{SS}})$$

Equation 3-15

R_{Al} , $R_{contact}$, R_{Ni} and R_{SS} can be explicitly calculated from the conduction characteristic length l and the thermal conductivities k. Their values are respectively 3.4, 4.3, 2.8 and 18.8 $m^2K/W*10^{-5}$.

Since the value of R_{eq} is independent of flow rate, Equation 3-16 can be used to solve for T_w at any flow rate:

$$T_w = T_{bot} - \frac{Q}{A_{heat}} \cdot R_{eq}$$

Equation 3-16

3.3.3 Pressure Loss and Friction Factor

The friction factor in the heat exchanger is a non-dimensional definition of the pressure drop ΔP_{HE} in the heat exchanger as given in Equation 3-17 [27]:

$$f = \frac{\Delta P_{HE}}{\left(\frac{\rho \cdot V^2}{2}\right)} \cdot \frac{D_h}{L}$$

Equation 3-17

In the equation above, L represents the dimension of the channel in the streamwise direction. Some authors [34], [39], [40] also define the friction factor normalized by the number of rows of pins N using the maximum velocity in the channel V_{max} as shown in Equation 3-18.

$$f = \frac{\Delta P_{HE}}{\left(\frac{\rho \cdot V_{\max}^2}{2}\right)} \cdot \frac{1}{N}$$

Equation 3-18

To calculate the value of ΔP_{HE}, one must realize that the differential pressure ΔP_{23} between the two pressure tap locations measured by the pressure transducer has three main components:

1. ΔP_{inlet}: the inlet pressure drop associated with the frictional losses in the 1.3 cm long and 500 μm tall channel upstream from the heat exchanger.
2. ΔP_{HE}: the pressure drop corresponding to the frictional losses within the heat exchanger only.
3. ΔP_{exit}: the exit pressure drop associated with the frictional losses in the 1.3 cm long and 500 μm tall channel downstream from the heat exchanger.

The terms ΔP_{inlet} and ΔP_{exit} are identical in both heat exchanger configurations and have the same friction factor as in the smooth channel (parallel plate heat exchanger) configuration. The corresponding values are found by geometrical considerations and given in Equation 3-19.

$$\Delta P_{inlet} = \Delta P_{exit} = \frac{1.3 \cdot cm}{(1.3 + 5.0 + 1.3) \cdot cm} \cdot \Delta P_{HE} \text{ (parallel plate heat exchanger)}$$

Equation 3-19

Finally ΔP_{HE} can be calculated using Equation 3-20:

$$\Delta P_{HE} = \Delta P_{23} - \Delta P_{inlet} - \Delta P_{exit}$$

Equation 3-20

3.4 Experimental Results and Uncertainty Analysis

3.4.1 Experimental Results

Raw data collected during the experiments is organized and provided in Table 3-1 and Table 3-2 for the parallel plate heat exchanger. The data presented in Table 3-3 and Table 3-4 correspond to the micro pin fin heat exchanger. Repeatability for all the test runs is within 5%.

Table 3-1: Heat transfer experimental data for the parallel plate heat exchanger

$\dot{V}$ (SCFM)	P_1 (psig)	P_2 (psig)	ΔP_{23} (psid)	P_4 (psig)	T_1 (ºC)	T_4 (ºC)	T_{bot} (ºC)	T_{top} (ºC)	$Q_{electric}$ (W)
4.0	4.0	3.0	1.5	0	20.1	55.5	145.1	147.5	99
8.0	12	10	4.7	4	18	37.9	86.7	89.1	102
12.0	21	18	7.4	10	18	31.8	70.1	72.4	103
16.0	33	30	9.7	19	18.2	28.7	61.2	63.5	103

Table 3-2: Pressure loss experimental data for the parallel plate heat exchanger

$\dot{V}$ (SCFM)	P_1 (psig)	P_2 (psig)	ΔP_{23} (psid)	P_4 (psig)	T_1 (ºC)	T_4 (ºC)
3	2.5	1	0.5	0	20.6	20.8
5	5	3	1.5	0	20.6	20.8
7	8	6	2.6	3	20.6	20.7
9	12.5	10	3.8	5	20.5	20.6
11	16	13	4.6	7.5	20.4	20.7
13	21	17	5.6	11	20.5	20.7
15	28	24	6.6	16.5	20.3	20.6
17	34.5	30	7.5	22	20.5	21.0

Table 3-3: Heat transfer experimental data for the micro pin fin heat exchanger

$\dot{V}$ (SCFM)	P_1 (psig)	P_2 (psig)	ΔP_{23} (psid)	P_4 (psig)	T_1 (ºC)	T_4 (ºC)	T_{bot} (ºC)	T_{top} (ºC)	$Q_{electric}$ (W)
4	11	10	9.2	0	20.5	58.7	73.0	75.5	99
8	31.5	30	25.6	4	20.3	40.4	46.6	49.0	98
12	51	49	39	10	20.4	34.1	39.5	41.7	100
16	67	65	46.3	19	20.6	31.5	36.9	39.2	100

Table 3-4: Pressure loss experimental data for the micro pin fin heat exchanger

$\dot{V}$ (SCFM)	P_1 (psig)	P_2 (psig)	ΔP_{23} (psid)	P_4 (psig)	T_1 (ºC)	T_4 (ºC)
3	8.5	7.5	7.0	0	20.3	20.5
5	15	14	12.5	0	20.0	21.1
7	24	23	20.1	2	19.9	20.5
9	34.5	33	27.9	4	19.9	20.4
11	43	41	33.6	8	20.1	20.0
13.5	59	56	43.2	12	20.1	19.7
15.5	66	64	47.5	16.5	20.1	19.7

Table 3-5: Heat transfer results for the parallel plate heat exchanger

$\dot{m}$ (kg/s)	Re	*error Re* (%)	T_2 (ºC)	$T_{3\text{-}tot}$ (ºC)	T_w (ºC)	$Q_{conduction}$ (W) (%$Q_{electric}$)	$Q_{convection}$ (W) (%$Q_{electric}$)	h (W/m^{2}K)	Nu	*error Nu (%)*
0.0023	4206	12.5	18.2	53.6	134.	107 (108)	80 (81)	388	12.6	3.8
0.0045	9114	6.2	14.3	34.2	76.2	107 (105)	90 (88)	760	27.1	4.2
0.0068	14023	4.2	13.2	27	59.5	103 (100)	94 (91)	1014	37.2	4.2
0.0091	18934	3.1	13.7	24.2	50.6	103 (100)	95 (92)	1259	46.8	4.7

Table 3-6: Pressure loss results for the parallel plate heat exchanger

$\dot{m}$ (kg/s)	*Re*	*error Re* (%)	T_2 (ºC)	T_3 (ºC)	ΔP_{HE} (psid)	*f*	*error f* (%)
0.0017	3693	16.7	19.3	19.4	0.3	0.026	39.6
0.0028	6184	10	17.7	17.3	1	0.031	22.6
0.004	8694	7.1	16.5	15.3	1.7	0.031	17.1
0.0051	11209	5.6	15.7	14	2.5	0.032	14.3
0.0062	13741	4.5	14.8	12.7	3.1	0.029	12.8
0.0074	16260	3.8	14.5	12	3.7	0.029	11.8
0.0085	18729	3.3	14.9	12.9	4.4	0.032	11.2
0.0096	21195	2.9	15.3	13.6	5	0.032	10.8

Table 3-7: Heat transfer results for the micro pin fin heat exchanger

$\dot{m}$ (kg/s)	*Re*	*error Re* (%)	T_2 (ºC)	$T_{3\text{-}tot}$ (ºC)	T_w (ºC)	$Q_{conduction}$ (W) (%$Q_{electric}$)	$Q_{convection}$ (W) (%$Q_{electric}$)	*h* (W/m^{2}K)	*Nu*	*error Nu (%)*
0.0023	4518	12.5	19.5	57.7	69	112 (113)	87 (87)	1265	44.7	4.2
0.0045	9440	6.2	19.1	39.2	42.6	107 (109)	91 (93)	2830	104.9	5.5
0.0068	14347	4.2	19.1	32.8	35.4	98 (98)	93 (93)	4094	154	6.8
0.0091	19227	3.1	19.1	30	32.8	103 (103)	99 (99)	4702	177.8	7.4

Table 3-8: Pressure loss results for the micro pin fin heat exchanger

$\dot{m}$ (kg/s)	*Re*	*error Re* (%)	T_2 (ºC)	T_3 (ºC)	ΔP_{HE} (psid)	*f*	*error f* (%)
0.0017	3693	16.7	19.6	19.1	6.8	0.637	36.8
0.0028	6172	10	18.9	17.6	12	0.485	23.1
0.004	8675	7.1	18.6	14.9	19.2	0.491	17.5
0.0051	11180	5.6	18.6	13.1	26.6	0.504	14.7
0.0062	13695	4.5	18.7	11.4	32.1	0.47	13.1
0.0076	16806	3.8	18.8	11.3	41.3	0.506	11.8
0.0088	19303	3.3	18.7	11.1	45.2	0.471	11.2

3.4.2 Uncertainty Analysis

In order to determine the accuracy (or uncertainty) of the final experimental results, an error analysis is performed.

First, this error analysis requires knowledge of the fact that all primary experimental measurements are characterized by uncertainties related to the metering equipment. These uncertainties are usually provided by the manufacturer. The absolute uncertainties on the measured pressures, temperatures, volumetric flow rates and electrical wattage are summarized in Table 3-9.

Table 3-9: Absolute uncertainties on the measured quantities

Measurement	$\dot{V}$ (SCFM)	T_1, T_4, T_{bot} (°C)	P_2 (psig)	ΔP_{23} (psid)	$Q_{electric}$ (W)
Absolute (±)	0.5	0.1	1.0	0.1 or 1.0	2.0

In addition, the following quantities have been accounted for in the uncertainty calculation because of the reasons mentioned:

- The thermal conductivities of the metals (their values were assumed constant even though they vary with temperature)
- The height of the micro posts (the heights are almost identical)
- The locations at which T_{bot} and T_{top} are calculated (these locations are 1/16 inch diameter holes and not points)
- The thickness of thermally conductive paste applied (this value is not known exactly)

Based on the experimenter's testing experience and literature survey data, intervals of confidence were specified for the quantities listed above as summarized in Table 3-10.

Table 3-10: Interval of confidence for other quantities

Quantity	k_{SS} (W/mK)	k_{Ni} (W/mK)	k_{Al} (W/mK)	H (μm)	$l_{silicone}$ (μm)	l_{Al} (μm)
Absolute (±)	1.0	9.0	10.0	15	25	794

Furthermore, it is assumed that fixed errors are negligible and that there are no other sources of errors.

According to the Kline and McClintock method [18], when an experimental results R is a function of independent variables $x_1, x_2,\ldots, x_n$, i.e. $R=R(x_1, x_2, \ldots, x_n)$, the uncertainty in the result w_R is given as shown in Equation 3-21. The quantities $w_1, w_2,\ldots, w_n$ are the uncertainties in the independent variables.

$$w_R = \left[\left(\frac{\partial R}{\partial x_1} w_1 \right)^2 + \left(\frac{\partial R}{\partial x_2} w_2 \right)^2 + \ldots + \left(\frac{\partial R}{\partial x_n} w_n \right)^2 \right]^{1/2}$$

Equation 3-21

The Kline and McClintock method was used to determine the uncertainty in the determination of *Re*, *Nu* and *f* in each heat exchanger configuration and coolant flow rate setting. The results are indicated in Table 3-5 through Table 3-8 under the columns *error Re*, *error Nu* and *error f*.

3.5 Results and Discussion

Nusselt number and friction factor experimental results as a function of Reynolds number are plotted respectively in Figure 3-4 and Figure 3-5. As expected, the presence of the pin fins has a dramatic effect in both experiments.

3.5.1 Heat Transfer Results

From Table 3-5 and Table 3-7, it appears that the heat rate transferred to the coolant by convection $Q_{convection}$ increases with Reynolds number and is always greater for the micro pin fin heat exchanger than the parallel plate heat exchanger at any given Reynolds number. The reason is the heat transfer resistance to the coolant decreases as the convective heat transfer coefficient increases and this effect is accompanied by a decrease in heat losses to the surroundings. For all experimental runs, more than 90% of the heat is transferred to the coolant by convection for both heat exchangers configurations except at the lowest flow rate in the case of the parallel plate heat exchanger, where only 81 % of the heat is transferred. However, at the lowest volumetric flow rate, the uncertainty of the measurement is relatively high (±12.5%).

Additionally, for all the experimental runs the heat transferred by conduction to the top plate of the heat exchanger is very close to or greater than 100%. The explanation for values greater then 100% originates from two reasons:

- the fact that the thermal conductivity of Aluminum was chosen constant, although it increases with temperature (the calculated value of $Q_{conduction}$ increases when the heating block temperature increases which occurs as the volumetric flow rate of coolant decreases).

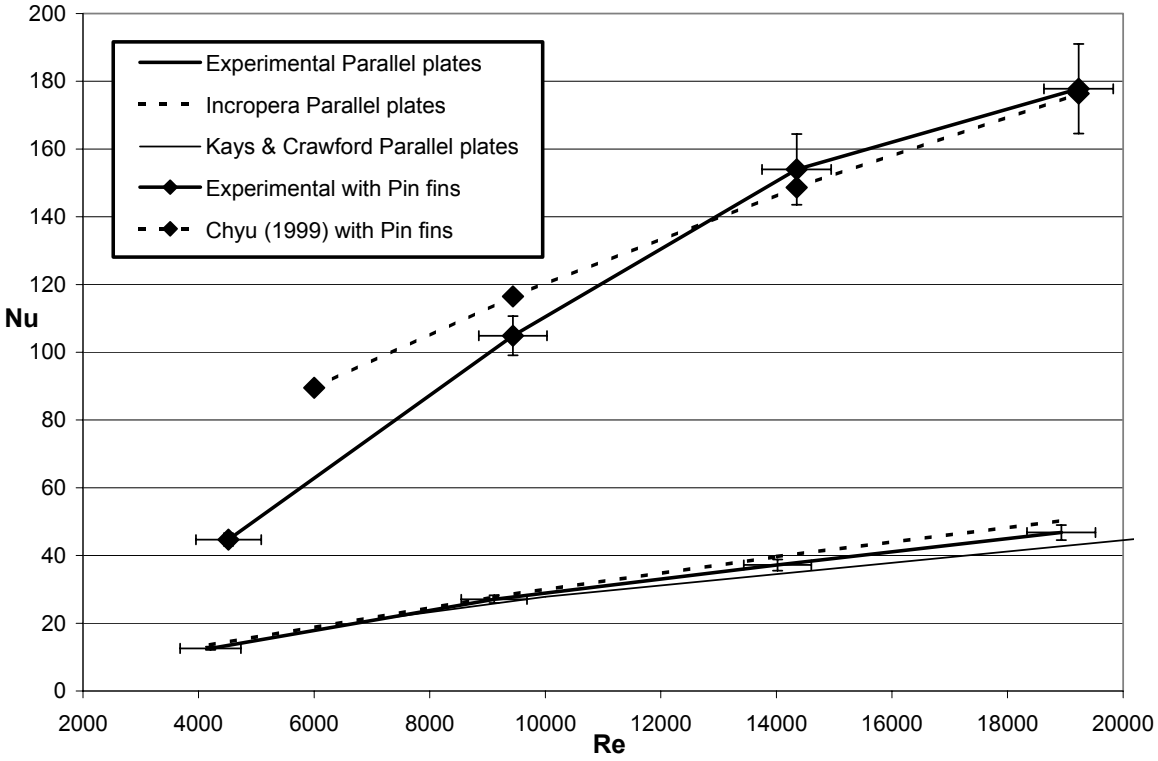

Figure 3-4: Nusselt number as a function of Reynolds number

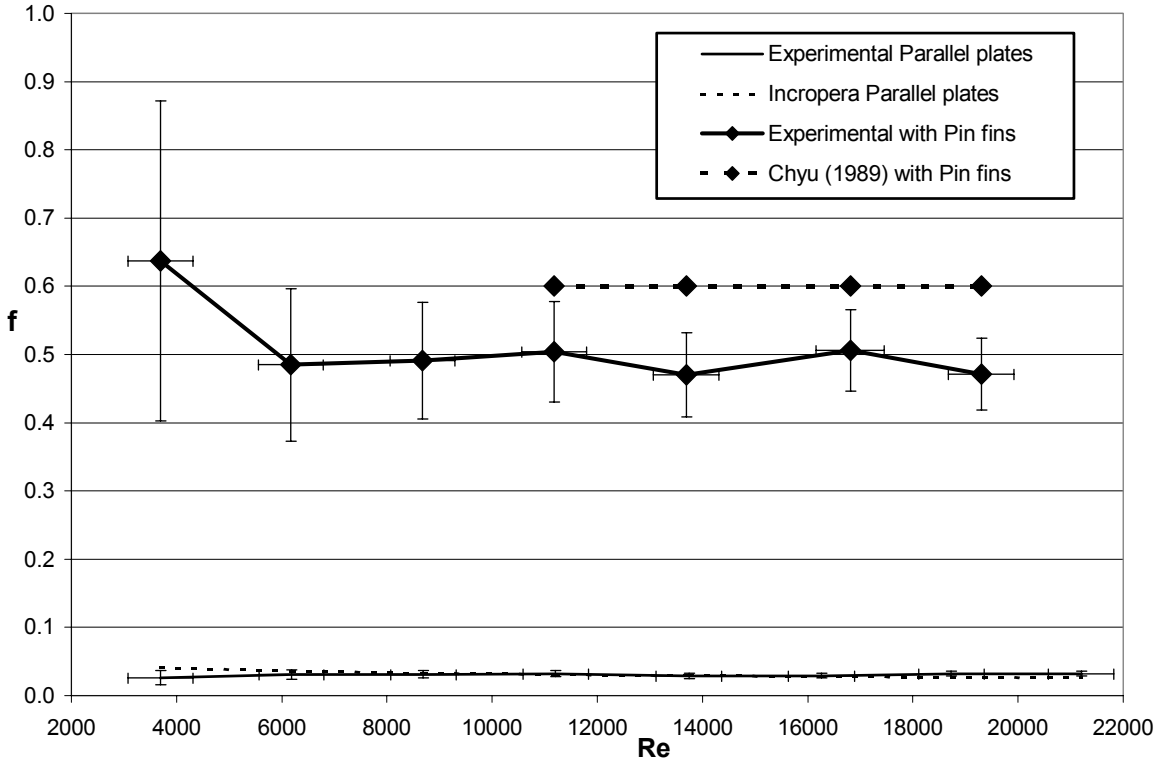

Figure 3-5: Friction factor as a function of Reynolds number

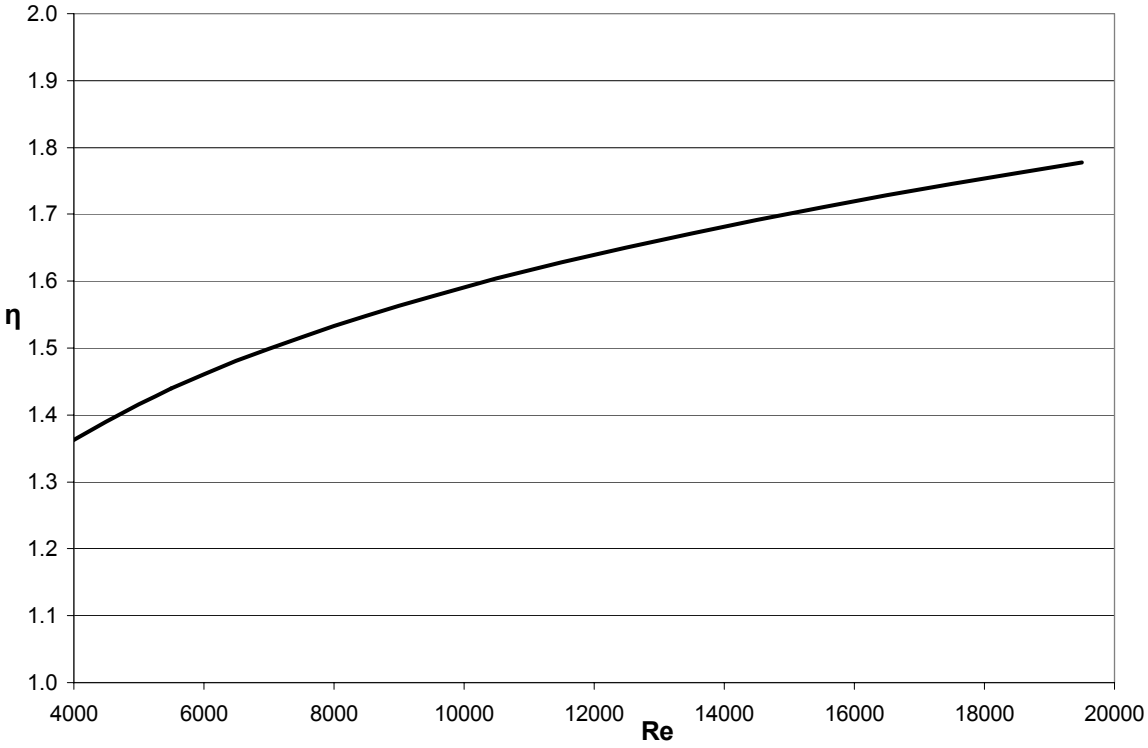

Figure 3-6: Overall thermal performance parameter as a function of Reynolds number

- the fact that the thermocouples measure the temperatures T_{top} and T_{bot} anywhere inside the 1/16 inch diameter holes located at elevation 1 and elevation 2. This creates uncertainties up to 17% in the distance between the two elevations which propagates into the calculation of $Q_{conduction}$.

In summary, especially for the pin fin micro heat exchanger but also for the parallel plate heat exchanger at higher flow rates, $Q_{electric} = Q_{conduction} = Q_{convection}$. This conclusion validates the temperature measurements in both the aluminum heating block and the air coolant stream. Also, it validates the assumption that the average heat flux over the entire heating block is well represented by the measured heat flux at the center of the heating block.

The Nusselt numbers plotted in Figure 3-4 are shown with error bars. According to the graph, the presence of the micro pin fins enhances the heat transfer by a factor of 3.3 to 4 over the range of Reynolds number studied 4,000 to 20,000. Surface roughness effects have not been included in the analysis since the relative surface roughness is negligible. Figure 3-4 also displays experimental results from Kays & Crawford [31] for fully developed turbulent flow between parallel plates, constant heat rate and one side heated while the other is insulated as well as a correlation from Incropera & DeWitt [28] valid for turbulent fully developed flow in circular tubes (Equation 3-22).

$$Nu = \frac{(f/8)\cdot(\mathrm{Re}-1000)\cdot \mathrm{Pr}}{1+12.7\cdot(f/8)^{1/2}\cdot(\mathrm{Pr}^{2/3}-1)} \qquad \begin{aligned} f &= 0.316\cdot \mathrm{Re}^{1/4} \\ 0.5 &< \mathrm{Pr} < 2000 \\ 3{,}000 &\le \mathrm{Re} \le 5\cdot 10^{6} \end{aligned}$$

Equation 3-22

It appears that the experimental results for parallel plates are in very good agreement with the correlations from Incropera & DeWitt (3% to 8%) and the data from

Kays & Crawford (1% to 4%). This very good match corroborates the reliability of the experimental apparatus and the validity of the all heat transfer experimental data. Note is made that for turbulent flows, the convective heat transfer coefficient is the same whether one side of the heat exchanger is heated or both because the thermal boundary layer profile is similar.

Furthermore, pin fin heat exchanger results are compared to Chyu's correlation [8] which corresponds to a heat transfer system in which the wetted surface is entirely isothermal and comprised of seven rows of posts with same array configuration as in the present study. The correlation shown in Equation 3-23 was adapted to the characteristic lengths used throughout this research.

$$Nu = 0.645 \cdot \mathrm{Re}^{0.583} \cdot \mathrm{Pr}^{0.4} \qquad 6{,}000 \le \mathrm{Re} \le 30{,}000$$

Equation 3-23

Within the range of Reynolds numbers common to the present study and Chyu's, Nusselt numbers are in good agreement, within 10%, for Reynolds numbers greater than 9,500. At a Reynolds number equal to 6,000, which is the lowest Reynolds number studied by Chyu, the difference in Nusselt numbers increases to 70%.

The Nu-Re power correlation suggested for micro pin fin heat exchanger is given in Equation 3-24:

$$Nu = 0.014 \cdot \mathrm{Re}^{0.977} \cdot \mathrm{Pr}^{0.4} \qquad 4{,}500 \le \mathrm{Re} \le 19{,}200$$

Equation 3-24

3.5.2 Pressure Loss Results

The experimental friction factors plotted in Figure 3-5 are shown with error bars. According to the graph, the presence of the micro pin fins increases the friction factor by

a factor of 20 to 15 over the range of Reynolds number studied.

The correlation from Incropera & DeWitt [28] valid for turbulent fully developed flow in circular tubes is shown in Equation 3-25 and plotted in Figure 3-5.

$$f = 0.316 \cdot \mathrm{Re}^{1/4} \qquad \mathrm{Re} \le 2 \cdot 10^4$$

Equation 3-25

It appears that the experimental results for parallel plates are within 15 % of agreement with the correlated data from Incropera & DeWitt for Reynolds numbers ranging from 6,200 to 19,000. Immediately outside of this range the discrepancies exceed 20 %. Again, the very good match within a large range of Reynolds numbers confirms the reliability of the experimental apparatus and the validity of the pressure loss experimental data.

In addition, pin fin heat exchanger results are compared to Chyu's friction factor [7] which is approximately 0.6 over the range of Reynolds numbers from 11,200 to 19,300 once the characteristic lengths defined in this study are applied. The micro pin fin heat exchanger results are estimated to be within 30% of Chyu's data.

As a conclusion about heat transfer and pressure loss experiments, the experimental data is reliable, validated both by the results obtained with the parallel plate heat exchanger and by reasonable agreement with the pin fin heat exchanger results obtained by Chyu.

3.5.3 Overall Thermal Performance

As explained in Chapter 1 : Introduction, the performance of micro pin fin heat exchanger can only be assessed after including the penalty effects related to friction losses. The overall thermal performance parameter η as defined in Equation 1-2 was

calculated and plotted in Figure 3-6.

According to the plot, at any Reynolds number η is strictly larger than 1.0 meaning that the micro pin fin heat exchanger performance always exceeds the parallel plate counterpart. Since η increases (from 1.35 to 1.78) with increasing Reynolds numbers, the micro pin fin heat exchanger is best applied when mass flow rates of coolant are the largest.

The logical continuation of this research would be to optimize the pin fin array configuration in order to produce the best performance.

3.6 Model Prediction for Gas Turbine Blade Cooling

The following model scenario is used to predict the cooling effectiveness of the flat micro heat exchanger.

A heat exchanger consisting of a pin fin array identical to that described earlier covers a turbine blade airfoil. The outer surface (or shroud) of the airfoil is heated via radiation and convection by combustion gases at T_G. The effective convection coefficient at the combustion gas-shroud interface is labeled as $h_{external}$. Air from the compressor enters the micro heat exchanger at a temperature T_C and pressure P_C typical of modern gas turbine engines. The mass flow rate of coolant per unit depth and the specific heat are respectively $\dot{m}'$ and C_p. The temperature of the coolant increases as the coolant travels through the heat exchanger. The effective convection coefficient $h_{effective}$ defined earlier as h in Section 3.3.2 couples the heat transfer between the shroud and the coolant. A schematic of the model is shown in Figure 3-7.

In this model, one-dimensional conduction in the shroud and an adiabatic blade surface are assumed. An average overall heat transfer coefficient per unit width of the

channel U can be defined as shown by Equation 3-26 after neglecting the conduction resistance.

$$U = \frac{1}{\frac{1}{h_{effective}} + \frac{1}{h_{external}}}$$

Equation 3-26

An energy balance applied to the coolant using the first law of thermodynamics yields a differential equation integrated in Equation 3-27 as a function of $T_{coolant}(x)$. The use of thermal resistances yields Equation 3-28, which provides the temperature of the shroud $T_{shroud}(x)$. Both $T_{coolant}(x)$ and $T_{shroud}(x)$ are a function of the mass flow rate $\dot{m}'$.

$$T_{coolant}(\mathrm{x}) = T_G - (T_G - T_C)\exp\left(\frac{-U \cdot x}{\dot{m}' \cdot C_p}\right)$$

Equation 3-27

$$T_{shroud}(x) = \frac{T_G \cdot h_{external} + T_{coolant}(x) \cdot h_{effective}}{h_{external} + h_{effective}}$$

Equation 3-28

By using Equation 1-1 with $T_{shroud}(x)$ as T_W the cooling effectiveness as a function of the downstream location x, $\varepsilon(x)$, can be predicted.

In a typical gas turbine T_G, T_C, P_C and $h_{external}$ are respectively 2200 K, 700 K, 20 atmospheres and 2500 W/m^{2}K. By using $h_{effective}$ values from Table 3-7 (air cooled micro pin fin heat exchanger results), the cooling effectiveness is calculated at two distances x_1= 1 cm and x_2= 2 cm downstream from the coolant injection location. The MathCAD calculation sheets are presented in Appendix H and the results are summarized in Table 3-11.

As shown in Table 3-11, the shroud temperature varies, as expected, with mass flow rate and the distance x from the coolant injection point. If the shroud temperature at x_1= 1.0 cm is chosen as the characteristic temperature of the shroud, then the analysis above provides cooling effectiveness values ranging from ε = 0.40 to ε = 0.72. The optimal combination of mass flow rate and heat exchanger design is a function of numerous variables (material properties, mission, etc.). This study is beyond the scope of this dissertation.

Table 3-11: Model Predictions for gas turbine blade cooling

$\dot{m}'$ (kg/m.s)	$h_{effective}$ (W/m^{2}K)	$T_{coolant}(x_1)$ (K)	$T_{coolant}(x_2)$ (K)	$T_{shroud}(x_1)$ (K)	$T_{shroud}(x_2)$ (K)	$\varepsilon(x_1)$	$\varepsilon(x_2)$
0.085	2617	1013	1261	1593	1720	0.40	0.32
0.172	5910	908	1087	1292	1418	0.61	0.52
0.259	8602	862	1007	1163	1275	0.69	0.62
0.342	9804	849	984	1124	1231	0.72	0.65

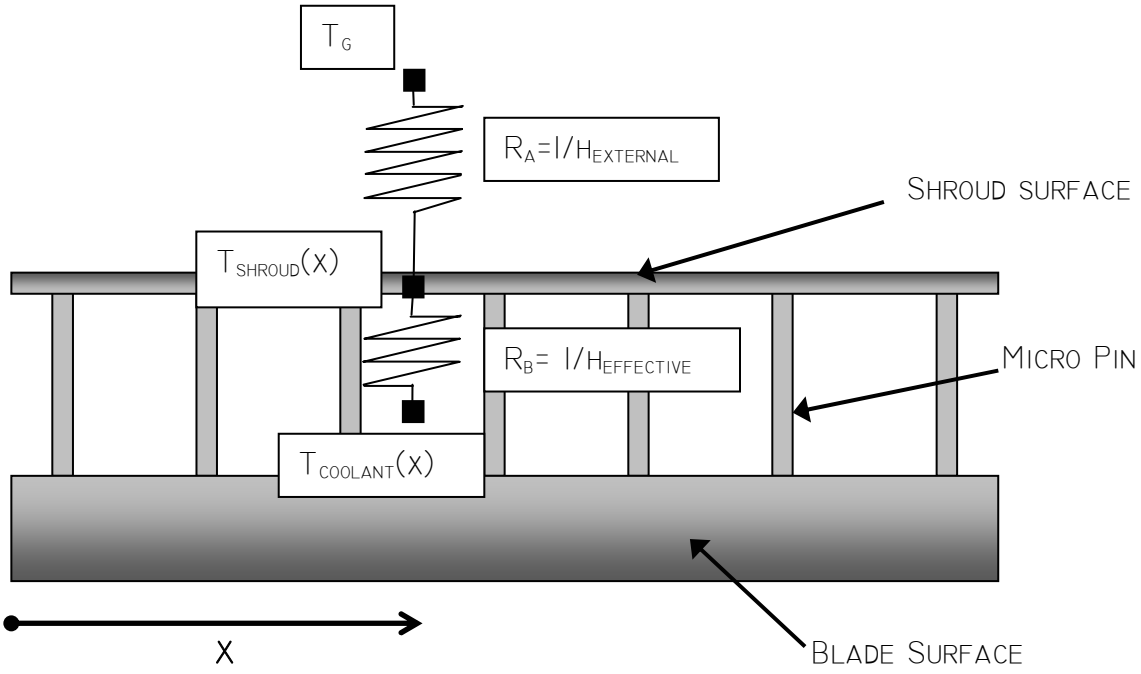

Figure 3-7: Schematic of thermal resistances in the turbine blade model

CHAPTER 4 : FABRICATION OF THE CURVED METAL MICRO HEAT EXCHANGER

The traditional LIGA micromachining process was modified again in order to fabricate a curved micro heat exchanger. The heat exchanger consists of a Nickel shroud supported by an array of micro pin fins electroplated onto the outer surface of a stainless steel tube. The new process presented in this chapter involves bending a lithographically patterned sheet of PMMA to the shape of the tube as an electroplating template.

4.1 Design Specifications

The heat exchanger configuration is as depicted in Figure 4-1. The hot fluid is sent across the outer diameter of the shroud. Cooling access and exhaust features for the micro channel are included in the design. The cold fluid enters the micro channel from the inside of the tube through an array of holes drilled in the wall of the tube around the leading edge and leaves through a slot situated at the trailing edge of the shroud. An important design aspect is the presence of a sidewall at the longitudinal edges of the heat exchanger in order to enclose the flow from the leading to the trailing edge. It can be seen from the three-dimensional view depicted in Figure 4-2 that two symmetry planes characterize the heat exchanger. The first plane contains the symmetry axis of the tube, the leading and the trailing edge of the shroud. The second plane (referred as “mid-plane” subsequently in this dissertation) is orthogonal to the first plane and intersects the symmetry axis of the tube in its middle.

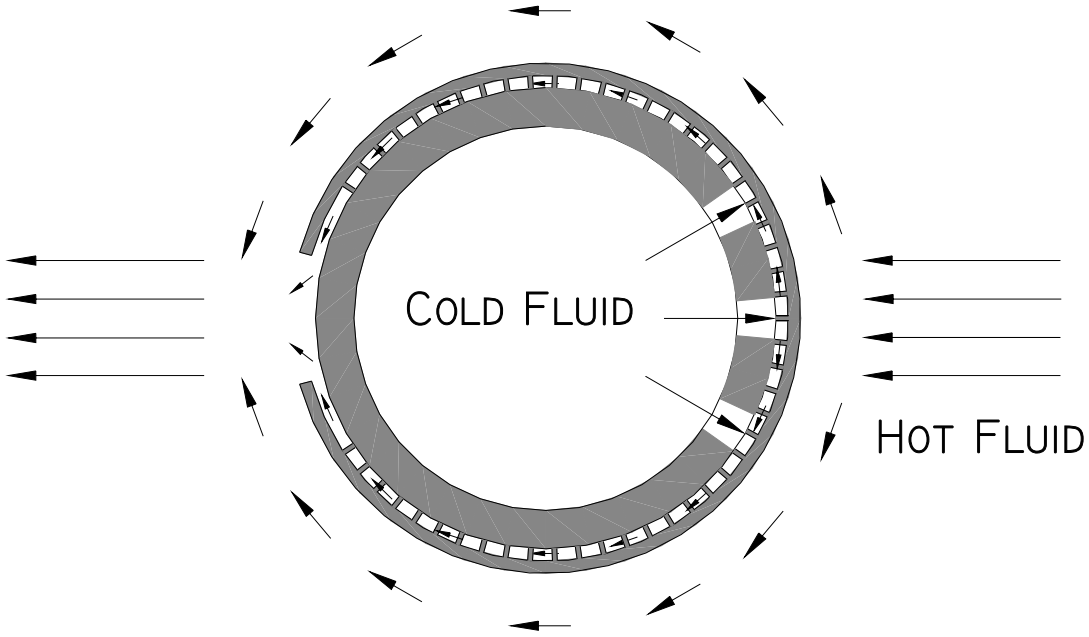

Figure 4-1: Curved metal heat exchanger flow configuration (cross section)

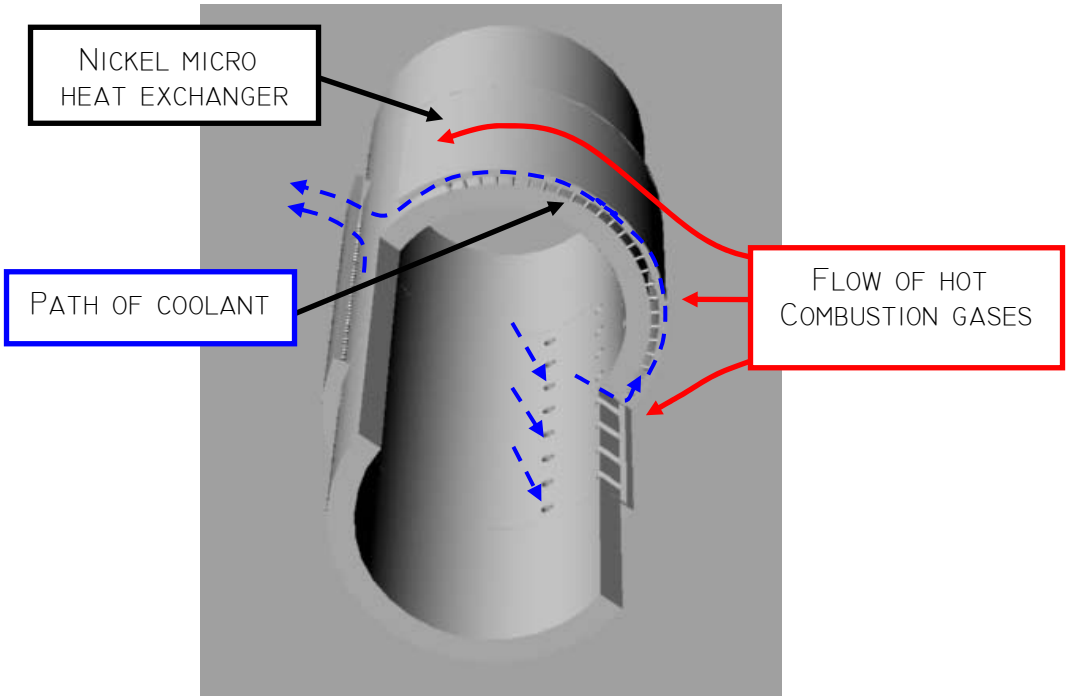

Figure 4-2: 3-D view of the curved metal heat exchanger on a tube

The flow configuration shows that the shroud is characterized to two types of cooling:

- Forced convection internal cooling in the micro channel
- Impingement cooling against the inner surface of the shroud at the leading edge.

Dimensional parameters of the heat exchanger are based on different reasons. Importantly, array arrangement, pin diameter and pin center-to-center spacing are parameters imposed by the available choice in X-ray masks at the time the heat exchanger was manufactured. Therefore these parameters are different from those associated with the flat metal heat exchanger. The choice of a PMMA thickness with a reasonable exposure time dictated the height of the micro pins, and consequently the channel height. The micro pin fin array built on the tube is characterized by the following dimensions:

- Array arrangement: in-line
- Pin diameter: 200 μm
- Pin height: 500 μm
- Streamwise pin center-to-center spacing: 1000 μm
- Spanwise pin center-to-center spacing: 1000 μm

The perimeter and longitudinal dimensions of the shroud are both 5.0 cm due the scanning length limitations of the X-ray exposure facility. As a consequence, the diameter and length of the tube are respectively set to 19.1 mm (¾ inch) and 12.1 cm (4¾ inch) in order to provide sufficient outer surface area to electroform the heat exchanger (5.0 cm by 5.0 cm).

The thickness values of the tube wall, channel sidewall and shroud were arbitrarily set to 1.6 mm (1/16 inch), 500 μm and 500 μm. The array dimensions of the bleed through-holes on the surface of the tube can be justified by the range of coolant mass flow rates of interest (from 0.001 to 0.01 kg/s) and are given as:

- Hole diameter: 1.6 mm (1/16 inch)
- Number of holes in the axial direction: 8
- Center-to-center spacing in the axial direction: 6.4 mm (¼ inch)
- Number of holes in the angular direction: 3
- Center-to-center spacing in the angular direction: 30 degrees

The parameters provided above can be optimized in order to improve the distribution of coolant (increase the number of holes, decrease their diameter, etc.) but this aspect is beyond the scope of this study.

The choice of material is similar to the choice made for the flat metal heat exchanger. The shroud, channel side-walls and the array of pins are a continuous metal part made of pure electroplated Nickel. However, the ¾-inch diameter tube is made of stainless steel 316.

The curved metal heat exchanger was produced using a procedure described in the following sections.

4.2 Manufacturing Procedure (Modified LIGA on a Curved Surface)

A new LIGA manufacturing procedure was developed in order to customize the flat micro pin heat exchanger to the shape of an outer tube. It was found at LSU [14],[32],[37],[38] that clamping a free standing lithographically patterned sheet of PMMA

onto a planar or curved conductive substrate instead of establishing a chemical bond could give well-defined microstructures. This method, which leads to negligible plating under the PMMA template, was improved to include all the heat exchanger design specifications.

The following subsections describe the steps of the procedure leading to the final product.

4.2.1 Substrate Preparation

The stainless steel 316 conductive substrate used to support the micro posts and the shroud was prepared before electroplating. Unlike the case of the flat metal heat exchanger, the metal substrate is part of the final product and a strong bond between the substrate and the electroformed micro posts is desired. The subsequent paragraphs provide a description of the steps guiding to an electroplating substrate with a chemically primed surface.

4.2.1.1 First Machining Step

A round bar of stainless steel 316 with a diameter greater than 19.1 mm (¾ inch) is ordered from a metal supplier and represents the starting point of the process. The bar is first bored with a 1.6 cm (5/8 inch) diameter through-hole turning the bar into a tube, and an array of 24 holes with 1/16 inch diameters (with the specifications given in Section 4.1) is drilled in the wall. Note is made that the outer diameter of the sample is maintained greater than 19.1 mm (¾ inch). The metal piece is cleaned with soap and tap water before the next step.

4.2.1.2 PMMA Filling

This procedure will prevent the electrolyte from flowing into the hollow volume of the tube by leaking though the PMMA micro patterns and the 1/16 inch though holes located on the surface of the tube during the subsequent electroplating step. The hollow volume of the tube and the 1/16 inch through-holes are filled with liquid PMMA, which solidifies and can be dissolved at the end of the manufacturing process.

The PMMA is first presented as a liquid mix of powdered PMMA and methyl methacrylate (MMA). Powedered PMMA and MMA can take several hours to dissolve but the amount of time may be reduced by increasing the temperature to 40ºC at the highest stirrer setting. Following that, benzoyl peroxide (BPO) and dimethyl aniline (DMA), respectively a hardener and a polymerization initiator, are added and thoroughly mixed. The final composition of the PMMA solution is provided in Table 4-1.

Table 4-1: Composition of the PMMA solution

Compound	Formula	Parts by weight
Methyl methacrylate *(MMA)*	$CH_2=C(CH_3)CO_2CH_3$	85
Poly(methyl methacrylate) *(Powdered PMMA)*	$[-CH_2C(CH_3)(CO_2CH_3)-]_n$	15
Benzoil peroxide *(BPO)*	$C_{14}H_{10}O_4$	1.5
N,N-dimethyl-aniline *(DMA)*	$C_8H_{11}N$	1.0

The stainless steel tube is slipped vertically around a 1/8 inch diameter stainless steel threaded rod in such a way that the bottom end of the tube rests against a metal washer secured to the threaded rod with a nut. After approximately 10 minutes, some of

the PMMA mix is poured into the upper end of the tube, when the mix is viscous enough to harden as it flows outside of the tube through the array of holes. The inside of the tube may be replenished with the left over PMMA mix to ensure that it is filled completely. Finally, a washer is placed onto the top end of the tube and secured with a nut.

The threaded rod, which is in electrical contact with the tube through the metal washers, will serve as an electrode connection during the electroplating process.

4.2.1.3 Second Machining Step

In order to remove the hardened PMMA bonded onto the outer surface of the tube and to reduce the outer diameter to 19.1 mm (¾ inch), the tube is machined using a lathe. A picture of the substrate at this stage of the process is shown in Figure 4-3.

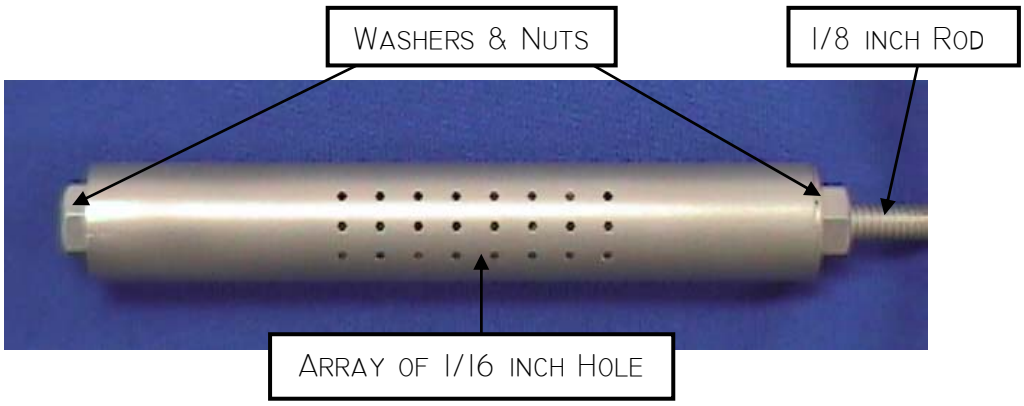

Figure 4-3: Stainless steel substrate prior to surface treatment

4.2.1.4 Surface Cleaning

Since roughness increases the bond between electroformed structures and substrate, the surface can be polished with sand paper or sandblasted. After immersing 20 minutes in an ultrasonic bath filled with detergent, the sample is successively rinsed

with tap water, de-ionized water, and isopropyl alcohol. Absolutely no acetone can be used otherwise it would dissolve the PMMA filler.

4.2.1.5 Wood Strike and C-12 Activator

A 4 μm thick layer of strongly adhesive Nickel is electroplated onto the surface of the stainless steel using the Wood strike bath [35]. The presence of the 4 μm thick layer of Nickel allows to increase the bond strength between the posts and the substrate.

The strong oxide layer located on the stainless steel passivates the surface and has to be removed using the original C-12 Activator (from Puma Chemical [26]). The substrate which represents the working electrode is placed in a C-12 activator bath of composition provided in Table 4-2. During 1 minute, using a general-purpose potentiostat (as in Section 2.3.7), a voltage difference of -2.0 V is applied between the working electrode and a stainless steel plate, which serves as counter electrode.

Note is made that the potentiostat can only apply a constant voltage difference between the working electrode and the reference electrode. Therefore, as advised by the manufacturer of the potentiostat, the reference electrode is wired to the counter electrode through a 1,000 Ω resistance.

After the activation process, the sample is immersed directly without rinsing into a Wood strike bath of composition given in Table 4-3. The sample is treated 6 minutes with the bath operating conditions described in Table 4-4 with a Nickel foil as counter electrode. In order to dissolve the abundantly generated hydrogen at the working electrode surface, agitation is maintained as high as possible.

Finally the sample is rinsed and stored until more processing is engaged.

Table 4-2: Composition of the C-12 activator solution [26]

Compound	Concentration (% per vol)
Concentrated C-12 activator	2.5
De-ionized water	97.5
Sulfuric acid (H_2SO_4)	Set pH=1.5

Table 4-3: Composition of the Wood strike bath [35]

Compound	Formula	Concentration (g/l)
Nickel chloride	$NiCl_2 \cdot 6H_2O$	240
Hydrochloric acid	HCl	80

Table 4-4: Wood strike bath operating conditions.

Temperature	Agitation	Filter porosity	Current density	Polarity	Operating mode
21-27°C	>600 RPM	1.6 μm	50 mA/cm^2	Negative	Galvanostatic

Table 4-5: Composition of the "GG" developer and rinse solutions [36]

Compound	Formula	Developer (% volume)	Rinse (% volume)
Diethylene glycol butyl ether	$H(OCH_2CH_2)_2O(CH_2)_3CH_3$	60	80
Morpholine	C_4H_9NO	20	0
Ethanolamine	$CH_2=C(CH_3)_2CO_2CH_3$	5	0
De-ionized water	H_2O	15	20

4.2.2 PMMA Micro Patterning

As mentioned earlier a free standing lithographically patterned sheet of PMMA needs to be created for further use as electroplating template. The lateral dimensions of the PMMA sheet, which was obtained from AIN Plastics Inc., are 5 cm by 5 cm square and the thickness 500 μm. The following sections depict the corresponding exposure and development procedures.

4.2.2.1 Exposure

The first requirement to ensure good quality PMMA exposure is that the minimum dose of energy absorbed in the exposed regions exceeds 3500 J/cm^3 (as mentioned in Table 2-1). This minimum absorption dose in exposed regions will allow complete dissolution in the subsequent step of LIGA. The second exposure requirement, which differs from the case of SU-8 photo resist, is that the upper side of the PMMA which faces incident X-rays does not exceed the damaging dose of 20,000 J/cm^3 (Table 2-1). This side of the PMMA, due to the law of absorption, accumulates more energy than the opposite side where the energy accumulated is the lowest. In other words, the top to bottom absorbed dose radio for PMMA has to remain lower than 5.7. To reduce the difference in doses absorbed between one side and the other side of the PMMA, a 15 μm Aluminum filter is used. The radiation dose needed for exposure was estimated using the DoseSim software.

The PMMA exposure was done with the XRLM-3 beamline at CAMD, when the storage ring energy was 1.5 GeV. For a thickness of 500 μm, with a 15 μm Aluminum filter, the required dose was 2589 mA*min/cm. Since the scan length was 2 inches, which corresponds to the lateral dimensions of the PMMA, the total exposure dose was 13153

mA*min, which represents approximately 130 minutes of exposure for an average storage ring current of 100 mA. According to the computer program, the top to bottom absorbed dose ratio for the PMMA is 4.0, which meets the second exposure requirement for PMMA.

4.2.2.2 Development

The step subsequent to X-ray exposure is the development of the exposed regions in the PMMA, using the "GG" developer and the rinse solution [36]. The solution compositions are given in Table 4-5. The following procedure allows carrying out the development of the irradiated PMMA regions:

- 40 minute immersion in the "GG" developer with medium agitation
- 90 minutes immersion in the rinse solution with medium agitation
- approximately 2 hour long immersion in de-ionized water

Subsequent to development, the PMMA is patterned with an array of through holes.

4.2.3 PMMA Wrapping Procedure

The lithographically patterned PMMA sheet has to conform to the shape of the prepared stainless steel tube. Heating at a temperature of 155°C causes PMMA to become flexible. Therefore, a PMMA wrapping apparatus, simply consisting of a 19.1 mm (¾ inch) in diameter temperature controlled aluminum cylinder was made to shape the PMMA to the desired geometry. A picture of the wrapping apparatus is shown in Figure 4-4 and the corresponding electric wiring diagram is similar to the one designed for the SU-8 casting jig (Section 2.3.4).

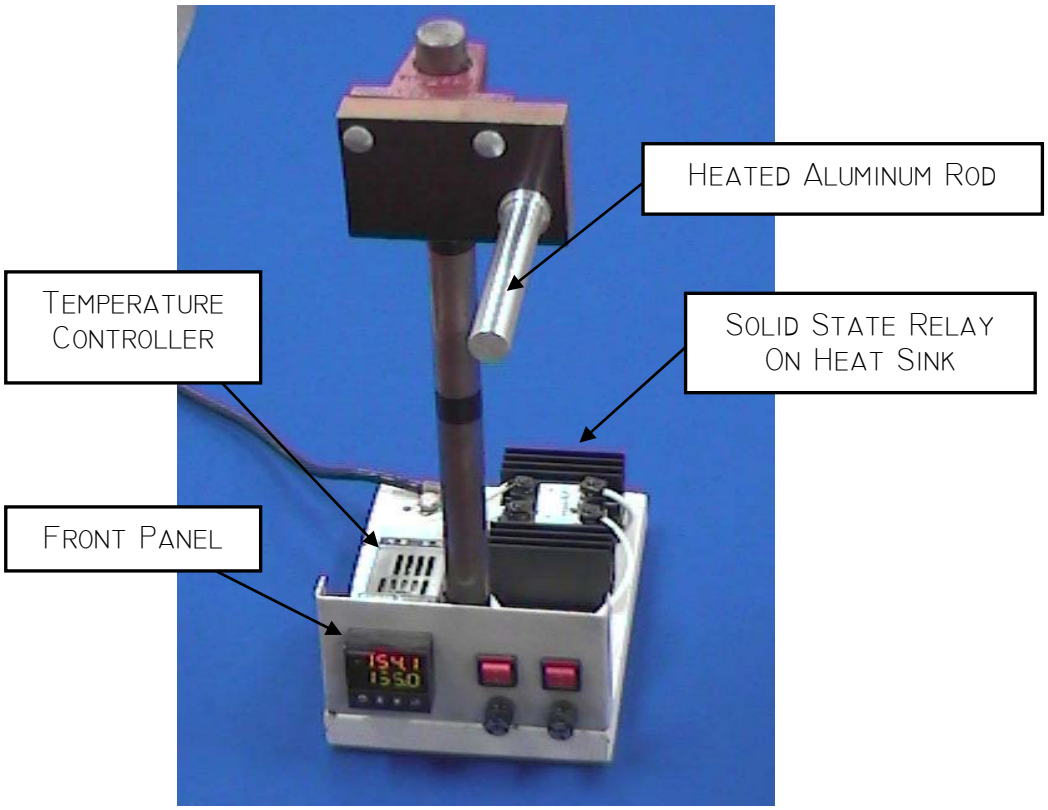

Figure 4-4: PMMA wrapping apparatus

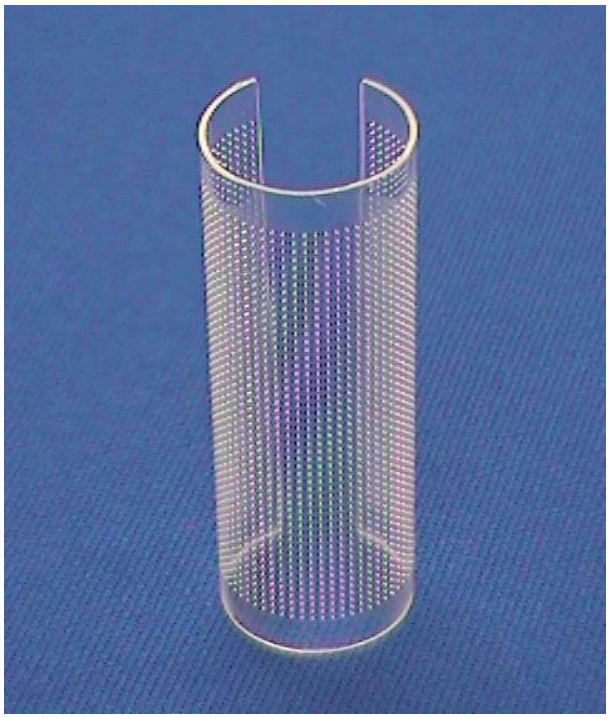

Figure 4-5: PMMA sheet conformed to the shape of a cylinder

The wrapping procedure is done manually and requires using a particular kind of gloves. ThermaPrene^{TM} gloves were chosen because they are excellent in protecting the hands against hot temperatures and because the layer of insulation is thin enough to ensure accurate handling of the PMMA around the heater cylinder using the fingers.

Once the temperature controller display reads 155°C, the developed square sheet of PMMA, initially at room temperature, is carefully brought into contact with the cylinder [37]. The initial line of contact between the PMMA and the cylinder is a tangent to the cylinder and parallel to two sides of in the middle of the square PMMA sheet. Slowly the PMMA becomes flexible as its temperature increases. One half the PMMA is wrapped around the cylinder, then the other. Finally, the PMMA coated Aluminum cylinder is allowed to slowly cool to room temperature. The edges of the PMMA are pressed firmly onto the cylinder during the temperature decrease from 155°C to 120°C.

The curved PMMA piece shown in Figure 4-5 is properly stored in order to prevent dirt or dust from entering and obstructing the micro patterns.

4.2.4 Nickel Electroplating

This section describes the preparation done prior electroplating and the actual electroplating step.

4.2.4.1 Pre-electroplating Preparation

The cylinder shaped PMMA part is positioned onto the metal stainless steel substrate, carefully aligned and clamped using three small size cable ties spaced evenly along the axial direction of the tube.

Then, electroplating tape is applied in the areas where electroplating is not desired. In particular, masking is done at the trailing edge of the tube, over the surface

delimited by the longitudinal ends of the PMMA sheet. In order to allow Nickel growth for the micro channel side wall, care is taken in leaving tape-free space along the two other edges of the PMMA. This unmasked surface is purposely oversized but the final dimensions will be reduced later. A picture of the resulting prepared substrate is shown in Figure 4-6 and Figure 4-7.

In order to eliminate Nickel passivation which is associated with the growth of a strong oxide over the surface of the 4 μm thick electroformed Nickel layer, the PMMA coated substrate is treated again with the C-12 activator. Care is taken in initially removing the air trapped inside the PMMA micro patterns. For this reason, the electroplating substrate is immersed into a C-12 activator bath located inside a vacuum vessel. Then air is removed with a vacuum pump using 4 cycles while shaking the vessel. The subsequent activation step is similar to the procedure in Section 4.2.1.

A small amount of hydrogen usually remains trapped in the PMMA micro cavities due to hydrogen generation induced by C-12 activation. In order to clear the micro cavities from any gases, the activated electroplating substrate is immersed in a 5 g/l lauryl sulfate solution and degassed by applying 4 vacuum cycles.

4.2.4.2 Electroplating Procedure

The electroplating procedure of the PMMA coated substrate is to a certain extent similar to the electroplating procedure used for making the flat heat exchanger. The electroplating bath is a Nickel sulfamate bath and is prepared in the same conditions (Table 2-3 and Table 2-4). However, due to the geometry of the working electrode, the electric field in the electrolyte has to be axisymmetric.

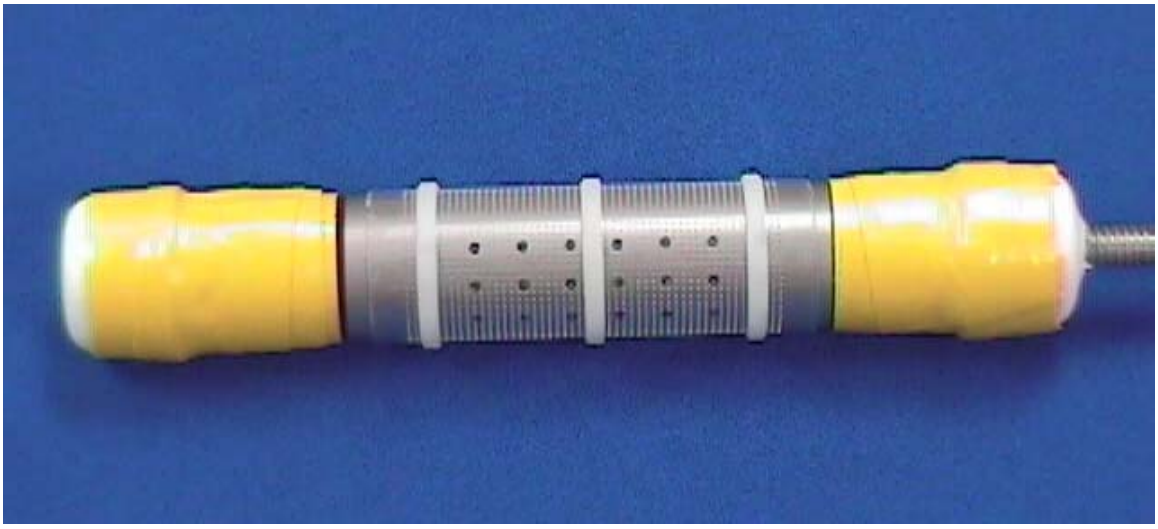

Figure 4-6: PMMA coated substrate before electroplating (Overall view)

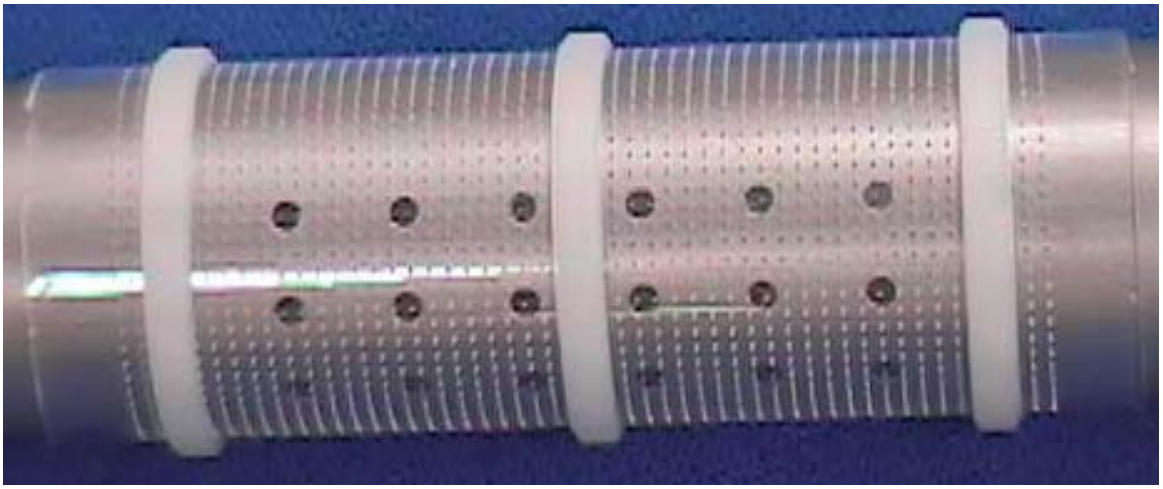

Figure 4-7: PMMA coated substrate before electroplating (Close-up view)

As a consequence, the counter electrode is a sulfurized Nickel filled titanium basket which completely surrounds the working electrode. Once the electrodes are connected to the potentiostat and the total current is programmed to match up a current density of 20 mA/cm^2, electroplating is initiated.

After 8 hours into the process, approximately 200 μm tall Nickel micro posts have been electroformed. Since their presence is enough to anchor the PMMA against the surface of the tube, the sample is taken out of the plating bath and the 3 cable ties are removed.

Prior to re-immersion in the Nickel sulfamate electroplating bath, the sample is vacuumed into activator, activated, and vacuumed into the lauryl sulfate solution in the same manner as described earlier. The reason for this is to allow the holes previously obstructed by the cable ties to fill up with metal when electroplating is resumed.

Electroplating is carried out with the same initial current until all the micro holes are filled and start to overplate. Then, as in the case of the flat metal heat exchanger, the total current is augmented due to the increase of metal surface area in order to maintain the current density as close to 20 mA/cm^2 as possible. Sustaining the electroplating process for 5 days allows to electroform overplated Nickel exceeding the desired shroud thickness of 500 μm.

At the end of this step, the sample is withdrawn from the solution and rinsed with tap water.

4.2.5 Post Processing Steps

The sample proceeds through the following steps before becoming the final product.

4.2.5.1 Machining

After pealing the electroplating masking tape off, the two nuts are unscrewed in order to remove the washers and the threaded rod. The PMMA is not removed at this point as it provides protection to the microstructures. The sample is machined on a lathe in order to match the dimensions of the overplated layer of Nickel to desired values given in the specifications in Section 4.1. In particular, the outer diameter of the shroud is made to 21.05 mm and the thickness of the sidewalls is reduced to 500 μm.

4.2.5.2 PMMA Removal

In order to strip away the solidified PMMA filling the inside of the tube and the bent PMMA sheet situated in the micro channel, the sample is placed in a beaker filled with acetone. The container is immersed in an ultrasonic bath in order to accelerate dissolution of the polymer while acetone is completely refreshed approximately every 3 hours.

After the PMMA present inside the stainless steel tube has disappeared, one end of the stainless tube is capped while the other end is connected to a mechanical PTFE-diaphragm pump head. The pump head is made of materials which permit transfer of aggressive organic solvents. Finally, a flow of acetone is pumped through the micro channel which ensures that absolutely all the PMMA has been removed from the heat exchanger.

Pictures and measurements of the sample are presented in the next section.

4.3 Results

Pictures of a Nickel micro pin fin heat exchanger without side walls are provided because they offer better visibility of the micro posts present in the micro channel.

Figure 4-8 shows a cross section of the micro pin fin array on the surface of a stainless steel tube whereas Figure 4-9 depicts an overall view. Figure 4-10 which corresponds to a picture of the heat exchanger after it was sliced with a wire EDM machine, clearly shows the micro pin fins connecting the tube and the Nickel shroud.

In addition, dimensions of the curved metal heat exchanger with side walls were taken. The outer diameter of the tube and the inner diameter of the shroud (which corresponds to the outer diameter of the bent PMMA after it is clamped) were measured before electroplating with a digital caliper. The diameter and axial spacing of the micro posts along with the other measurements are compiled in Table 4-6.

It is emphasized at this point that the manufacturing technique described in this chapter is successful in building micro heat exchangers on convex surfaces only. This restriction is related to the fact that the micro patterned sheet of PMMA can only be clamped on such surfaces.

Table 4-6: Final dimensions of the curved micro pin fin heat exchanger

Feature	tube outer diameter	shroud inner diameter	pin diameter	axial pin spacing
Dimension (mm)	19.05	20.05	0.2	1.0
Tolerance (±%)	0.5	0.6	2.5	0.5

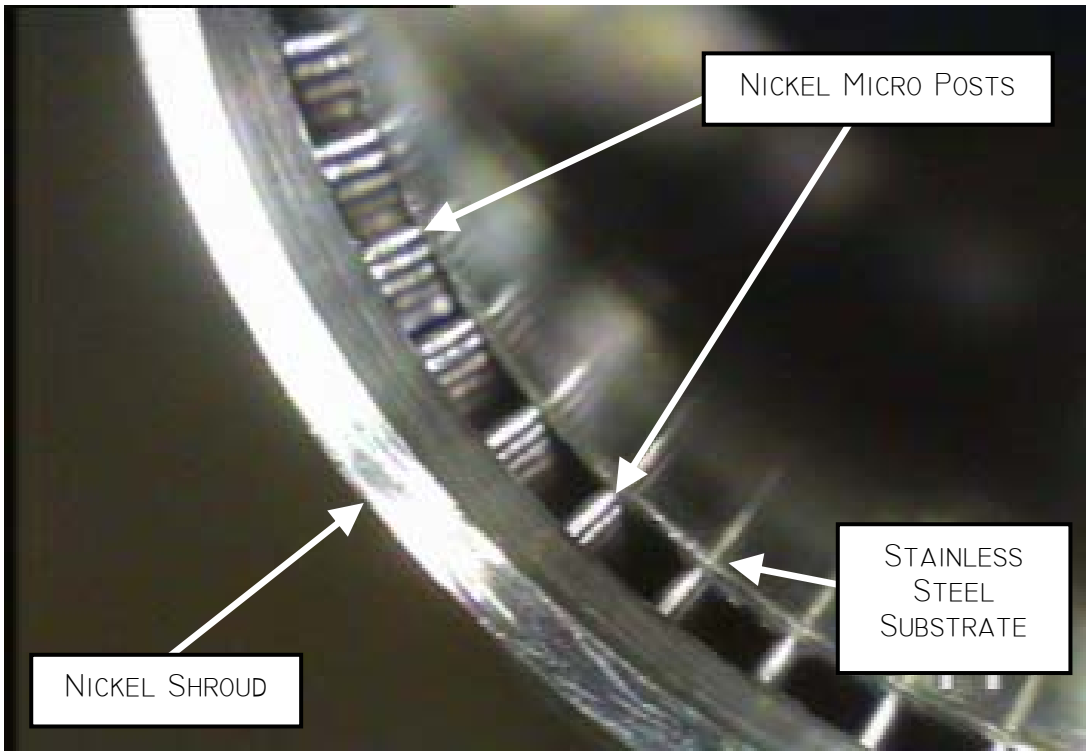

Figure 4-8: Curved heat exchanger without side walls on a stainless steel tube (Cross sectional view)

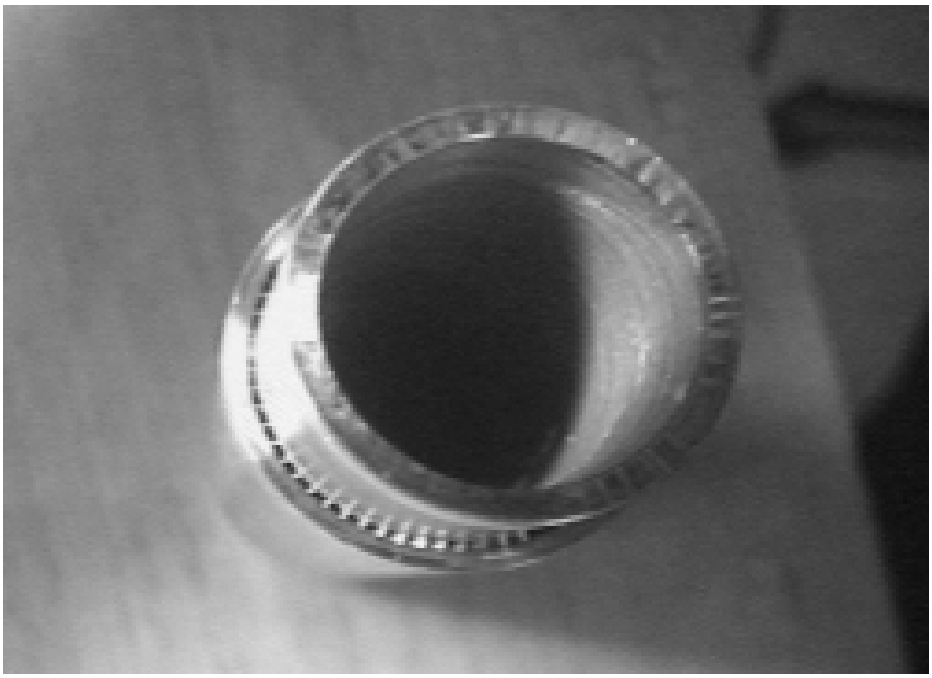

Figure 4-9: Curved heat exchanger without side walls on a stainless steel tube (Overall view)

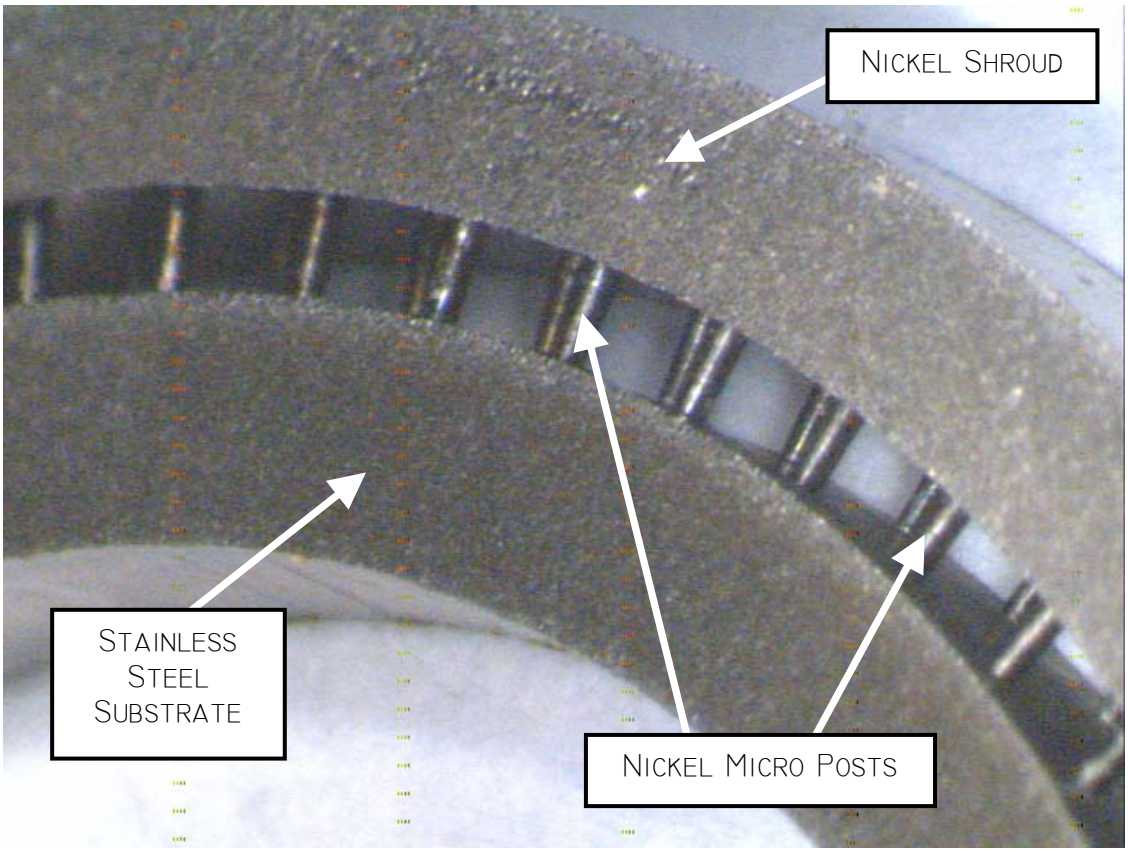

Figure 4-10: Curved metal heat exchanger sliced with a wire EDM machine.

CHAPTER 5 : EXPERIMENTAL STUDY OF THE CURVED METAL MICRO HEAT EXCHANGER

In order to estimate the performance of the curved metal heat exchanger described in Chapter 4, an aero-thermodynamic testing facility capable of producing high temperature and pressure gases was constructed. The tube heat exchanger was instrumented with thermocouples and tested according to the flow configuration created in the preliminary design. This chapter deals with the experimental aspects of the study.

5.1 Experimental Facility

A testing facility comprising a combustion chamber and a wind tunnel (burner rig) was designed by the "Aero Thermodynamic Facility senior design project team", under the supervision of Dr. Ekkad and Dr. Acharya in the Department of Mechanical Engineering at LSU [48]. The experimental facility was constructed and installed in the LSU Engineering Annex building.

Flow conditions in the movable test section correspond to gas temperatures and pressures able to respectively attain 1000°F (550°C) and 120 psi (8 atmospheres). A supply of compressed air with pressures varying from 190 to 280 psi (13 to 19 atmospheres) is available for cooling the heat exchanger.

5.1.1 Overall Description of the Burner Rig

Gases with high temperature and pressure are created by the burning of fuel in compressed air rich environment inside a combustion chamber.

A compressed air supply system has been available in the LSU Engineering Annex for the past five years. Ambient air undergoes an increase in pressure using an Atlas Copco model GR110, 2 stage, rotary screw compressor which allows, according to the manufacturer, volumetric flow rates up to 475 ACFM at 290 psi (20 atmospheres). The compressed air is taken to a dew point -40ºF (-40ºC) and then filtered by a Pneumatech® model PS-500 Heatless Regenerative Desiccant type drier. Finally the dried and compressed air is stored in a 10 m^3 tank.

The fuel used for combustion is contained in a 25 gallon (95 liter) propane bottle. The volumetric flow rate of fuel is controlled using a compressed gas pressure regulator and monitored by a correlated flow meter from Cole Palmer Instruments (044-40ST tube with stainless steel float) joined with a calibration chart for propane. The fuel line is connected to the combustion chamber via a flashback arrester and check valve (AGA FR50) with the aim of protecting the propane tank from an accidental return of flame.

The fuel and compressed air line are connected to the facility depicted in Figure 5-1 and Figure 5-2. The following sections describe the components of the burner rig and their functions. The last section provides the material selection.

5.1.1.1 Ball Valve (Label 1 in Figure 5-1)

This hand operated ball valve (2-inch Watts Ball Valve) allows the facility to be totally disconnected from the compressed air storage tank when complete shutoff is desired.

5.1.1.2 Air Pressure Regulating Valve (Label 2 in Figure 5-1)

Uncontrolled variations in air pressure between the compressor and the facility due to compressor on/off cycles causes instabilities in the flow.

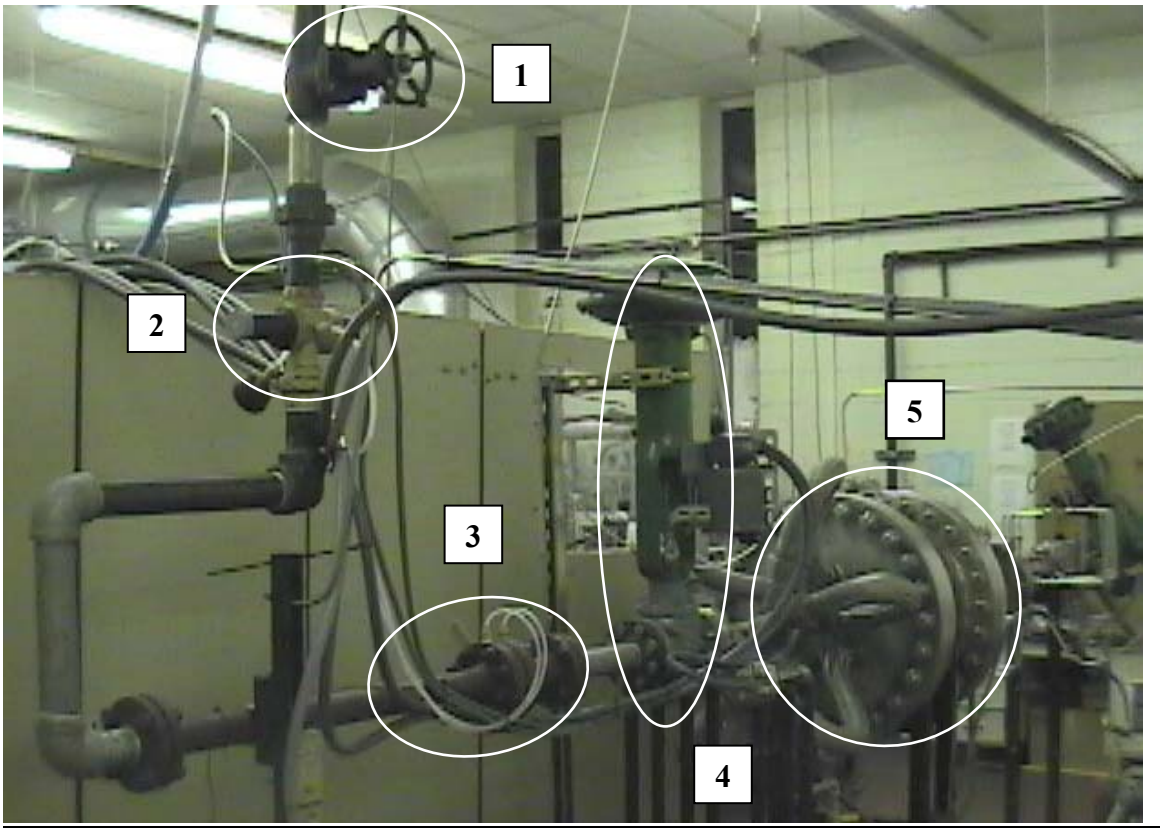

Figure 5-1: Upstream section of the burner rig

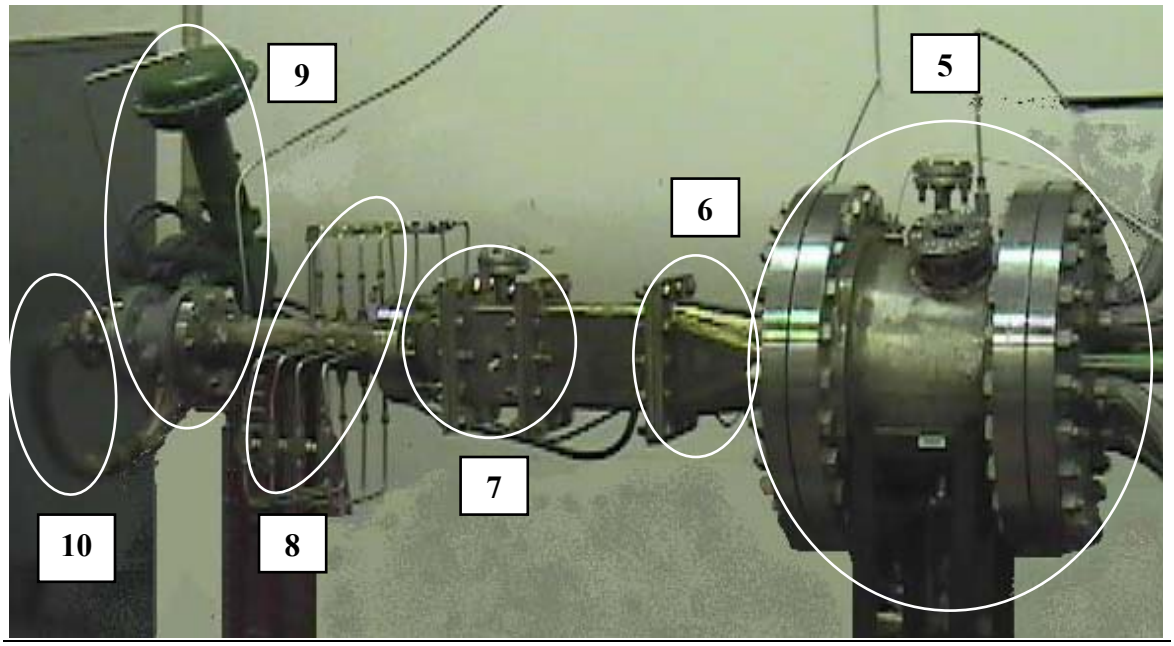

Figure 5-2: Downstream section of the burner rig

An air pressure regulating valve (Honeywell Braukmann D06G Valve), which was not included in the original senior project design, was added in order to maintain a constant air pressure. The values of the pressure exiting the regulator can range from 15 to 130 psi (1 to 9 atmospheres).

5.1.1.3 Meter Run (Label 3 in Figure 5-1)

This segment consists of a 0.8284-inch (21.04 mm) diameter orifice plate clamped between two flanged meter tubes of 2-inch (5.08 cm) line size. The pressure and temperature of the fluid upstream from the orifice, as well as the pressure drop across the orifice are measured. The collected measurements along with the orifice flow calibration chart (pressure drop versus mass flow rate for a given upstream pressure and temperature) provided by the manufacturer Fluidic Techniques® allow to determine the corresponding mass flow rate of air.

The length of the upstream and downstream meter tube, respectively 36 and 8 inches (0.9 and 0.2 m) were advised by the manufacturer, in agreement with ASME and ISO recommended lengths. An appropriate length of pipe upstream and downstream from the orifice plate ensures that a fully developed velocity profile flow free of swirls and vortices enters the orifice and that exit effects are minimized.

The metering run is a segment that was added to the original senior project design of the facility.

5.1.1.4 Upstream Control Valve (Label 4 in Figure 5-1)

This Fisher globe valve (2-inch ES Body) allows to reduce and adjust the pressure of the compressed air flowing downstream. The components of the valve are motioned using an actuator (Fisher model 667 size 45), a positioner (Fisher type 3582i pneumatic)

and a pressure controller (Fisher type 4160K). This control valve is connected to a control system including a process controller (Fisher-Rosemount DPR950) and a transmitter (Rosemount model 2088) which measures the pressure in the test section located downstream.

This process controller can be used either

- in automatic mode: to maintain a set pressure value in the test section
- or in manual mode: to merely open and close the valve

5.1.1.5 Combustion Chamber (Label 5 in Figure 5-1 and Figure 5-2)

A lean mixture of compressed air and propane are combusted in an Allison 501K Can Combustor. An electrical spark plug is used in the beginning of the experiment in order to ignite the combustible mixture. In addition, a quartz window fireye located on the side of the combustion chamber allows the operator to monitor the presence of the flame.

5.1.1.6 Nozzle (Label 6 in Figure 5-2)

The nozzle is a duct section which connects the circular exit of the combustion chamber to the rectangular inlet of the test section. The shape of the nozzle is designed such that the temperature and velocity fields associated with the products of combustion flow become uniform.

5.1.1.7 Test Section (Label 7 in Figure 5-2)

The test section is the duct segment where the studied sample is placed and where hot gas flow conditions are monitored throughout the experiment. As mentioned earlier, the pressure is measured using a transmitter (Rosemount model 2088). The temperature is

measured using a 1/8 inch (3.2 mm) diameter type K thermocouple. A more detailed description of the test section is provided further in this chapter.

5.1.1.8 Quenching System (Label 8 in Figure 5-2)

This duct section allows the combustion gases to be cooled down when their temperature exceeds 800ºF (430ºC), the maximum temperature withstandable by the exit control valve situated immediately downstream. When the temperature of the gases is too high, ambient temperature water is injected into the hot gases though 16 spray nozzles located on the wall of the 2 foot (0.6 m) long and 4 inch (0.1 m) diameter duct.

5.1.1.9 Downstream Control Valve (Label 9 in Figure 5-2)

This Fisher ball valve (4-inch V300 Rotary Valve) is used to apply a back pressure in the test section and the combustion chamber. The components of the valve are motioned using an actuator (Fisher model 1052 size 40), a positioner (Fisher type 3620J pneumatic) and a pressure controller (Fisher type 4160K). This control valve is connected to a control system including a process controller (Fisher-Rosemount DPR950) and a transmitter (Rosemount model 2088) measuring the pressure at a location immediately upstream from the valve. This process controller is used in manual mode only.

5.1.1.10 Exhaust Pipe (Label 10 in Figure 5-2)

This piping section starts from the downstream control valve, turns 90 degrees in the vertical direction and goes outside through the roof of the building. The exhaust simply serves to bring the products of combustion from the burner rig to the outside atmosphere.

5.1.1.11 Material Selection

The heated sections of the burner rig are made of L grade stainless steel 316 which provides good welding capabilities at the manufacturing stage and good mechanical properties during operating conditions at elevated temperatures. The nuts and bolts are made of stainless steel 316 whereas the cool sections of the rig are made of simple carbon steel.

All the components are bolted together and sealed using 3.2 mm (1/8 inch) thick flexible graphite sheets known under the name of Grafoil®. This gasketing material has reliable properties at elevated pressure and temperature.

The next paragraph provides a detailed description of the test section.

5.1.2 Description of the Test Section

The test section is a 316 stainless steel flanged duct with inner lateral dimensions of 7.6 cm (3 inches) and 20.3 cm (8 inches) and with a stream wise dimension of 15.2 cm (6 inches). The sample is mounted through the flanged orifice located on the 7.6 cm long side as shown in Figure 5-3 and Figure 5-4. The orientation of the parts in the test section allows the heat exchanger to be present in the region of the hot mainstream flow where the velocity and temperature fields are uniform, away from the wall boundary layers.

A pressure tap located on the side wall is connected to a pressure transmitter (Rosemount model 2088) and a 1/8-inch (3.2 mm) diameter thermocouple is inserted in the flow through a ¼-inch (6.4 mm) compression fitting mounted to the wall of the test section.

Pipe thread sealant with Teflon® (item 567 from Loctite Corporation) is applied to all the bolts threads, nuts and compression fittings used in the burner rig.

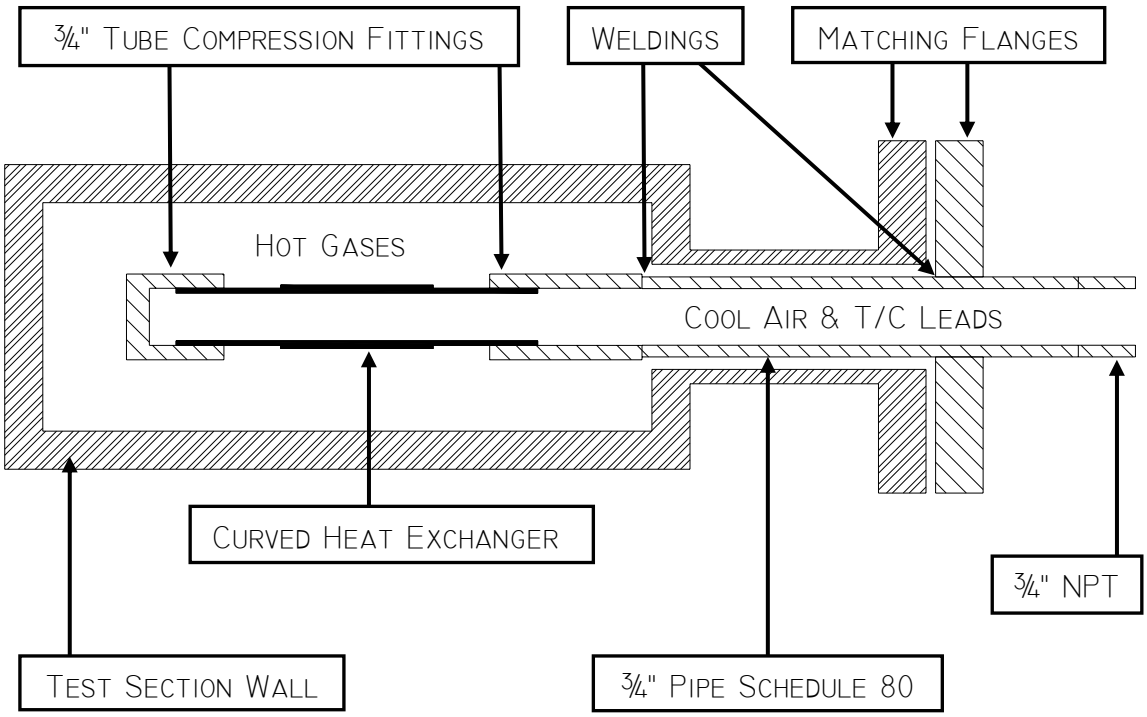

Figure 5-3: Schematic of a cross sectional view of the test section

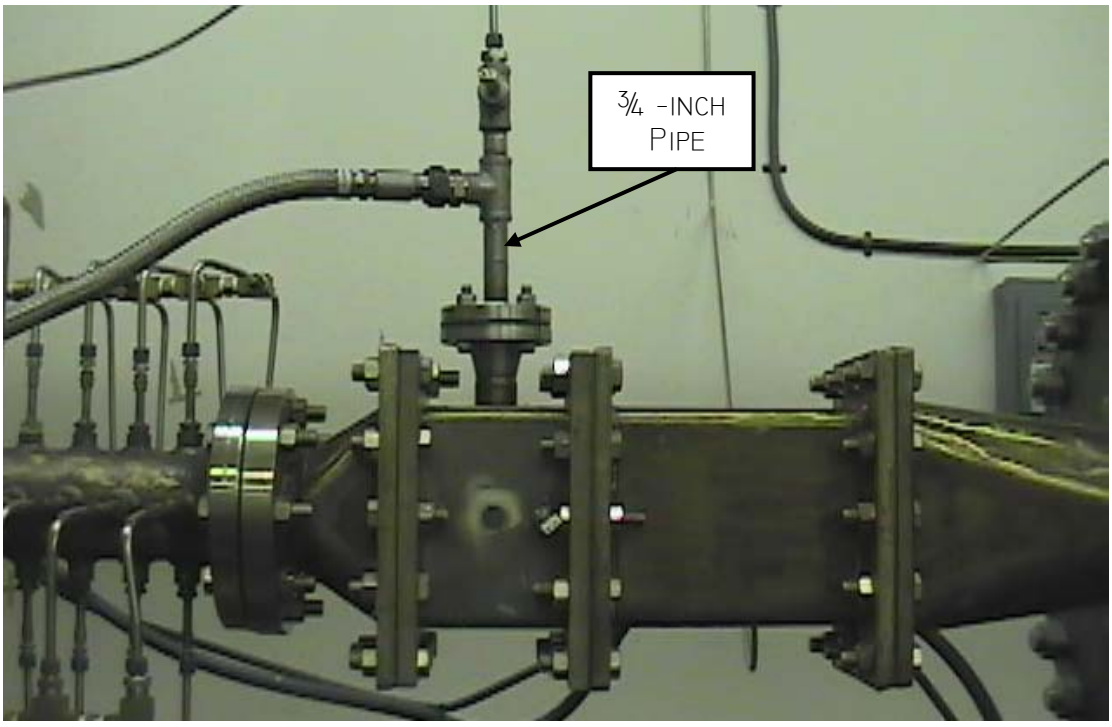

Figure 5-4: External view of the burner rig test section

Teflon® prevents galling, a phenomenon which appears when stainless steel welds to itself due to the combination of large compression mounting forces within the threads and elevated temperatures.

Note is made that a 1-inch (2.54 cm) stainless steel compression fitting was used prior to the installation of the flanged orifice currently welded to the side wall where the heat exchanger is inserted. The 1-inch compression fitting necessitated such a high mounting torque that intense forces were generated and galling problems occurred causing irreversible damage.

5.1.3 Heat Exchanger Installation

The manufactured heat exchanger is primarily instrumented with thermocouples. After the heat exchanger tube is mounted onto a supporting apparatus, the assembly is installed in the test section. Finally, the coolant piping and the thermocouple wires are respectively connected to a compressed air supply and the data acquisition system.

5.1.3.1 Instrumentation of the Heat Exchanger

Temperature measurements are necessary to calculate the cooling effectiveness of the heat exchanger. Type K Inconel sheath thermocouple wires with an outer diameter of 500 μm (0.020 inch) were installed in the mid plane cross section of the tube by qualified HITEC Corporation technicians [20].

As shown in Figure 5-5, a total of eight thermocouples have been positioned at the following different locations:

- Two thermocouples are located onto the inside surface of the stainless steel tube. Their positions are at 15 and 100 degrees from the leading edge. The reason for

using a small quantity of thermocouples is because the tube inner surface temperature is not included in the cooling effectiveness calculations.

- Five thermocouples are imbedded inside the Nickel-plated shroud. Four of them are on one side of the sample, 30 degrees apart from each other, starting on the leading edge. The fourth thermocouple is symmetrically opposed to the 3rd thermocouple, on the other side of the sample, at -60 degrees. The usage of the fourth thermocouple will help verify that the temperature distribution in the shroud is symmetrical with respect to a mid plane containing the leading edge.
- The eighth and last thermocouple is positioned at the trailing edge 1.3 mm (0.05 inch) from the surface of the tube and captures the temperature of the coolant exiting the channel.

The leading edge and trailing edge sides of the instrumented tube heat exchanger are shown in Figure 5-6 and Figure 5-7. All the thermocouples wires converge to the interior of the tube and exit the heat exchanger through the path used by the incoming compressed air. Figure 5-8 shows the thermocouple wires exiting tube heat exchanger.

Since the exiting coolant mixes directly with the mainstream, a box shaped like a converging nozzle was added as shown in Figure 5-9. The presence of the box serves to confine the coolant exhaust around the thermocouple located at the trailing edge and also serves to isolate the coolant from the hot mainstream flow. The box is glued to the heat exchanger with high temperature metal adhesive (Durabond 954) purchased from Cotronics Corporation. The adhesive can withstand up to 2000ºF (1100ºC).

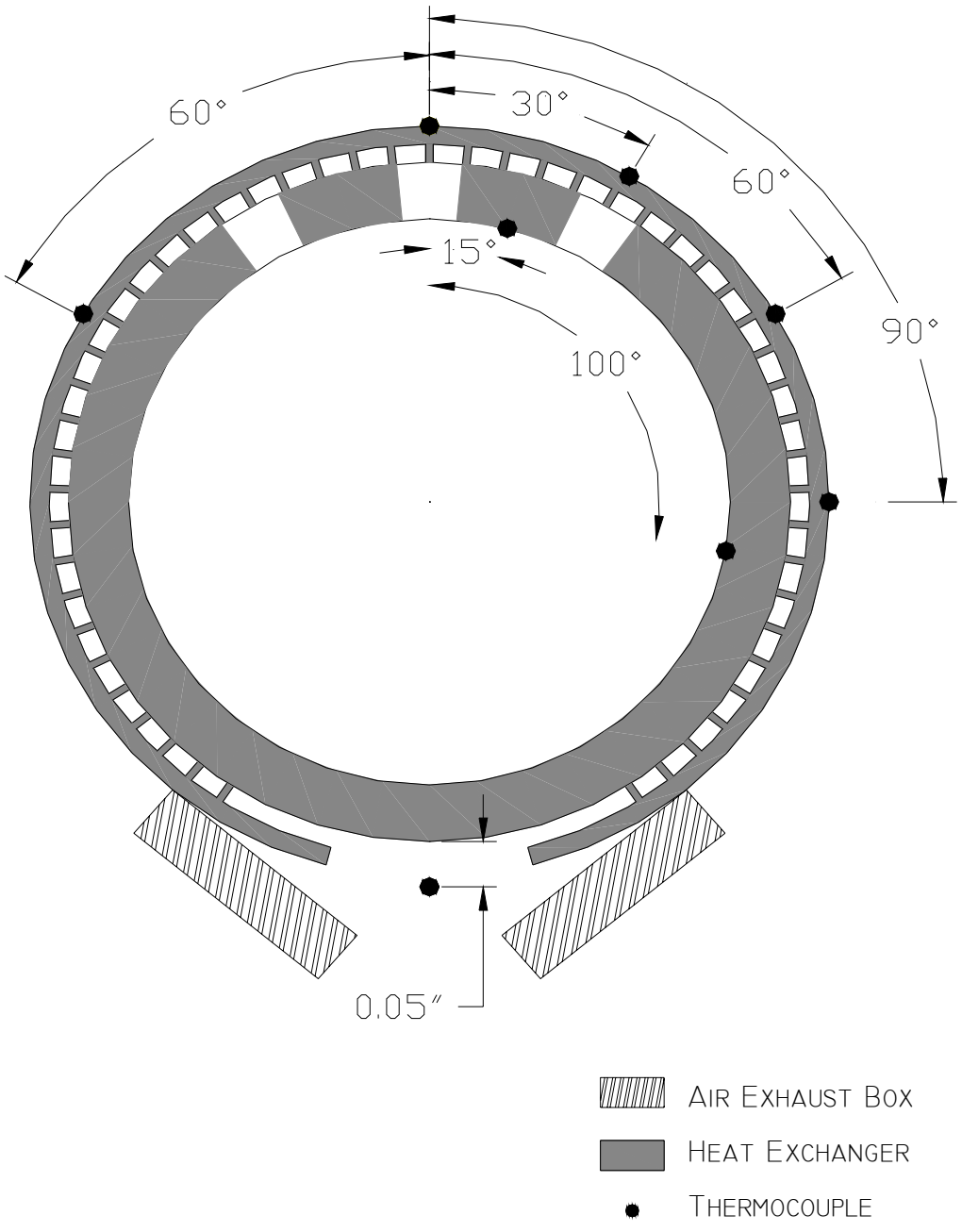

Figure 5-5: Location of the thermocouples on the curved heat exchanger

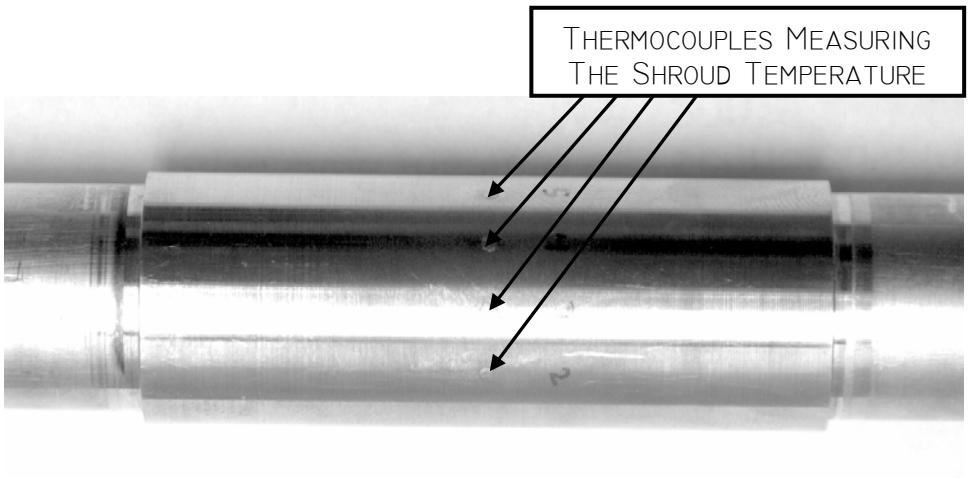

Figure 5-6: Leading edge of the tube heat exchanger

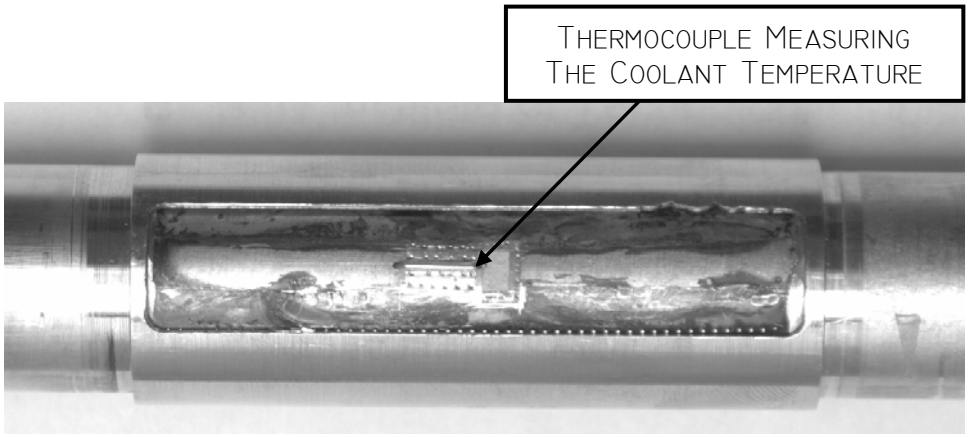

Figure 5-7: Trailing edge of the tube heat exchanger

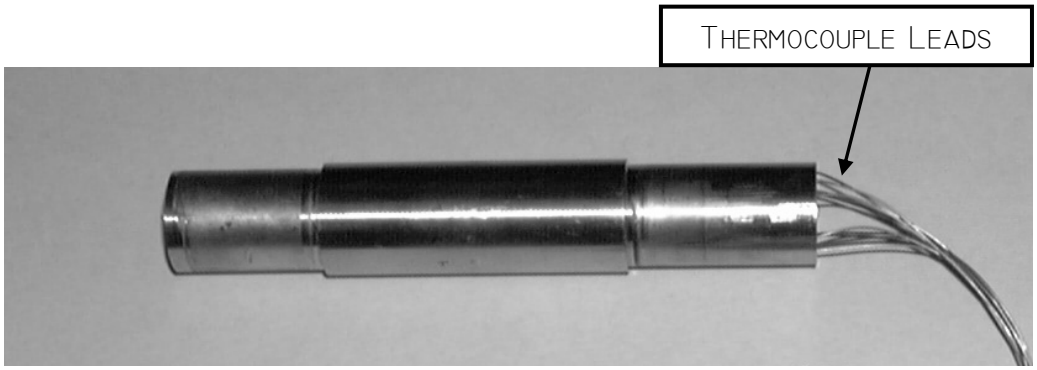

Figure 5-8: Thermocouple wires exiting tube heat exchanger

5.1.3.2 Installation of the Heat Exchanger in the Test Section

As sketched in Figure 5-3 and shown in Figure 5-10, the heat exchanger is mounted onto a supporting system. The supporting system can be described as an 8-inch long and ¾-inch diameter schedule 80 pipe to which the following modifications were made:

- A 1-¼" nominal pipe size 150 pound blind 304 stainless steel flange, matching the test section orifice flange, was drilled with a ¾-inch diameter hole, slipped around the ¾-inch diameter pipe and welded to it.
- A ¾-inch tube compression fitting was welded to one end of the pipe.
- ¾-inch NPT threads were machined to the other end of the pipe

Once the thermocouple wires are passed all the way through the ¾-inch pipe, the heat exchanger tube is attached to the pipe by tightening the welded compression fitting. In order to completely seal the cavity inside the tube, the other extremity is closed using an end cap compression fitting, as depicted in Figure 5-9. Finally the heat exchanger support apparatus is inserted through the flanged orifice of the test section, the flanges are sealed with Grafoil® and tightened using nuts and bolts.

5.1.3.3 Connection to a Compressed Air Supply and a Data Acquisition System

The ¾-inch diameter flanged pipe which is attached to the heat exchanger and which extends through the wall of the test section provides access to both the thermocouple leads and the coolant path. In order to separate the thermocouple lead and the coolant entrance, a ¾-inch Tee is placed onto the threaded end of the pipe as shown in Figure 5-10.

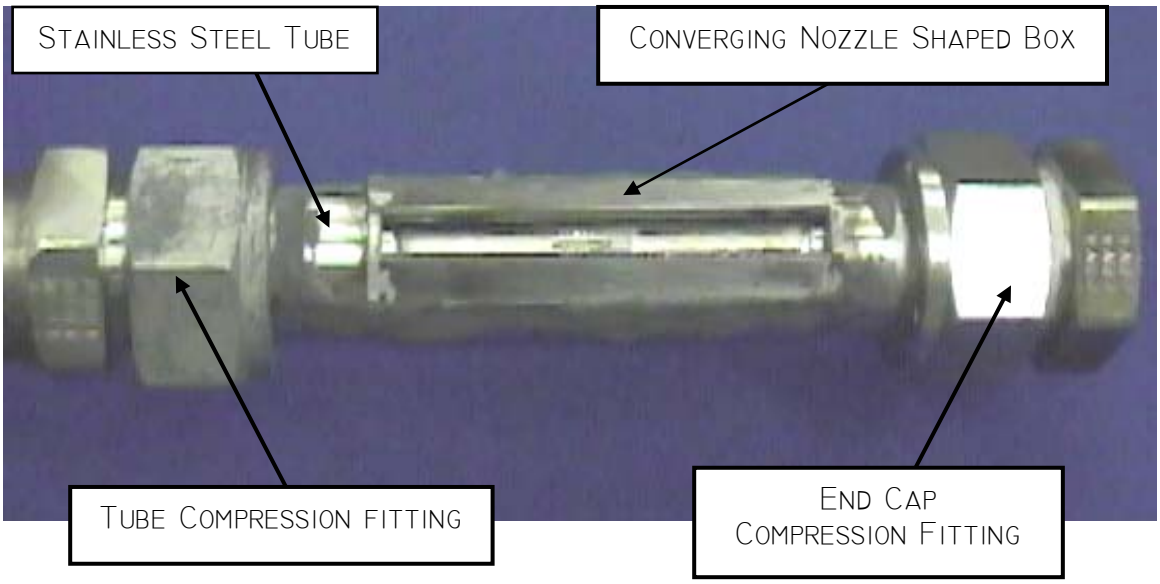

Figure 5-9: Converging nozzle bonded to the trailing edge of the heat exchanger

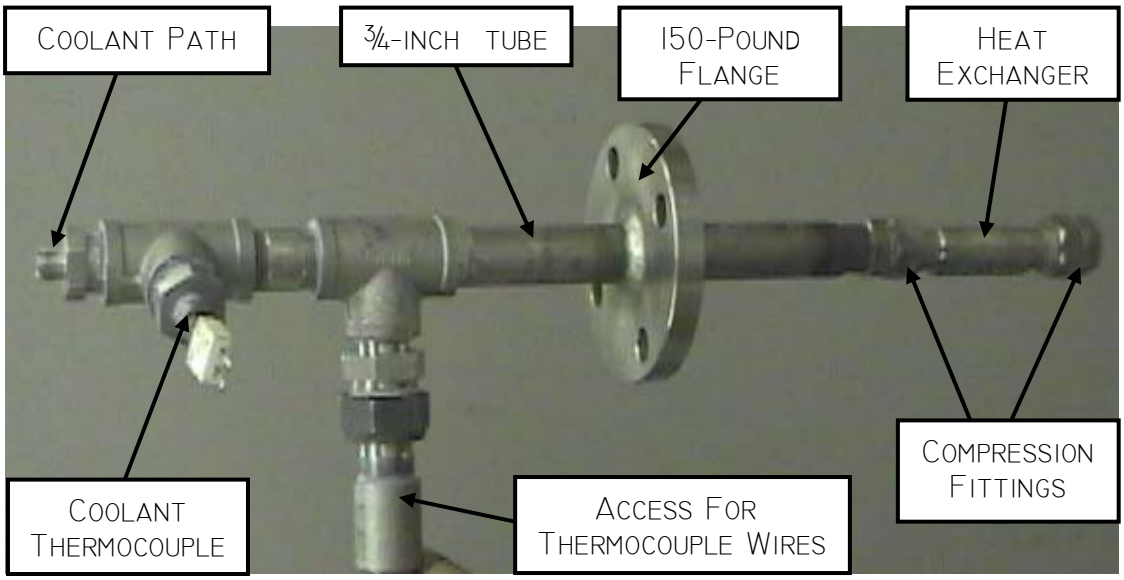

Figure 5-10: Heat exchanger supporting system

The compressed air supply, also used at the inlet of the burner rig, is connected to the Tee through a pressure regulator, a filter and a 2-25 SCFM (standard cubic foot per minute) range direct-reading spring-loaded flow meter. A 1/8-inch diameter type K thermocouple is located immediately upstream from the Tee and measures the temperature of the inlet coolant.

The remaining port of the Tee brings the thermocouple wires to a pressurized compartment through a 3-foot (0.9 m) long flexible stainless steel hose. In order to access the thermocouple wires from the atmospheric pressure side of the compartment wall, a thermocouple feed-through is used. Pressure feed-throughs allow to penetrate a pressure barrier with electrical conductors while maintaining a tight pressure seal. The wires and the body of the feed-through are a pre-assembled hermetic unit manufactured by Douglas engineering Company upon the customer's specifications. In the present case, the body is molded from a high temperature strength epoxy resin in a ¾-inch NPT connection with a total of 16 pairs of type K wires.

The pressurized compartment was built in order to provide a large enough space to inter-connect the thermocouple wires from the heat exchanger and from the pressure feed-through. The compartment sketched in Figure 5-11 and photographed in Figure 5-12 was made by welding a flange and a pipe end cap to either extremity of a 3 inch diameter and 4 inch long stainless steel pipe. The pressure feed-through NPT connection is screwed onto the blind flange which seals the compartment and the stainless steel flexible hose is screwed into a ¾-inch NPT hole drilled through the wall of the 3 inch diameter pipe.

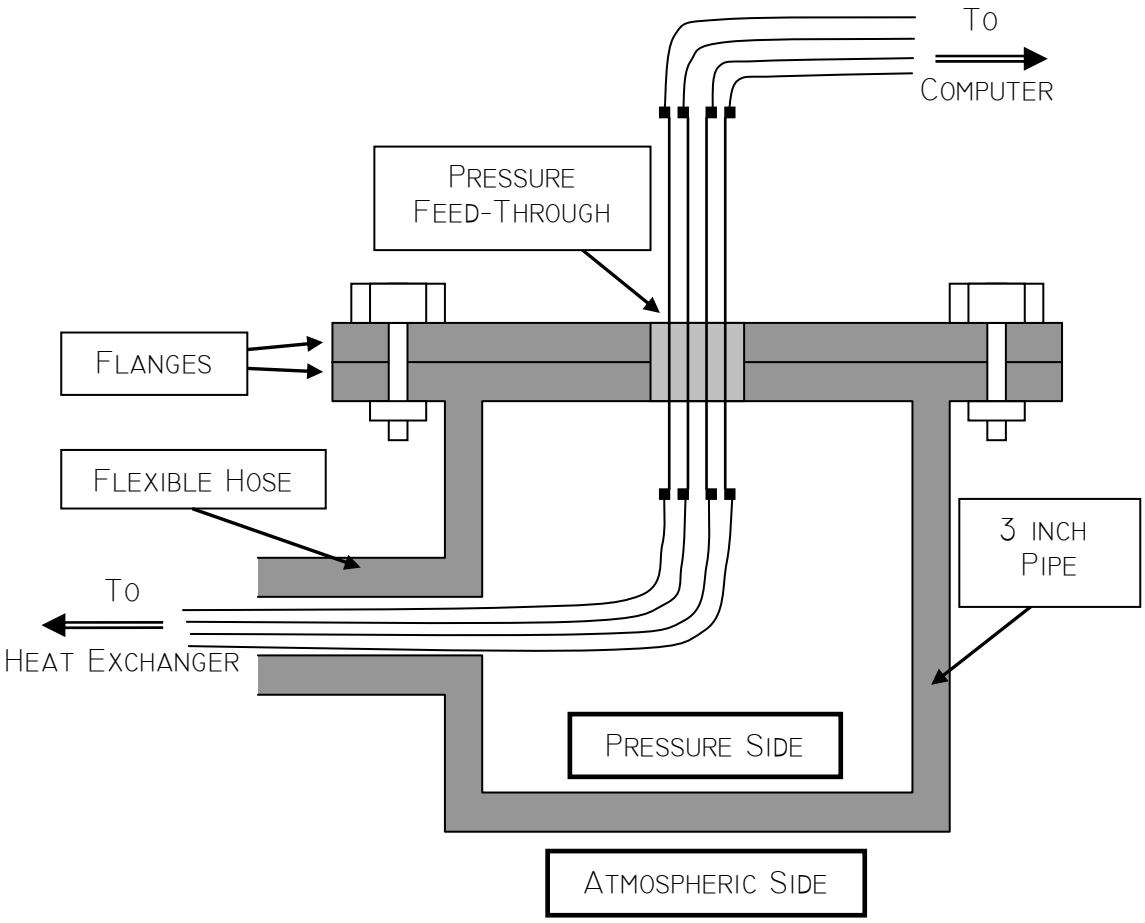

Figure 5-11: Sketch of the compartment for thermocouple connections

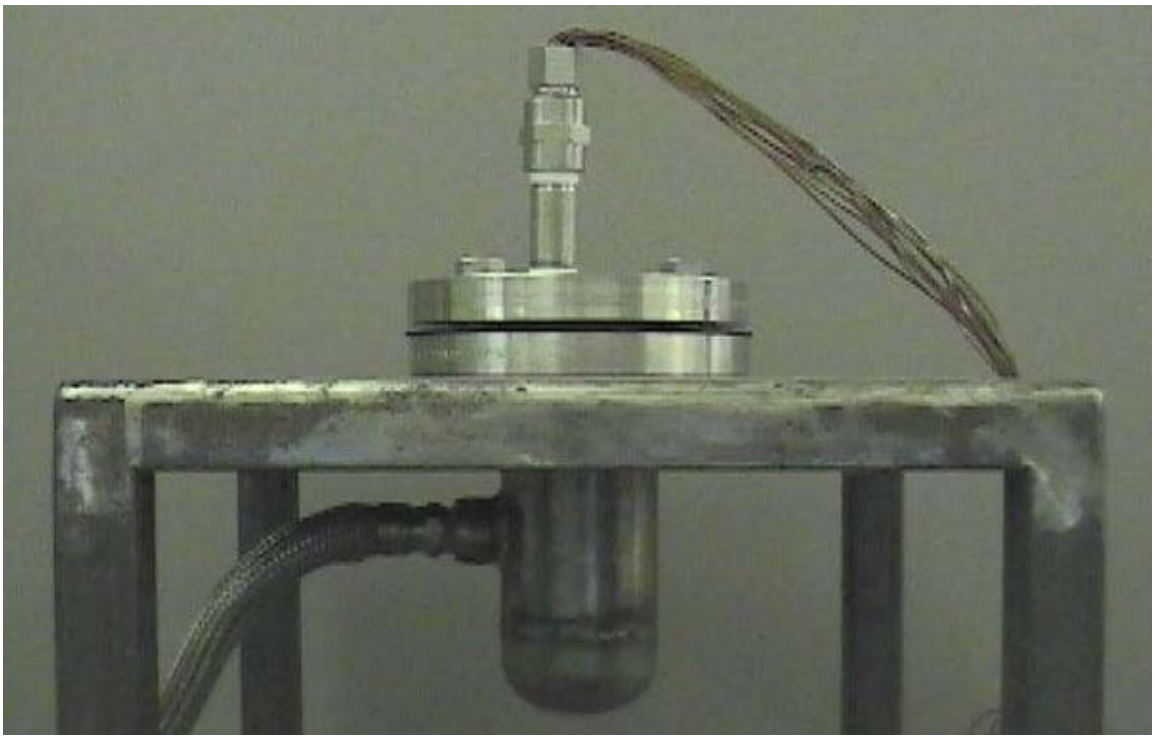

Figure 5-12: Compartment for thermocouple connections

Finally, eight of the sixteen pairs of thermocouple wires are utilized and connected to the data acquisition board of a computer.

The next section provides a description of the procedure followed in order to run the heat transfer experiments associated with the curved metal heat exchanger.

5.2 Experimental Procedure

Heat transfer experiments were performed on the curved metal heat exchanger in the aerodynamic facility using compressed air as coolant. For each mainstream gas temperature, specifically 200ºC, 300ºC and 400ºC, temperature measurements in the heat exchanger were conducted for coolant mass flow rates ranging from 1% to 4% of the mainstream gas mass flow rate.

The data acquisition system which uses the software InstruNet (from Omega Engineering) was calibrated using a thermocouple simulator (Model CL300 Portable Thermocouple source, Omega Engineering). The eight inputs of the data acquisition board were connected to the thermocouples measuring respectively the mainstream gas temperature, the temperatures of the nickel shroud at 0, 30, 60 and 90 degrees, the temperatures on the stainless steel tube at 15 and 100 degrees and the exit temperature of the coolant. A handheld digital thermometer was also used to monitor the temperature of the air coolant flowing into the heat exchanger.

Setting and maintaining the mainstream gas temperature and mass flow rate was achieved by adjusting the air pressure-regulating valve, the upstream control valve and the propane line pressure regulator. The temperature of the combustion gases was monitored using the thermocouple located in the test section and maintained within ±5%.

All the temperature data was recorded for each coolant mass flow rate until steady state was reached. The sequence in which the experiments were performed was such that the heat exchanger underwent increasing severe temperature conditions, in order to preserve the tested sample from eventual irreversible damage. This means that the experiments involving the lowest mainstream gas temperatures were completed first, and that for a given gas temperature, the coolant mass flow rates were tested in decreasing order. In addition, throughout all the experimental runs, the mass flow rate of compressed air feeding the combustor was held constant.

The temperature of the nickel shroud at -60 degrees was measured occasionally and recorded separately.

5.3 Data Reduction

Given mainstream gas temperature and coolant mass flow rate conditions correspond to a series of temperature, pressure and volumetric flow rate measurements recorded at steady state. The combination of those experimental conditions can be characterized by non-dimensional parameters defined in Equation 5-1 and Equation 5-2 as the coolant to mainstream gas temperature ratio *TR* and the coolant to mainstream gas mass flow rate ratio *MR*:

$$TR = \frac{T_C}{T_G}$$

Equation 5-1

$$MR = \frac{\dot{m}_C}{\dot{m}_G}$$

Equation 5-2

In Equation 5-1, T_C and T_G are respectively the temperatures of the air coolant and the mainstream gases in degrees Kelvin. In Equation 5-2, $\dot{m}_C$ and $\dot{m}_G$ are respectively the mass flow rate of air coolant and mainstream gases. The mass flow rate of combustion gases $\dot{m}_G$ is calculated using the law of conservation of mass applied to a control volume delimited by the combustor (Equation 5-3):

$$\dot{m}_G = \dot{m}_{Air} + \dot{m}_{\mathrm{Pr}opane}$$

Equation 5-3

If α denotes the ratio of $\dot{m}_{\mathrm{Pr}opane}$, the mass flow rate of propane and $\dot{m}_{Air}$, the mass flow rate of compressed air, Equation 5-3 can be rewritten as:

$$\dot{m}_G = (1+\alpha)\cdot \dot{m}_{Air}$$

Equation 5-4

It will be shown in Section 5.5 (Table 5-1 through Table 5-3) that α is much smaller than 1.0. Consequently $\dot{m}_G$ can be substituted with $\dot{m}_{Air}$. Rearranging Equation 5-2 by using the corresponding volumetric flow rates $\dot{V}_C$ and $\dot{V}_{Air}$ in SCFM (The standard conditions are 1 atmosphere and 70 degrees Fahrenheit) leads to Equation 5-5.

$$MR = \frac{\dot{V}_C}{\dot{V}_{Air}}$$

Equation 5-5

The value of $\dot{V}_C$ is obtained directly from the air coolant flow meter, whereas $\dot{V}_{Air}$ is calculated indirectly by combining the use of the pressure drop measurement across the orifice plate and the flow calibration chart associated with the meter run.

The experimental parameters can be reduced to a single pair of variables (*TR*, *MR*). The resulting temperature measurements are used to calculate the average cooling effectiveness of the curved heat exchanger as a function of (*TR*, *MR*).

In order to determine the average temperature of the Nickel shroud T_W, an arithmetic average of the temperatures T_0, T_{30}, T_{60} and T_{90} taken respectively at 0, 30, 60 and 90 degrees, is calculated.

$$T_w = \frac{T_0 + T_{30} + T_{60} + T_{90}}{4}$$

Equation 5-6

The value of T_W obtained with Equation 5-6 is inserted in Equation 1-1 and the cooling effectiveness $\varepsilon(TR, MR)$ can be determined.

5.4 Experimental Results and Uncertainty Analysis

5.4.1 Experimental Results

Raw data collected during the experiments is organized and provided in Table 5-1, Table 5-2 and Table 5-3. The tables respectively correspond to mainstream gas conditions of 200ºC, 300ºC and 400ºC. The quantities T_{SS15} and T_{SS100} refer to the temperatures of the stainless steel tube at 15 and 100 degrees from the leading edge whereas $T_{C\,out}$ refers to the exit temperature of the coolant.

Experimental data presented from Table 5-1 though Table 5-3 was reduced with the equations described in Section 5.3. The MathCAD calculation sheets are available in Appendix I. The reduced heat transfer results for the curved metal heat exchanger are summarized in Table 5-4.

Table 5-1: Curved metal heat exchanger experimental data for gases at 200ºC

$\dot{V}_C$ (scfm)	$\dot{V}_{Air}$ (scfm)	$\dot{m}_{Propane}$ (g/s)	T_0 (ºC)	T_{30} (ºC)	T_{60} (ºC)	T_{90} (ºC)	T_{SS15} (ºC)	T_{SS100} (ºC)	T_C (ºC)	$T_{C\,out}$ (ºC)	T_G (ºC)
4.0	362	0.5	70	78	82	76	63	82	26	83	205
7.0	362	0.5	54	62	65	58	48	64	24	67	209
10.7	362	0.5	46	53	56	48	39	53	23	56	210
14.5	362	0.5	39	47	49	41	34	45	23	48	204

Table 5-2: Curved metal heat exchanger experimental data for gases at 300ºC

$\dot{V}_C$ (scfm)	$\dot{V}_{Air}$ (scfm)	$\dot{m}_{Propane}$ (g/s)	T_0 (ºC)	T_{30} (ºC)	T_{60} (ºC)	T_{90} (ºC)	T_{SS15} (ºC)	T_{SS100} (ºC)	T_C (ºC)	$T_{C\,out}$ (ºC)	T_G (ºC)
4.0	360	0.8	96	104	110	105	85	110	26	111	298
7.0	360	0.8	75	82	87	81	64	86	25	90	303
10.7	360	0.8	61	69	72	66	52	69	24	74	306
14.5	358	0.8	53	61	64	56	44	59	24	65	307

Table 5-3: Curved metal heat exchanger experimental data for gases at 400ºC

$\dot{V}_C$ (scfm)	$\dot{V}_{Air}$ (scfm)	$\dot{m}_{Propane}$ (g/s)	T_0 (ºC)	T_{30} (ºC)	T_{60} (ºC)	T_{90} (ºC)	T_{SS15} (ºC)	T_{SS100} (ºC)	T_C (ºC)	$T_{C\,out}$ (ºC)	T_G (ºC)
4.0	357	1.1	128	137	145	141	114	146	28	150	392
7.0	357	1.1	93	101	107	102	78	106	26	112	407
11.0	355	1.1	75	83	88	81	61	84	25	91	408
14.5	357	1.1	65	73	77	69	52	72	25	78	406

Table 5-4: Curved metal heat exchanger results

TR	*error TR* (%)	*MR* (%)	*error MR* (%)	α (%)	T_W (ºC)	ε	*error* ε (%)
1.60	0.2	1	12.5	0.2	77	0.72	0.9
1.62	0.2	2	7.2	0.2	60	0.81	0.7
1.63	0.2	3	4.7	0.2	51	0.85	0.7
1.61	0.2	4	3.5	0.2	44	0.88	0.6
1.91	0.2	1	12.5	0.4	104	0.71	0.6
1.93	0.2	2	7.2	0.4	81	0.80	0.5
1.95	0.2	3	4.7	0.4	67	0.85	0.4
1.95	0.2	4	3.5	0.4	59	0.88	0.4
2.21	0.2	1	12.5	0.6	138	0.70	0.5
2.27	0.2	2	7.2	0.6	101	0.80	0.4
2.28	0.2	3	4.7	0.6	82	0.85	0.3
2.28	0.2	4	3.5	0.6	71	0.88	0.3

5.4.2 Uncertainty Analysis

In order to determine the uncertainty of the final experimental results, the Kline and McClintock method [18] described in Section 3.4.2 is used again. The measured experimental quantities T_C, T_G, T_0, T_{30}, T_{60}, T_{90}, $\dot{V}_C$ and $\dot{m}_{Air}$ are characterized by uncertainties related to the metering equipment and are summarized in Table 5-5. It is assumed that all other errors are negligible.

The Kline and McClintock method was used to determine the uncertainty in the determination of *TR*, *MR* and ε in each heat exchanger configuration and coolant flow rate setting. The results are indicated in Table 5-4 under the columns *error TR*, *error MR* and *error* ε.

Table 5-5: Absolute uncertainties on the measured quantities

Measurement	$\dot{V}_C$ (scfm)	$\dot{m}_{Air}$ (g/s)	T_C (ºC)	T_G, T_0, T_{30}, T_{60}, T_{90} (ºC)
Absolute (±)	0.5	0.7	0.1	2.0

5.5 Results and Discussion

Analysis of the data presented in Table 5-1 through Table 5-3, shows that both the temperature of the Nickel shroud and the temperature of the stainless steel tube vary as a function of the angular position from the leading edge of the heat exchanger.

For any *(MR,TR)* combination, the Nickel shroud temperature increases from the leading edge through the angular locations 30 and 60 degrees and decreases at 90 degrees. Even though locations at 0 and 30 degrees are submitted to the greatest heat flux from the mainstream gases, the corresponding temperatures are the lowest because these location benefit from impingement cooling. The continuous increase in temperature until the 60 degree angular location is due to the rise in temperature of the coolant. However, the Nickel shroud temperature declines at around 90 degrees because the external convective heat transfer coefficient associated with the flow of mainstream gases has decreased as a function of angular location and has become minimal (with a value 2 to 3 times lower than at the leading edge [28]).

All the temperature measurements made by the thermocouple situated at -60 degrees on the Nickel shroud are at most 5ºC less than the temperatures measured at 60 degrees. This indicates that the leading edge of the cylinder is not exactly at 0 degrees but

is slightly offset. This offset has very little impact on the cooling effectiveness calculations since it can only generate relative errors lower than 3%.

On the other hand, the temperature of the stainless steel tube increases with angular location, the reason being attributed to the rise in coolant temperature. For any *(MR,TR)* combination, the temperature measurement at 100 degrees is slightly lower than the exit temperature of the coolant. It is safe and reasonable to assume that the temperature of the stainless steel tube is equal to the temperature of the coolant and, of course, lower than the temperature of the Nickel shroud at any given angular location.

A plot of the cooling effectiveness versus *TR* and *MR* is provided in Figure 5-13 with the error bars. It appears that the cooling effectiveness of the curved micro pin fin heat exchanger ranges from 0.70 to 0.88 for the different combinations of flow settings used. The cooling effectiveness increases with coolant to mainstream gas mass ratio, which was a predictable trend.

Conversely, the effect of coolant to mainstream gas temperature ratio is very negligible, in particular as the coolant to mainstream gas mass ratio increases.

Importantly, it is noted that the inlet temperature of the coolant as measured by the thermocouple underestimates the actual temperature of coolant entering the micro pin fin heat exchanger. This situation is due to the fact that the coolant flow is heated in the portion of piping located between the thermocouple location and the entrance holes to the micro channel. This causes all the calculated values of cooling effectiveness to be underestimated. If the inlet temperature of the coolant were assumed to be equal to the temperature of the stainless steel tube at the angular location of 15 degrees, the successive values taken by the cooling effectiveness would be respectively 0.91, 0.93,

0.94 and 0.95 for the coolant to mainstream gas mass ratio values of 1%, 2%, 3% and 4%.

In order to properly compare the curved micro pin fin heat exchanger to other cooling schemes, it is important to include the order of magnitude of the Reynolds number of the mainstream gases. The next section presents a model predicting the value of the cooling effectiveness of the micro pin fin heat exchanger in the case of a typical gas turbine.

5.6 Cooling Effectiveness Prediction for a Typical Gas Turbine

For aircraft engines, the Reynolds number of the mainstream gases based on leading edge diameter of the turbine blades ranges typically from 75,000 to 300,000 [11] and corresponding values of cooling effectiveness vary from 0.3 to 0.7 [33]. In the present study, the Reynolds number based on the diameter of the Nickel shroud and the maximal velocity in the tests section ranges from 8,600 to 10,500 which is the maximal range attainable using the compressed air supply system.

In order to estimate the cooling effectiveness of the micro heat exchanger in real gas turbine flow conditions, a simple model has been created. The subscripts used herein are defined as follows:

- *external-rig*: corresponds to the flow properties on the outer surface of the Nickel micro heat exchanger for burner rig experimental conditions
- *internal-rig*: corresponds to the flow properties inside the Nickel micro heat exchanger for burner rig experimental conditions
- *external-turbine*: corresponds to the flow properties on the outer surface of the Nickel micro heat exchanger for real gas turbine experimental conditions

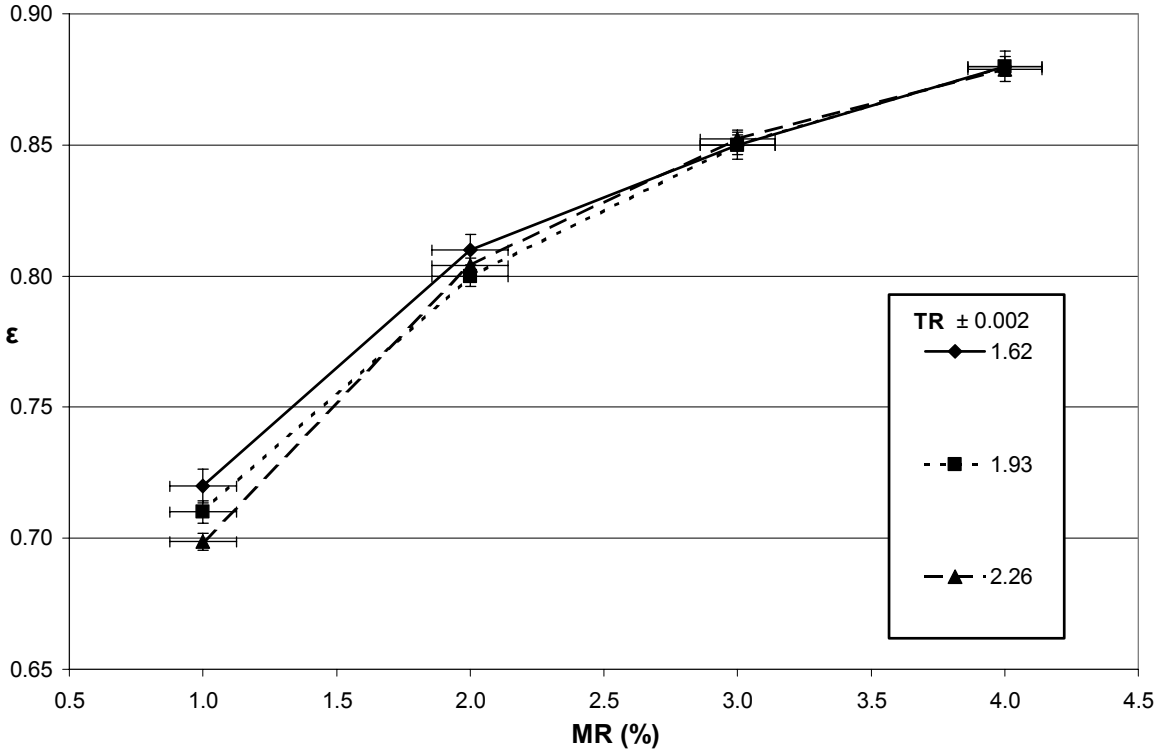

Figure 5-13: Cooling effectiveness as a function of *TR* and *MR*

- *internal-turbine*: corresponds to the flow properties inside the Nickel micro heat exchanger for real gas turbine experimental conditions

Using the schematic of thermal resistances for the turbine blade model in Chapter 3 (Figure 3-7), one can see that q'', the heat flux through the shroud of the heat exchanger, is equal to $h_{external-rig} \cdot (T_G - T_W)$ and $h_{\text{int}ernal-rig} \cdot (T_W - T_C)$.

According to the definition of the cooling effectiveness from Chapter 1 in the case of burner rig flow conditions, Equation 1-1 can be re-written as:

$$\varepsilon_{rig} = \frac{q''/h_{external-rig}}{q''/h_{external-rig} + q''/h_{\text{int}ernal-rig}}$$

Equation 5-7

A new relationship providing the cooling effectiveness ε_{rig} is obtained by dividing the numerator and denominator in Equation 5-7 by q'':

$$\varepsilon_{rig} = \frac{1/h_{external-rig}}{1/h_{external-rig} + 1/h_{\text{int}ernal-rig}}$$

Equation 5-8

According to Incropera & DeWitt [28], the Nusselt numbers of the flow at Reynolds numbers $Re_{external\text{-}turbine}$=300,000 and $Re_{external\text{-}rig}$=10,000 are respectively given by:

- $Nu_{external-turbine} = 0.027 \cdot \text{Re}^{0.805}_{external-turbine} \cdot \text{Pr}^{1/3}_{external-turbine}$
- and $Nu_{external-rig} = 0.193 \cdot \text{Re}^{0.618}_{external-rig} \cdot \text{Pr}^{1/3}_{external-rig}$

Therefore, the ratio r between the corresponding convective heat transfer coefficients is:

$$r = \frac{h_{external-turbine}}{h_{external-rig}} = \frac{(0.027 \cdot \mathrm{Re}^{0.805} \cdot \mathrm{Pr}^{1/3} \cdot k)_{external-turbine}}{(0.193 \cdot \mathrm{Re}^{0.618} \cdot \mathrm{Pr}^{1/3} \cdot k)_{external-rig}}$$

Equation 5-9

After substituting the values of Reynolds numbers *Re*, Prandtl numbers *Pr* and thermal conductivity *k* in Equation 5-9, the calculation of the ratio *r* yields a value of 37.4.

The ratio *p* between the convective heat transfer coefficients of the flow inside the micro channel in real gas turbine and burner rig experimental conditions is given in Equation 5-10. One can notice that Equation 5-10 is simpler than Equation 5-9. The reason is because $Re_{internal-turbine}=Re_{internal-rig}$, which leads to the same correlation for the Nusselt numbers in both experimental cases. The calculation of the ratio *p* yields a value of 2.4.

$$p = \frac{h_{\mathrm{int}\,ernal-turbine}}{h_{\mathrm{int}\,ernal-rig}} = \frac{(\mathrm{Pr}^{1/3} \cdot k)_{\mathrm{int}\,ernal-turbine}}{(\mathrm{Pr}^{1/3} \cdot k)_{\mathrm{int}\,ernal-rig}}$$

Equation 5-10

The cooling effectiveness of the micro pin fin heat exchanger equivalent to typical gas turbine conditions, $\varepsilon_{gas-turbine}$, can be estimated by Equation 5-11:

$$\varepsilon_{gas-turbine} = \frac{1/(h_{external-turbine})}{1/(h_{external-turbine}) + 1/h_{\mathrm{int}\,ernal-turbine}} = \frac{1/(r \cdot h_{external-rig})}{1/(r \cdot h_{external-rig}) + 1/(p \cdot h_{\mathrm{int}\,ernal-rig})}$$

Equation 5-11

Equation 5-8 can be re-arranged such that $h_{\mathrm{int}\,ernal-rig}$ is written as a function of $h_{external-rig}$ and ε_{rig}, leading to Equation 5-12:

$$\frac{1}{h_{\text{int}\,ernal-rig}} = \frac{1}{h_{external-rig}} \cdot \left(\frac{1}{\varepsilon_{rig}} - 1 \right)$$

Equation 5-12

Finally, $h_{\text{int}\,ernal-rig}$ from Equation 5-12 is substituted into Equation 5-11 and $h_{external-rig}$ cancels out, leading to a simple relationship giving $\varepsilon_{gas-turbine}$ as a function of ε_{rig}, r and p:

$$\varepsilon_{gas-turbine} = \frac{1}{1 + \frac{r}{p} \cdot \left(\frac{1}{\varepsilon_{rig}} - 1 \right)}$$

Equation 5-13

A plot of $\varepsilon_{gas-turbine}$ versus ε_{rig} is shown in Figure 5-14. The predicted cooling effectiveness values of the micro pin fin heat exchanger in the case of a gas turbine range from 0.13 to 0.32 which are rather low values compared to typical cooling schemes. If the inlet temperature of the coolant were based on the temperature of the stainless steel tube at the angular location of 15 degrees, the cooling effectiveness values would be significantly greater, ranging from 0.39 to 0.55.

It is reminded that the results derived above do not provide accurate values of cooling effectiveness but a prediction and that the pin fin array configuration of the curved heat exchanger has not been optimized to yield the best cooling effectiveness.

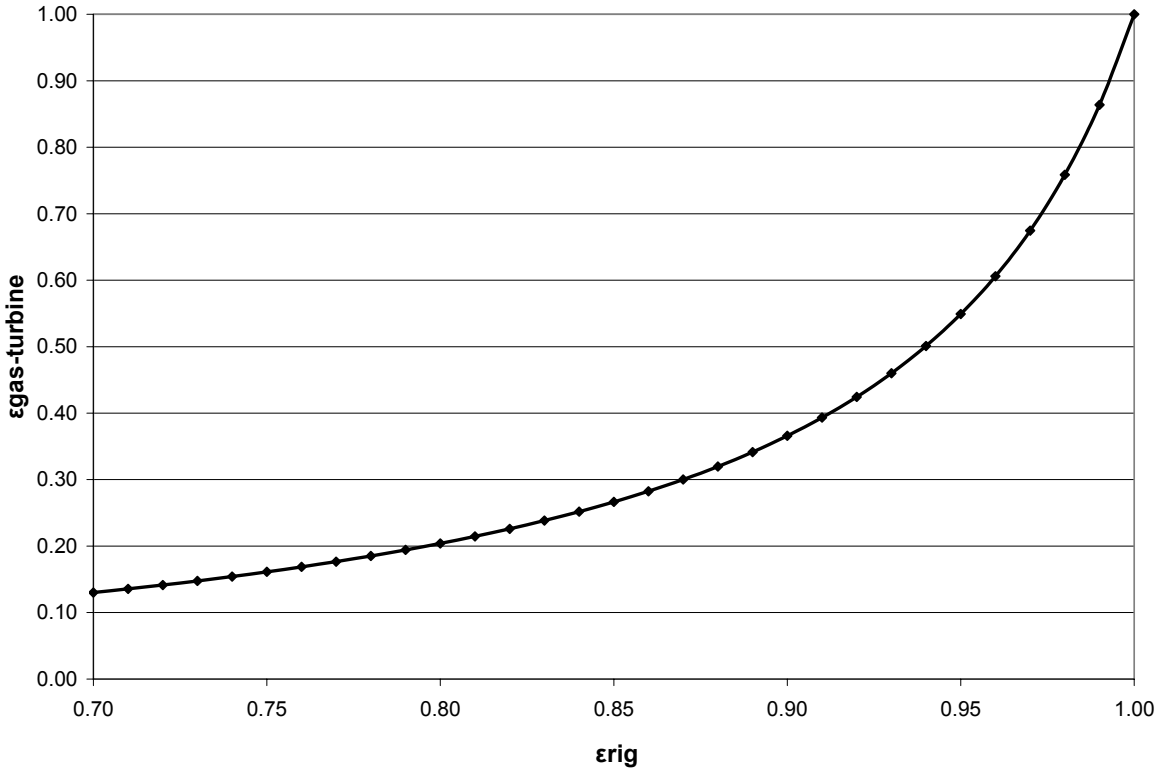

Figure 5-14: Cooling effectiveness in the case of a gas turbine as a function of the cooling effectiveness calculated in the burner rig.

CHAPTER 6 : CONCLUSIONS AND UPCOMING RESEARCH GOALS

This dissertation has successfully completed the following goals:

- Micro heat exchangers, both flat and of cylindrical configurations, were manufactured according to pre-established design specifications.
- An apparatus was fabricated to quantify the performance of micro pin fin array heat exchangers. Nusselt numbers and friction factors values over a range of Reynolds numbers from 4,500 to 19,500 were obtained. These values compare favorably with the results of Chyu [7],[8]. The suggested correlation for the Nusselt number is given below:

$$Nu = 0.014 \cdot \mathrm{Re}^{0.977} \cdot \mathrm{Pr}^{0.4} \qquad 4{,}500 \le \mathrm{Re} \le 19{,}200$$

- Tests were performed to determine the cooling effectiveness of a micro pin fin heat exchanger fabricated on a cylinder. Cooling effectiveness values ranging from 0.70 to 0.88 were obtained for coolant to mainstream gas mass flow rate ratios ranging from 1% to 4% and for coolant to mainstream gas temperature ratios from 1.62 to 2.26 at Reynolds number near 10,000.

Future work that should be completed is as follows:

- Optimize the pin fin array geometry to maximize the overall thermal performance.
- Perform experiments to accurately calculate cooling effectiveness values at Reynolds numbers approaching those typical within a gas turbine ($75{,}000 \le \mathrm{Re} \le 300{,}000$).

REFERENCES

[1] Artwork Conversion Software, Inc., "ASM 2500^{TM} DXF to Pattern Generator User's Manual", Version 5.0, June 1992.

[2] S.C. Arora, W. Abdel-Messeh, "Characteristics of Partial Length Circular Pin Fins As Heat Transfer Augmentors for Airfoil Internal Cooling Passages", Journal of Turbomachinery, July 1990, Vol. 112, pp.559-565.

[3] D., Baudrand, "Nickel Sulfamate Plating, Its Mystique And Practicality", Metal Finishing 94 (7), pp.15-18.

[4] E. W. Becker, W. Ehrfeld, P. Hagmann, A. Maner and D. Munchmeyer, "Fabrication of microstructures with high aspect ratios and great structural heights by synchrotron radiation lithography, galvanoforming and plastic moulding (LIGA process)", Microelectronic Engineering 4, p 35-56, 1986.

[5] P. Bley, W. Menz, W. Bacher, K. Feit, M. Harmening, H. Hein, J. Mohr, W. Schomburg and W. Stark, "Application of the LIGA Process in Fabrication of Three-dimensional Mechanical Microstructures", In S. Namba & T. Tsurushima (Ed.), Microprocess 91, 1991 International Microprocess Conference, p 384-389, Kanazawa, Japan, 1991.

[6] B.A. Brigham, "The Effect of Channel Convergence on Heat Transfer in a Passage With Short Pin Fins", NASA-TM-83201, 1984.

[7] M.K. Chyu, "Heat Transfer and Pressure Drop for Short Pin-Fin Arrays with Pin-Endwall Fillet", Journal of Heat Transfer, 1990, Vol. 112, pp. 926-932.

[8] M.K. Chyu, Y.C. Hsing, T.I-P. Shih, V. Natarajan, "Heat Transfer Contributions of Pins and Endwall in Pin-Fin Arrays: Effects of Thermal Boundary Condition Modeling", Journal of Turbomachinery, April 1999, Vol. 121, pp. 257-263.

[9] M.K. Chyu, C.H. Yen, W. Ma, T. I-P. Shih, "Effects of Flow Gap Atop Pin Elements on The Heat Transfer from Pin Fin Arrays", Presented at the International Gas Turbine & Aeroengine Congress & Exhibition, Indianapolis, June 7-10, 1999.

[10] J.C. Coynel, "Study of a Micro Heat Exchanger for Turbine Blades", M.S. Thesis, Louisiana State University, Baton Rouge, December 1999.

[11] Discussions with Dr. Srinath Ekkad, Assistant Professor, Mechanical Engineering Department, Louisiana State University, Baton Rouge, Louisiana.

[12] J.R. Dobbs, J.A. Graves, S. Meshkov, "Advanced Airfoil Fabrication", Proceedings of the 8th International Symposium on Superalloys, Pennsylvania, Sept 22-26 1996, pp. 523-529.

[13] J.R. Dobbs, J.A. Graves, R.R. Bowman, "Advanced Airfoil Fabrication", Proceedings of the Annual HITEMP Review, Oct 23-25, Ohio, 1995, Vol II, paper 30, pp. 1-13.

[14] V. Galhotra, C. Marques, Y. Desta, K. Kelly, M. Despa, A. Pendse, J. Collier, "Fabrication of Mold Inserts Using a Modified LIGA procedure", SPIE Proceedings, Micromachining and Microfabrication Process Technology II, Vol. 2879, p 168-173, September 1996.

[15] P. Hagmann, W. Ehrfeld and H. Vollmer, "Fabrication of microstructures with extreme structural heights by reaction injection molding", Makromolekulare Chemie- Macromolecular Symposia 24, p 241-251, 1989.

[16] J.C. Han, S. Dutta, S. Ekkad, "Gas Turbine Heat Transfer & Cooling Technology", Taylor and Francis, 2001, ISBN 156032841X.

[17] D.K. Hennecke, "Turbine Blade Cooling in Aero Engines- Some New Results, Future Trends and Research Requirements", pp. 1-16.

[18] J.P. Holman, "Experimental Methods For Engineers", 3rd edition, McGraw-Hill Inc., ISBN 0-07-029601-4, 1978, pp.41-50.

[19] http://www.aadc.com/lamilloy.htm and interview of Larry Junod, Director of Aerodynamics And Cooling Systems, Allison Advanced Development Company, Indianapolis.

[20] http://www.hitecorp.com

[21] http://www.lsiphotomask.com

[22] http://www.matweb.com

[23] http://www.mezzosystems.com

[24] http://www.microchem.com

[25] http://www.poco.com

[26] http://www.pumachemical.com

[27] J.-J. Hwang, D.-Y. Lai, Y.-P. Tsia, "Heat Transfer and Pressure Drop in Pin-Fin Trapezoidal Ducts", Journal of Turbomachinery, April 1999, Vol. 121, pp.264-271.

[28] F. P. Incropera and D. P. DeWitt, "Introduction to Heat Transfer", 3rd Edition, John Wiley & Sons, New York, 1996, ISBN 0-471-30458-1.

[29] L. Jian, Y. M. Desta, G. Aigeldinger, M. Bednarzik, B. Loechel, J. Goettert, "SU-8 Based Deep X-ray Lithography/LIGA", SPIE Proceedings, Micromachining and Microfabrication Process Technology VIII, Vol. 4979, p 394-401, January 2003.

[30] B.V. Karlekar and R. M. Desmond, "Engineering Heat Transfer", West Publishing Company, 1977, ISBN 0-8299-0054-3.

[31] W.M. Kays, M.E. Crawford, "Convective Heat and Mass transfer", 3rd Edition, McGraw Hill, ISBN 0070337217,1993, pp. 344.

[32] K. Kelly, C. Marques, J. Rogers, M. Despa, J. Collier, "High-aspect-ratio microstructure-covered sheets: fabrication and function" ", SPIE Proceedings, Smart Structures and Materials 1998: Smart Electronics and MEMS, October 14-15 Austin TX, Vol. 3328, p 403-408, July 1998.

[33] B. Lakshminarayana, "Fluid Dynamics and Heat Transfer of Turbomachinery", John Wiley & Sons, Inc., 1996, ISBN 0-471-85546-4, pp.677.

[34] S.C. Lau, J.C. Han, Y.S. Kim, "Turbulent Heat Transfer and Friction in Pin Fin Channels With Lateral Flow Ejection", Journal of Heat Transfer, Feb 1989, Vol. 111, pp. 51-58.

[35] F. Lowenheim, "Modern Electroplating", 3rd Edition, John Wiley & Sons, p 287-296, 1974, ISBN 0-471-54968-1.

[36] A. Maner, S. Harsch and W. Ehrfeld, "Mass Production of Microdevices with Extreme Aspect Ratios by Electroforming", Plating and Surface Finishing, p 60-65, March 1988.

[37] C. Marques, "Heat Transfer of a Microstructure-Covered Cylinder in Crossflow", M.S. Thesis, Louisiana State University, Baton Rouge, August 1997.

[38] C. Marques, Y. Desta, J. Rogers, M. Murphy and K. Kelly, "Fabrication of High-Aspect-Ratio Microstructures on Planar and Non-Planar Surfaces Using a Modified LIGA Process", Journal of MEMS, Dec 1997, pp. 329-336.

[39] D.E. Metzger, C.S. Fan, S.W. Haley, “Effects of Pin Shape and Array Orientation on Heat Transfer and Pressure Loss in Pin Fin Arrays”, Journal of Engineering for Gas Turbines and Power, Jan 1984, Vol. 106, pp. 252-257.

[40] D.E. Metzger, R.A. Berry, J.P. Bronson, “Developing Heat Transfer in Rectangular Ducts With Staggered Arrays of Short Pin Fins”, Journal of Heat Transfer, Nov 1982, Vol. 104, pp. 700-706.

[41] R.J. Moffat, “Turbine Blade Cooling”, Presented at Symposium on Heat Transfer in Rotating Machinery, Apr 28- May 3, 1985, Hawai.

[42] D.A. Olson, “Heat Transfer in Thin, Compact Heat Exchangers With Circular, Rectangular, or Pin-Fin Flow Passages”, Journal of Heat Transfer, May 1992, Vol. 114, pp. 373-382.

[43] J.R. Shen, Z. Wang, P.T. Ireland, T.V. Jones, A.R. Byerley, “Heat Transfer Enhancement Within a Turbine Blade Cooling Passage Using Ribs and Combinations of Ribs With Film Cooling Holes”, Journal of Turbomachinery, Vol. 118, July 1996, pp. 428-434.

[44] S. Thakur, J. Wright, W. Shyy, “Convective Film Cooling Over a Representative Turbine Blade Leading-Edge”, International Journal of Heat and Mass Transfer, 1999, Vol. 42, pp. 2269-2285.

[45] Y.S. Touloukian, R.W. Powell, C.Y. Ho, P.G. Klemens, “Thermophysical Properties Of Matter, Volume 1, Thermal Conductivity: Metallic Elements and Alloys”, IFI/Plenum, New York-Washington, 1970.

[46] G.J. VanFossen, “Heat Transfer Coefficients for Staggered Arrays of Short Pin Fins”, Journal of Engineering for Power, Vol. 104, 1982, pp. 268-274.

[47] H. Wang, S.H. Jason Lo, “Effect of Heat Treatment on the Thermal Conductivity of a Particulate SiC Reinforced 6061 Aluminum Matrix Composite”, Thermal Conductivity 23, edited by K.E. Wilkes, R.B. Dinwiddie and R.S. Graves, pp288-298, Technomic Publishing Co., Lancaster, PA, 1996.

[48] G. White, J. Gabriel, K-C. Chin, Y-C. Tan, “Aero Thermodynamic Facility Senior Design Project Report”, Advised by Dr. S. Ekkad and Dr. S. Acharya, Louisiana State University, College Of Engineering, Department Of Mechanical Engineering, Fall 1999.

[49] A. Zhukauskas “Heat Transfer from Tubes in Cross Flow”, Advances in Heat transfer, Vol. 8, pp.116-133, 1972.

NOMENCLATURE FOR APPENDIXES

A2	Cross sectional area of the flow at the upstream pressure tap
A3	Cross sectional area of the flow at the downstream pressure tap
AChyu	Reference area used by Chyu to define the convective heat transfer coefficient [8]
Aheat	Reference area used to define the convective heat transfer coefficient
Cp(T)	Specific heat of the coolant as a function of temperature
CrossAreaFlow	Maximal cross sectional area of the flow in the heat exchanger
Dh	Hydraulic diameter ($4Ac/P$)
Distancetopbot	Distance between the higher and lower temperature locations in the heating block
distanceAl	Distance between Tbot and the interface with heat exchanger
distanceNi	Thickness of the top plate of the Nickel heat exchanger
distanceSS	Thickness of the top plate of the Stainless steel heat exchanger
Dpost	Diameter of the pin fins
f	Friction factor of the heat exchanger
fINCRO	Friction factor of the heat exchanger as correlated by Incropera & DeWitt [28]
heffective	Effective convective heat transfer coefficient corresponding to the micro pin fin heat exchanger
Height	Height of the channel inside the heat exchanger
Height2	Height of the channel upstream from the heat exchanger
Height3	Height of the channel downstream from the heat exchanger
hexternal	Convective heat transfer coefficient at the shroud outer surface of the curved heat exchanger
hUHF	Convective heat transfer coefficient for uniform heat flux boundary conditions
i	Counter used for vector computations
j	Counter used for vector computations
k(T)	Thermal conductivity of the coolant as a function of temperature
kAl	Thermal conductivity of Aluminum
kNi	Thermal conductivity of Nickel
ksilicone	Thermal conductivity of the thermally conductive silicone paste
kSS	Thermal conductivity of Stainless steel
Length	Streamwise dimension of the heat exchanger
M2	Mach number of the coolant at the upstream pressure tap location
M3	Mach number of the coolant at the downstream pressure tap location
massflowrate	Mass flow rate of coolant
massflowrategase	Mass flow rate of the mainstream hot gases
MR	Coolant to mainstream gas mass flow rate ratio

Npost	Total amount of pin fins in the heat exchanger
Nu	Nusselt number of the coolant
NuChyu	Nusselt number of the coolant as correlated by Chyu [8]
NuINCRO	Nusselt number of the coolant as correlated by Incropera & DeWitt [28]
Num	Number of data points
NumberIntervals	Amount of intervals used to subdivide the path of the coolant in the streamwise dimension of the heat exchanger
NuUHF	Nusselt number of the coolant for uniform heat flux boundary conditions
P1	Gage pressure of the coolant in the entry reservoir
P2	Gage pressure of the coolant in the upstream pressure tap location
P3	Gage pressure of the coolant in the downstream pressure tap location
P4	Gage pressure of the coolant in the exit reservoir
Pb	Bulk pressure of the coolant inside the heat exchanger
Po	Standard pressure
Pr(T)	Prandtl number of the coolant as a function of temperature
Q	Rate of heat transferred to the coolant
Qconduction	Rate of heat conducted to the top plate of the heat exchanger
Qconvection	Rate of heat transferred to the coolant by convection
Qelectric	Electric power dissipated in the cartridge heaters measured with the wattmeter
QperLength	Rate of heat transferred to the coolant per unit length
R	Ideal gas constant of the air coolant
Re	Reynolds number of the coolant
Rthermal	Summation of all the thermal resistances in series
scfm	Volumetric flow rate
Spanwiseratio	Pin spacing to diameter ratio in the spanwise direction
T1	Temperature of the coolant in the entry reservoir
T2	Temperature of the coolant at the upstream pressure tap location
T3	Temperature of the coolant at the downstream pressure tap location
T3total	Total temperature of the coolant at the downstream pressure tap location
T4	Temperature of the coolant in the exit reservoir
TapToTapLength	Distance between the pressure tap locations
Tb	Bulk temperature of the coolant in the heat exchanger
Tbconv	Bulk temperature of the coolant (without units)
Tblinear	Bulk temperature of the coolant calculated with the liear temperature
Tbot	Temperature measured in the lower elevation of the heating block
Tbstatic	Bulk temperature of the coolant calculated with the static temperature
Tbtotal	Bulk temperature of the coolant calculated with the total temperature
Tc	Temperature of the coolant at the inlet of the curved heat exchanger
tcontact	Thickness of thermally conductive silicone paste applied
Tcoolantxk	Temperature of the coolant at the distance xk from the coolant injection location in the curved heat exchanger
Tconversion	Factor used to remove units from temperatures (K^{-1})

Tdynamic	Dynamic temperature of the coolant at a given streamwise location
Tf	Film temperature of the coolant in the heat exchanger
Tfconv	Film temperature of the coolant (without units)
Tg	Temperature of the hot mainstream gases
Tlinear	Linearized temperature profile of the static temperature of the coolant
To	Standard temperature
TR	Coolant to mainstream gas temperature rate ratio
TRaveraged	Average matrix of TR
Tshroudxk	Temperature of the shroud at the distance xk from the coolant injection location in the curved heat exchanger
Tstatic	Static temperature of the coolant at a given streamwise location
Ttop	Temperature measured in the higher elevation of the heating block
Ttotal	Total temperature of the coolant at a given streamwise location
Tw	Average temperature at the flat heat exchanger-coolant interface or average shroud temperature of the curved heat exchanger
U	Average overall heat transfer coefficient of the curved heat exchanger
V2	Velocity of the coolant at the upstream pressure tap location
V3	Velocity of the coolant at the downstream pressure tap location
Vb	Bulk velocity of the coolant in the heat exchanger
volumetricrateco.	Volumetric flow rate of coolant in the curved heat exchanger
volumetricratega.	Volumetric flow rate of hot mainstream gases
Width	Width of the channel
xk	Distance from the coolant injection location in the curved heat exchanger
ΔKE	Kinetic energy change of the coolant per unit length in a given interval
ΔP23	Differential pressure of the coolant measured between the pressure tap locations
ΔPHE	Pressure drop of the coolant across the heat exchanger
ΔTIE	Static temperature change of the coolant in a given interval
ΔTKE	Dynamic temperature change of the coolant in a given interval
ε	Average cooling effectiveness of the curved heat exchanger
εxk	Cooling effectiveness at the distance xk from the coolant injection location in the curved heat exchanger
μ(T)	Dynamic viscosity of the coolant as a function of temperature
ρb	Bulk density of the coolant in the heat exchanger
ρo	Standard density

APPENDIX A: X-RAY MASK AUTOCAD DRAWINGS

The 500 μm disks have been approximated by overlapping 98 μm x 490 μm rectangles rotated 8 times with respect to their center. The following AutoCAD drawings show respectively:

- the overall view of the staggered hole pattern
- a detail view of a 500 μm disk.

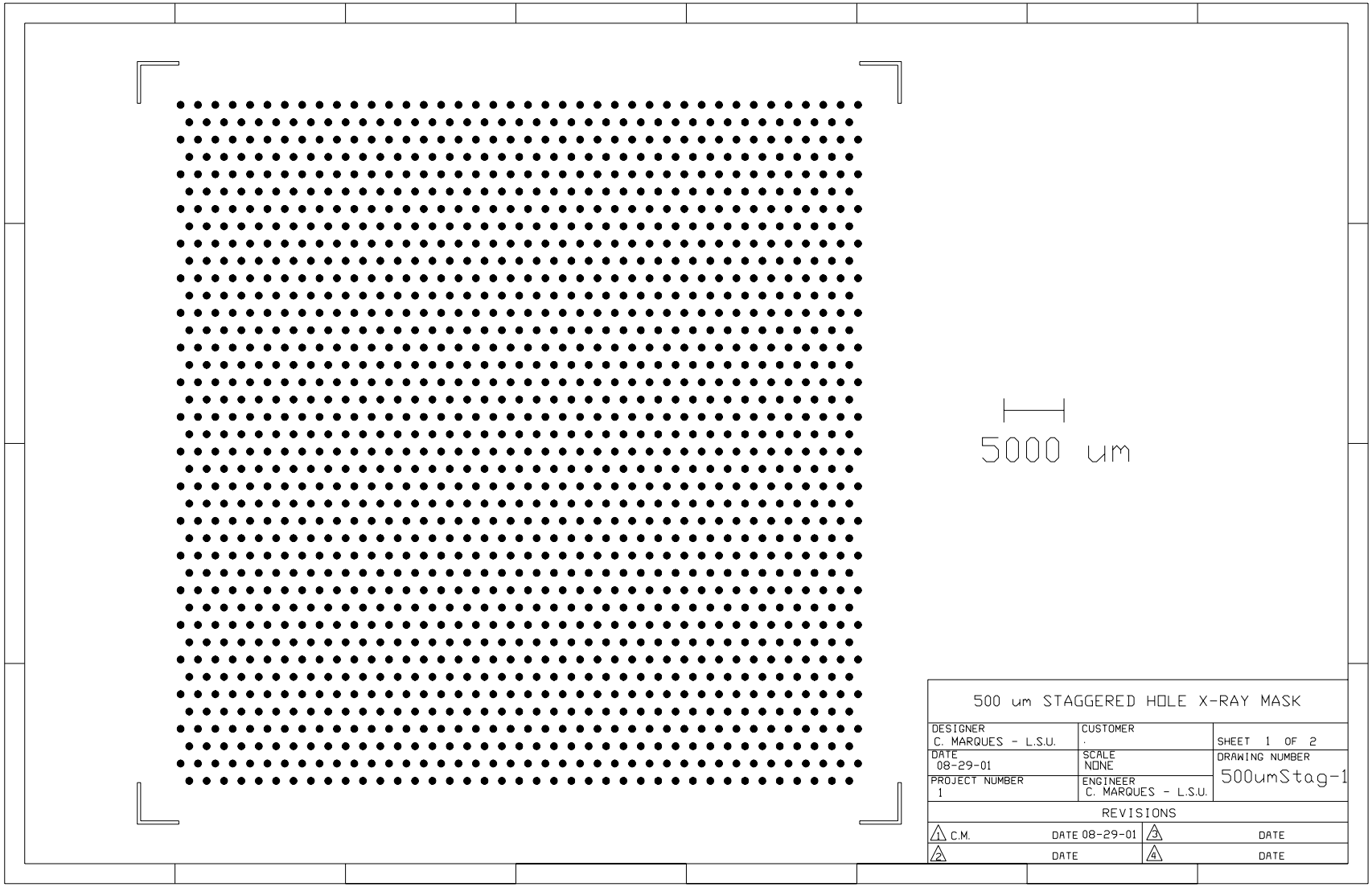
5000 um
500 um STAGGERED HOLE X-RAY MASK
DESIGNER
C. MARQUES - L.S.U.
CUSTOMER
.
SHEET 1 OF 2
DATE
08-29-01
SCALE
NONE
DRAWING NUMBER
500umStag-1
PROJECT NUMBER
1
ENGINEER
C. MARQUES - L.S.U.
REVISIONS
1 C.M. DATE 08-29-01
3 DATE
2 DATE
4 DATE

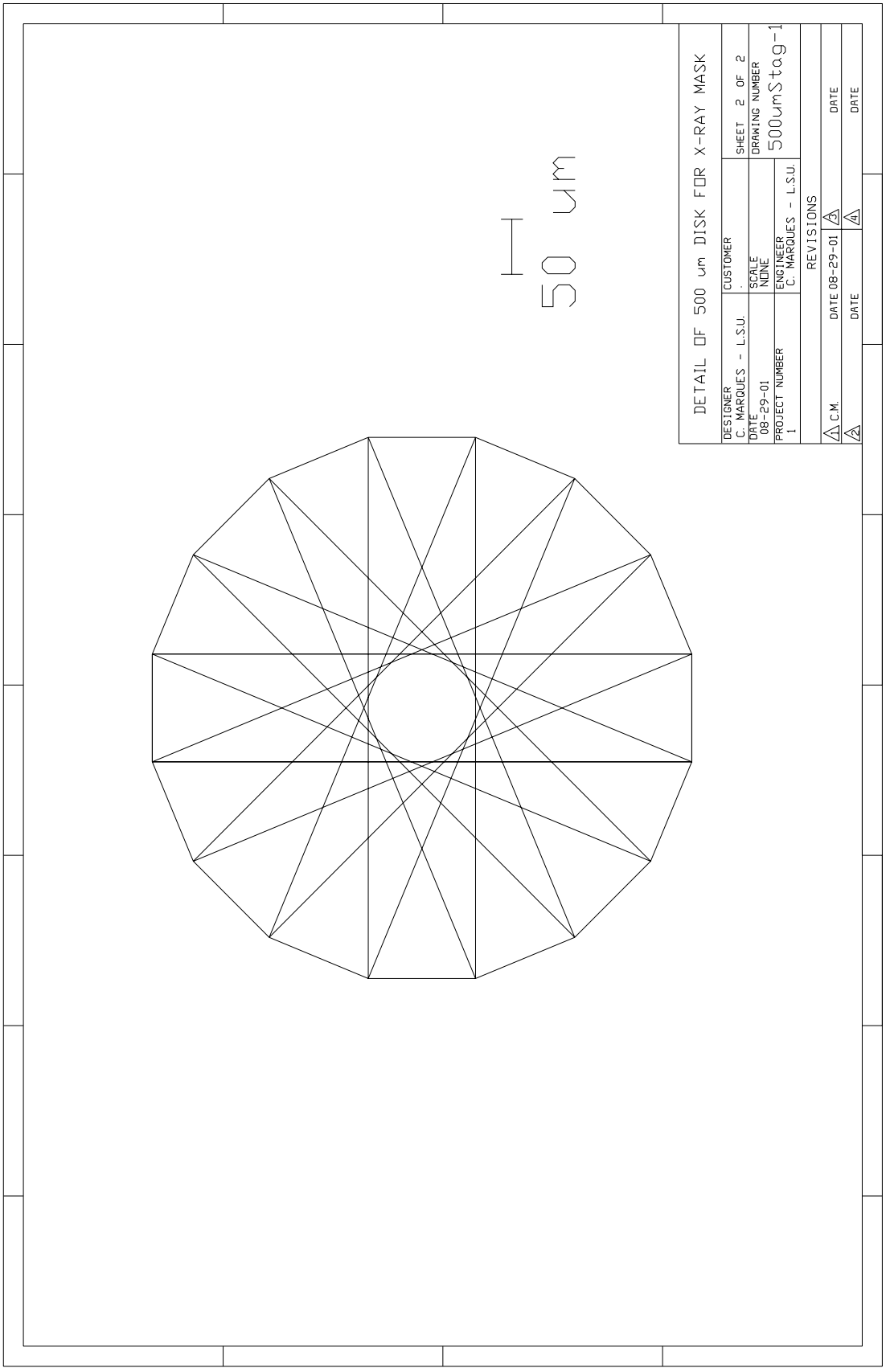
DETAIL OF 500 um DISK FOR X-RAY MASK
DESIGNER
C. MARQUES - L.S.U.
DATE
08-29-01
PROJECT NUMBER
1
CUSTOMER
.
SCALE
NONE
ENGINEER
C. MARQUES - L.S.U.
SHEET 2 OF 2
DRAWING NUMBER
500umStag-1
REVISIONS
1 C.M. DATE 08-29-01
2 DATE
3 DATE
4 DATE
50 um

APPENDIX B: THE ELECTROPLATING SUBSTRATE HOLDER

The three parts composing the substrate holders are, the lower half, the upper half and the face gasket. As shown in Figure B- 1, the lower half is a 1.5 x 7 x 6 inch body made of polyetherimide (natural PEI ®Ultem) and machined with a 4.75 inch diameter recess. A stainless steel plate is screwed onto the bottom of the recess and connected to a 1/8 inch diameter threaded stainless steel rod which extends to the outside. The threaded rod is surrounded by a PVC tube attached to the PEI block with a sealed NPT thread.

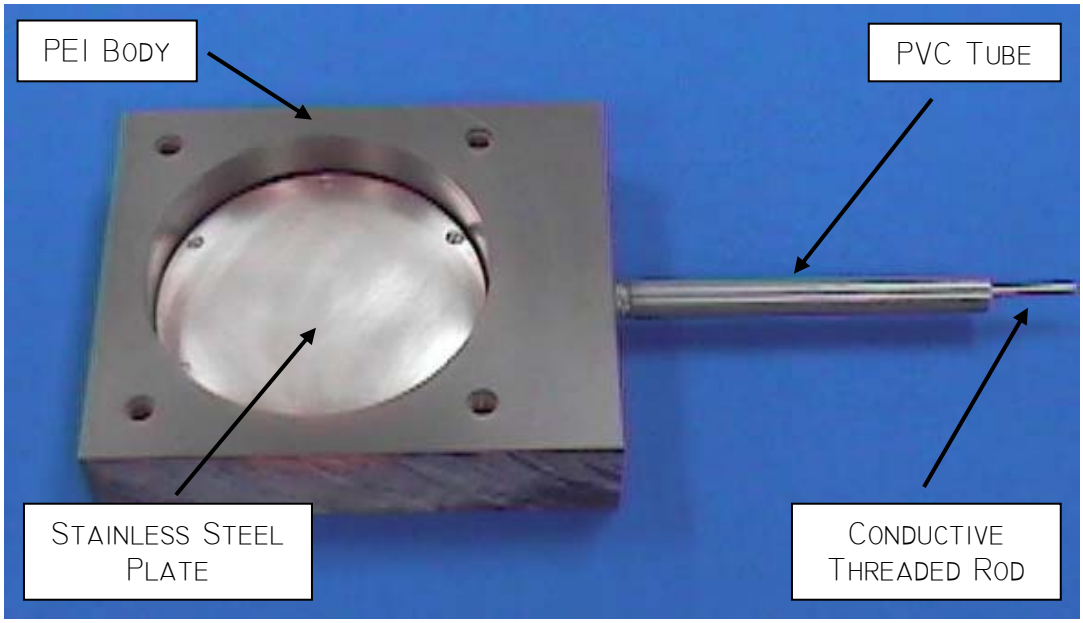

Figure B- 1: Lower half of the substrate holder

Figure B- 2 depicts the upper half of the holder and the face gasket. The shape of the upper half is complementary to the lower half so that one can fit into the other. To prevent leakage, two gaskets are applied to the protruding part of the upper half. One is imbedded into the outer surface and the other is placed onto the top face. Figure B- 3 shows the sample holder mounted around a stainless steel electroplating substrate. The maximal substrate thickness is 12 mm. The maximal area available for electroplating is the one corresponding to a diameter of 3.5 inch.

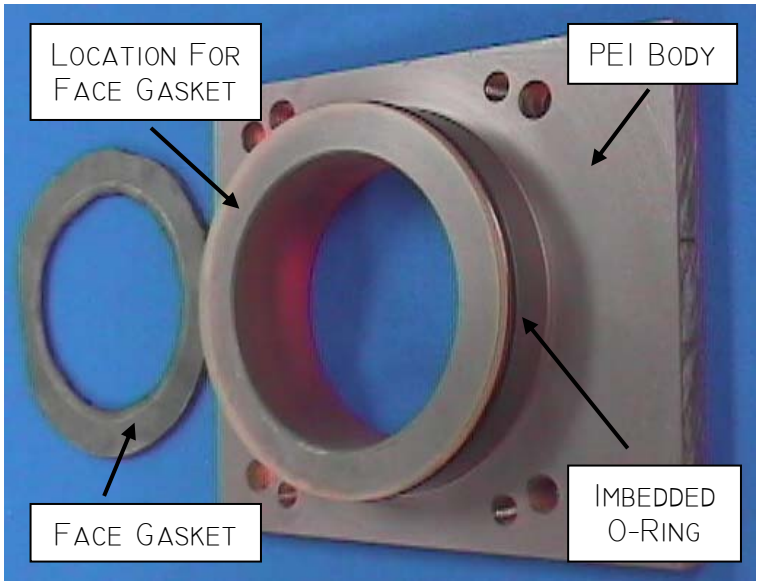

Figure B- 2: Upper half of the substrate holder and face gasket

The jig shown on Figure B- 4 was manufactured to connect a vacuum pump to the recess located in the sample holder. It consists of a Plexiglas plate into which an O-ring has been imbedded and a connector fitting. During operation, the vacuum jig is

positioned such that the O-ring is in contact with the upper half of the substrate holder and the vacuum pump is connected to the fitting.

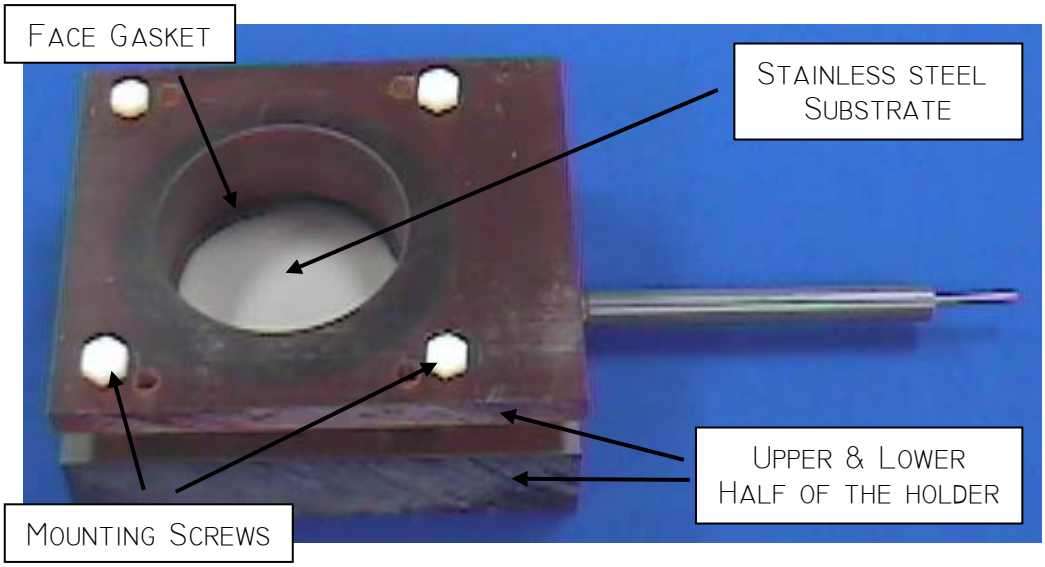

Figure B- 3: Assembled substrate holder

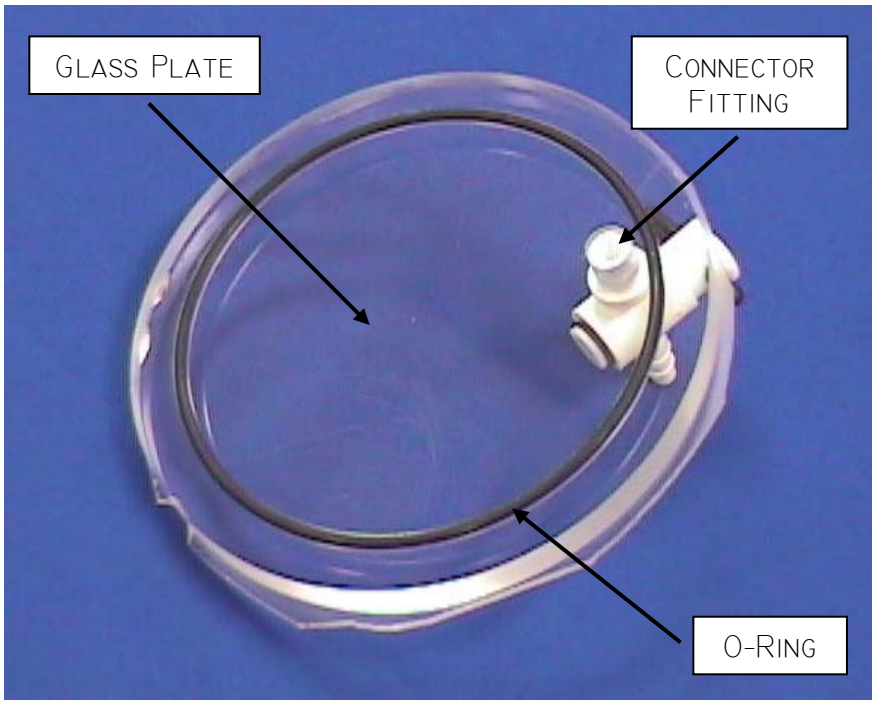

Figure B- 4: Vacuum jig for the substrate holder.

APPENDIX C: DRAWINGS OF THE FLAT HEAT EXCHANGER EXPERIMENTAL APPARATUS

The following pages show in order the AutoCAD drawings of:

- The upper half of the apparatus
- The lower half of the apparatus
- The details of the heat exchanger

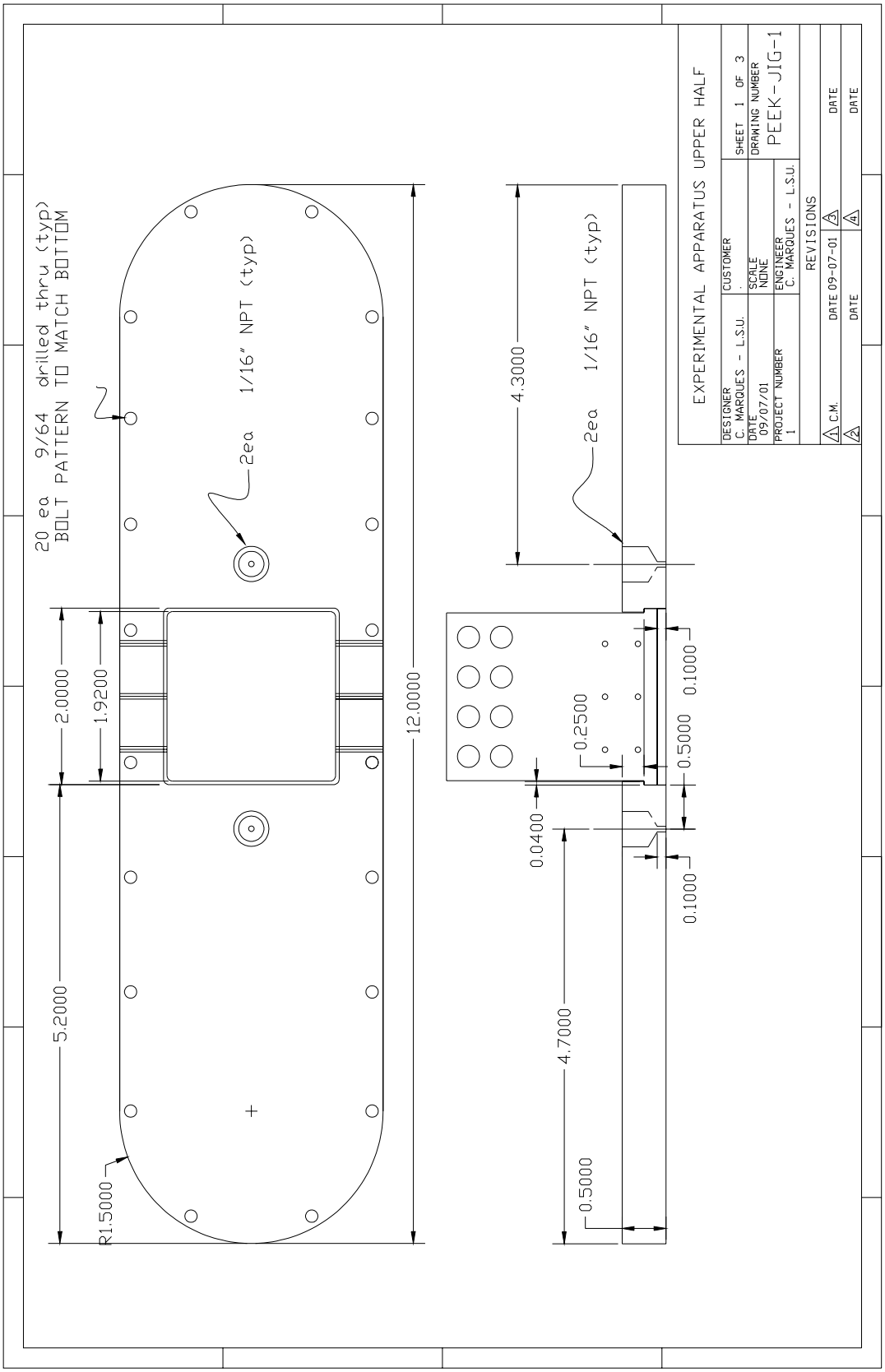
EXPERIMENTAL APPARATUS UPPER HALF
DESIGNER
C. MARQUES - L.S.U.
CUSTOMER
.
SHEET 1 OF 3
DATE
09/07/01
SCALE
NONE
DRAWING NUMBER
PEEK-JIG-1
PROJECT NUMBER
1
ENGINEER
C. MARQUES - L.S.U.
REVISIONS
C.M.
DATE 09-07-01
DATE
DATE
DATE
20 ea 9/64 drilled thru (typ)
BOLT PATTERN TO MATCH BOTTOM
2ea 1/16" NPT (typ)
2.0000
1.9200
5.2000
12.0000
R1.5000
4.3000
2ea 1/16" NPT (typ)
0.2500
0.1000
0.5000
0.0400
0.1000
4.7000
0.5000

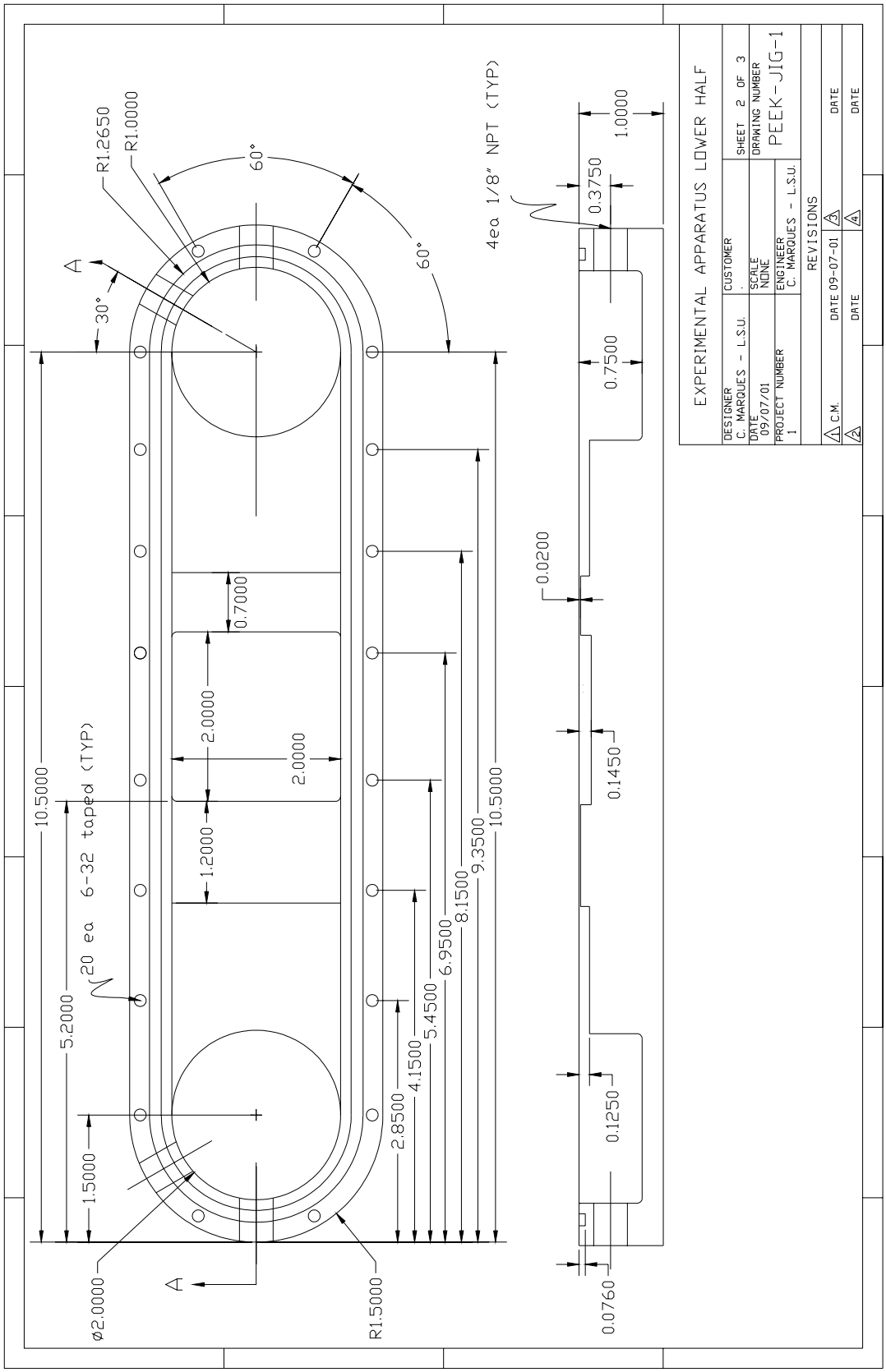
EXPERIMENTAL APPARATUS LOWER HALF
DESIGNER
C. MARQUES - L.S.U.
CUSTOMER
SHEET 2 OF 3
DATE
09/07/01
SCALE
NONE
DRAWING NUMBER
PEEK-JIG-1
PROJECT NUMBER
1
ENGINEER
C. MARQUES - L.S.U.
REVISIONS
C.M.
DATE 09-07-01
DATE
DATE
DATE
R1.2650
R1.0000
60°
60°
30°
A
4eq 1/8" NPT (TYP)
0.3750
1.0000
0.7500
0.0200
0.1450
0.1250
0.0760
10.5000
5.2000
1.5000
20 eq 6-32 taped (TYP)
0.7000
2.0000
2.0000
1.2000
2.8500
4.1500
5.4500
6.9500
8.1500
9.3500
10.5000
ø2.0000
R1.5000
A

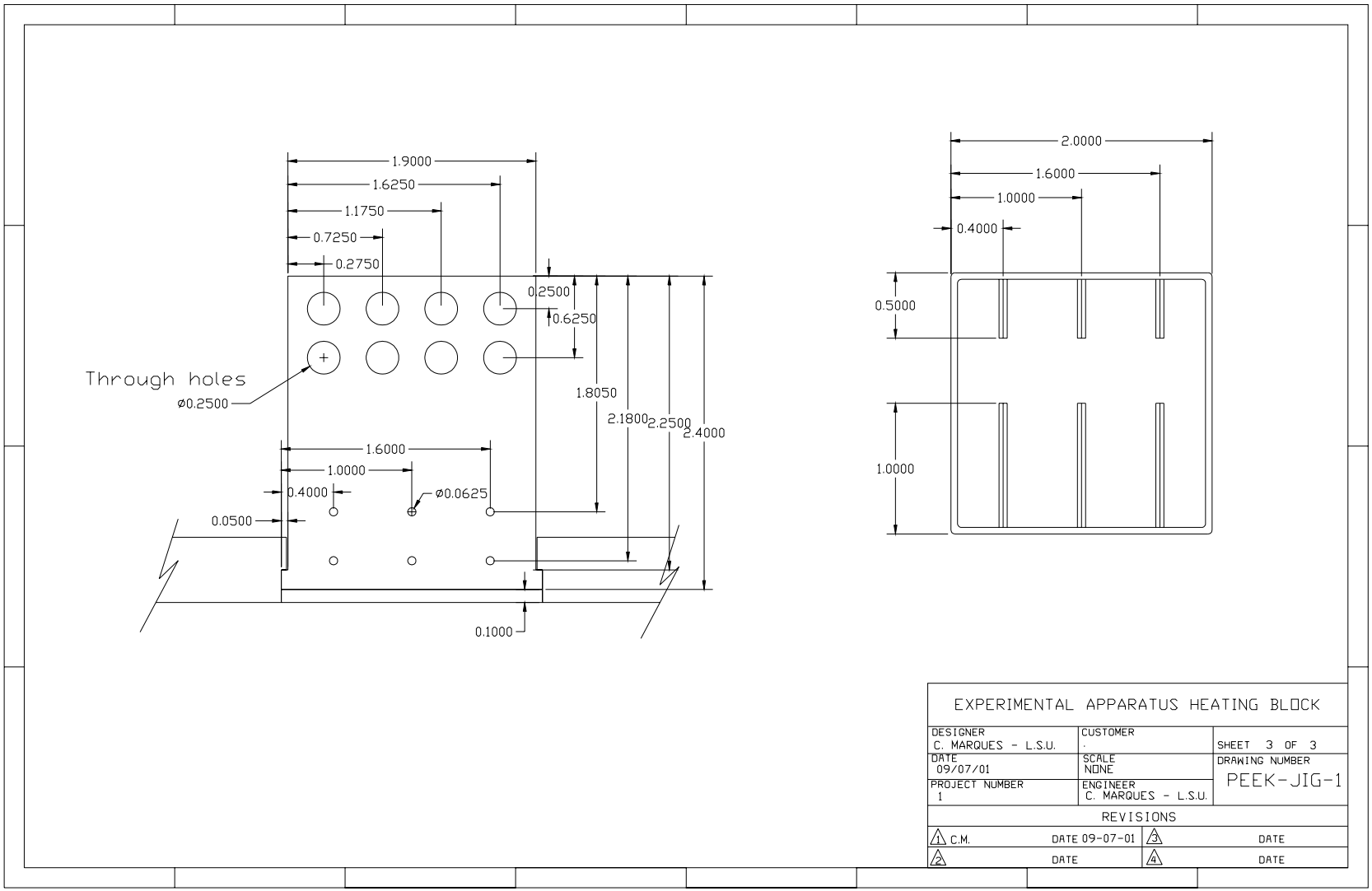
1.9000
1.6250
1.1750
0.7250
0.2750
0.2500
0.6250
Through holes
ø0.2500
1.8050
2.1800
2.2500
2.4000
1.6000
1.0000
0.4000
ø0.0625
0.0500
0.1000
2.0000
1.6000
1.0000
0.4000
0.5000
1.0000
EXPERIMENTAL APPARATUS HEATING BLOCK
DESIGNER
C. MARQUES - L.S.U.
CUSTOMER
.
SHEET 3 OF 3
DATE
09/07/01
SCALE
NONE
DRAWING NUMBER
PEEK-JIG-1
PROJECT NUMBER
1
ENGINEER
C. MARQUES - L.S.U.
REVISIONS
1 C.M. DATE 09-07-01
2 DATE
3 DATE
4 DATE

APPENDIX D: FINITE ELEMENT MODEL

A three dimensional finite element model including the heating block used in the flat heat exchanger apparatus and the surrounding material was created with the software ANSYS 5.7. The model was used in order to predict the maximal heat leakage rate from the heating block into the surrounding PEEK and the insulation, which occurs in the testing of the parallel plate heat exchanger without posts. In addition, the 3-D finite element model allowed to verify the validity of the 1-D model used in Section 3.3.2.2 in order to estimate the average temperature of the coolant-heat exchanger interface.

D.1 Description of the Model

The geometry of the apparatus being symmetric with respect to a vertical mid-plane in the streamwise direction of the flow, the model includes only half of the structure, as shown in Figure D-1 and Figure D-2. The thermal conductivities and dimensions of the material involved, namely PEEK, Calsil, Aluminum and Stainless Steel are as given in Section 3.1.2. The values of convective heat transfer coefficients are calculated from correlations provided by Incropera and DeWitt [28] in the case of turbulent, fully developed flow in tubes.

ANSYS 5.7 modelizes the geometry of the problem as small elements characterized by constant properties. The problem solved for is the steady state heat equation described as:

$$\frac{\partial^2 T}{\partial x^2} + \frac{\partial^2 T}{\partial y^2} + \frac{\partial^2 T}{\partial z^2} = 0$$

Equation D- 1

The following subsections describe the types of boundary conditions used in the model.

D.1.1 Convective Boundary Condition

Equation D- 2 mathematically describes this condition which is specified by the value of the convection heat transfer coefficient h, and the average surrounding fluid temperature T_{fluid}. In Equation D- 2, x_n is a coordinate corresponding to a vector normal to the interface.

$$-k\left.\frac{\partial^2 T}{\partial x_n^{\,2}}\right|_{surface} = h(T_{fluid} - T_{surface})$$

Equation D- 2

This type of boundary condition is present at the interface between the apparatus and the surrounding atmospheric air (T_{fluid}= To) as well as at the interface between the 500 μm channel and the compressed air coolant (T_{fluid}= Tb). In the model, the increase of Tb throughout the micro channel is approximated by 3 average coolant temperatures. Each average coolant temperature characterizes one of the 3 regions (namely the upstream micro channel, the heat exchanger micro channel and the downstream micro channel) which arbitrarily subdivide the micro channel.

D.1.2 Constant Heat Flux Boundary Condition

This condition is specified by the value of the heat flux q'' corresponding to the 100 Watts dissipated by the cartridge heaters. In the model, the heat flux is applied to the top of the aluminum heating block.

$$-k\left.\frac{\partial^2 T}{\partial x_n^{\,2}}\right|_{surface} = q''$$

Equation D- 3

D.1.3 Adiabatic Boundary Condition

This condition which is described by Equation D- 4 is applied to all the remaining boundaries of the model. Those boundaries correspond to the symmetry planes of the experimental apparatus.

$$-k\left.\frac{\partial^2 T}{\partial x_n^{\,2}}\right|_{surface} = 0$$

Equation D- 4

The boundary conditions in the case of the parallel plate heat exchanger without pin fins at the lowest coolant mass flow rate are indicated on the geometry of the model in Figure D-1 and Figure D-2. The convective heat transfer coefficient corresponding to each coolant Reynolds number in the micro channel are shown in Table D-1.

D.2 Estimation of Heat Losses

Heat losses into the PEEK and the insulation materials are maximal when the heat transfer resistance between the heating block and the coolant is the lowest, which occurs when the parallel heat exchanger is tested at the lowest coolant flow rate (*Re*=4,000).

In order to estimate heat losses, the model presented in this Appendix was solved for both highest and lowest mass flow rates of coolant. Temperature contours are shown in Figure D-3 and Figure D-4. The heat flux going through the coolant-stainless steel interface was integrated over the surface of the interface and allowed to calculate the heat losses.

The results for heat losses are summarized in Table D-1 and range from 5.5 to 10.5 %.

D.3 Verification of the 1-D Thermal Resistance Model in the Heating Block

According to the 1-D thermal resistance model presented in Section 3.3.2.2, the temperature drop between the horizontal plane at elevation (1) in the heating block and the parallel plate heat exchanger-coolant interface ΔT_{1-D} is given as:

$$\Delta T_{1-D} = \frac{Q}{A_{heat}} \cdot \left(\frac{l_{Al}}{k_{Al}} + \frac{l_{SS}}{k_{SS}} \right)$$

Therefore, using the dimensions and the material properties of stainless steel and aluminum, ΔT_{1-D} =7.84ºC.

For both lowest and highest coolant mass flow rates, the average temperature of the parallel plate heat exchanger-coolant interface (T_{ave}) , the temperature at elevation (1) in the heating block (T_{bot}) and the difference between the temperatures (ΔT_{ANSYS}) were estimated using the ANSYS. According to the results, which are summarized in Table D-2, the 1-D thermal resistance model approximates the 3-D ANSYS model with an accuracy ranging from 0.9 to 3.0%.

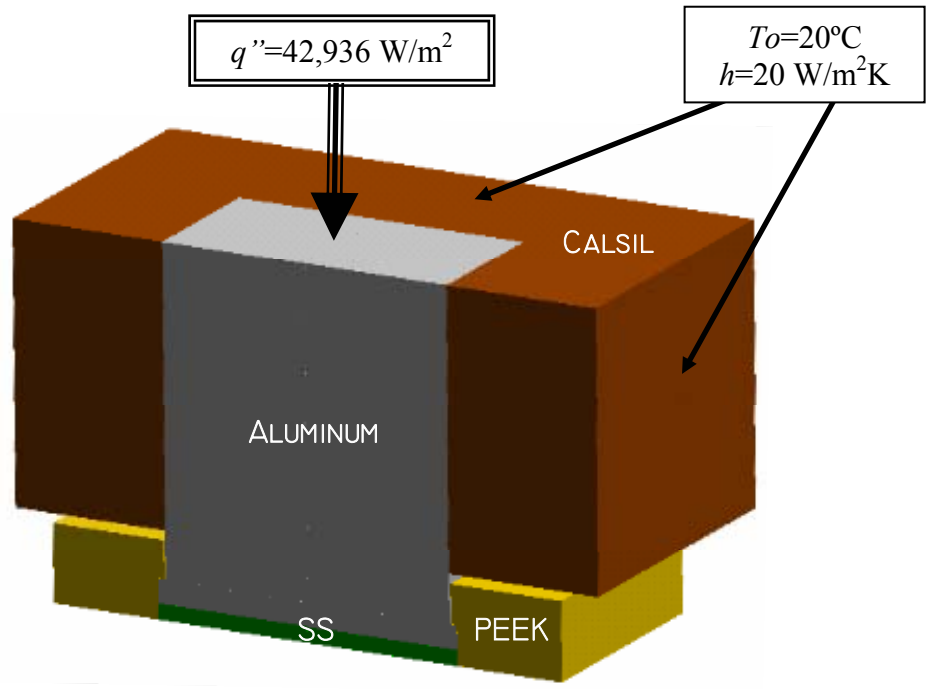

Figure D-1: Front view of the 3-D ANSYS model geometry

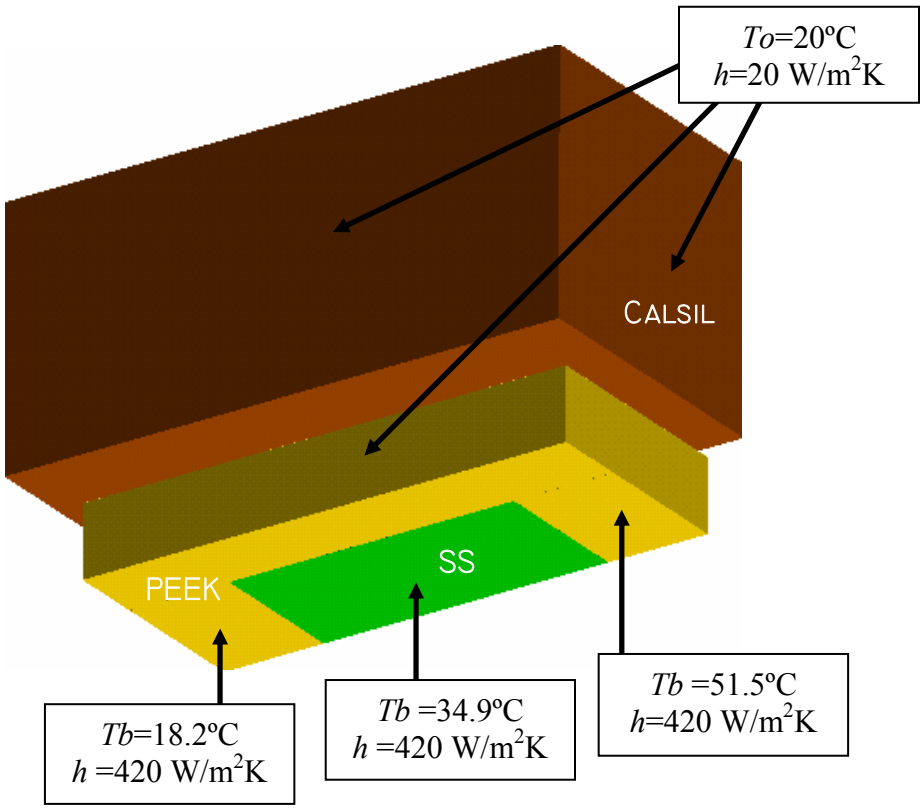

Figure D-2: Rear view of the 3-D ANSYS model geometry

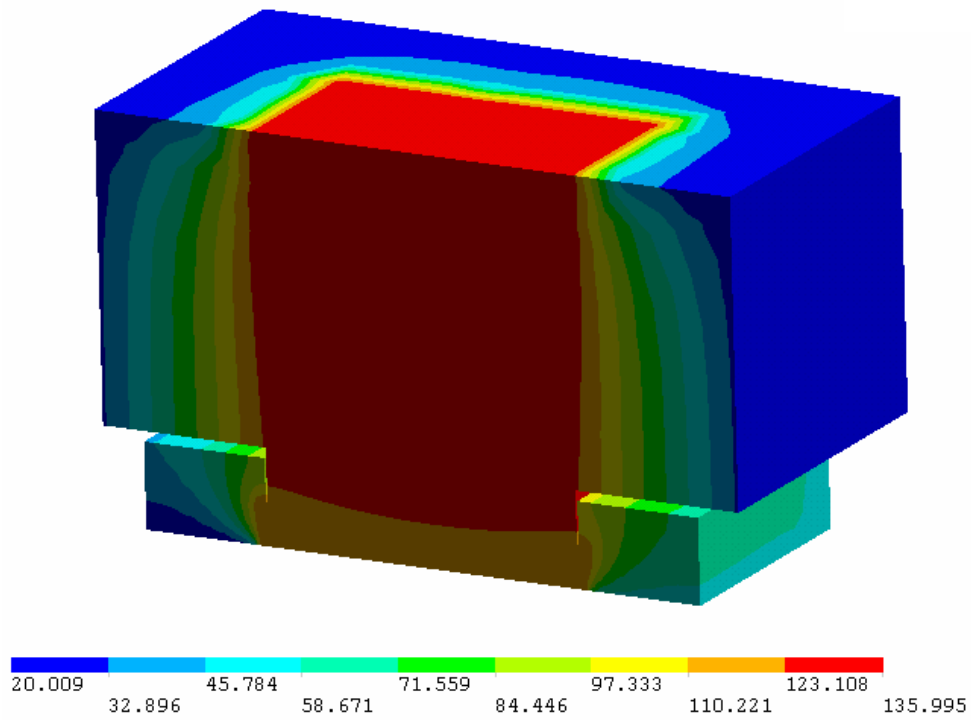

Figure D-3: Temperature contours at *Re*=4,000

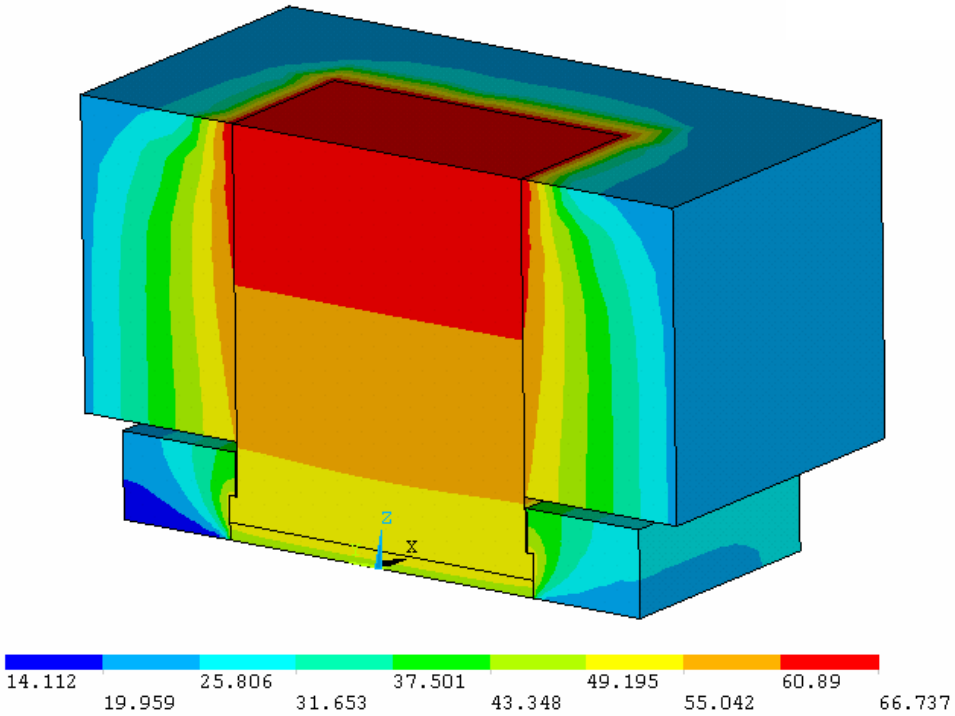

Figure D-4: Temperature contours at *Re*=20,000

Table D-1: Heat losses at the extreme coolant mass flow rates in the case of the parallel plate heat exchanger

Re	h (W/m^2K)	T_b (ºC)	Heat leakage rate (%)
4,000	420	18.2 / 34.9 / 51.5	10.5
20,000	1265	13.9 / 17.5 / 21.1	5.5

Table D-2: Comparison between 1-D model and ANSYS model at the extreme coolant mass flow rates in the case of the parallel plate heat exchanger

Re	T_{ave} (ºC)	T_{bot} (ºC)	ΔT_{1-D} (ºC)	ΔT_{ANSYS} (ºC)	Model accuracy (%)
4,000	115.96	123.57	7.84	7.61	3.0
20,000	46.14	54.05	7.84	7.91	0.9

APPENDIX E: MATHCAD MODEL FOR ESTIMATING Tb

Experimental Data :

Note: maximum flow rate data from Pin Fin Heat Transfer Experiments

$scfm := 16 \frac{ft^3}{min}$ $T2 := (273.2 + 19.1)\ K$ $Qelectric := 100\ W$

$P2 := (14.7 + 65)\ psi$ $\Delta P23 := 46.3\ psi$

Properties and constants:

$NumberIntervals := 10$

$R := 287 \frac{J}{kg \cdot K}$

$Po := 1\ atm$

$To := 294.3\ K$

$Cp := 1000 \frac{J}{kg \cdot K}$

Geometric parameters:

$Length := 2.0\ in$

$Height := 0.5\ mm$

$Width := 2.0\ in$

Calculations:

mass flow rate:

$\rho o := \frac{Po}{R \cdot To}$

$massflowrate := scfm \cdot \rho o$ $massflowrate = 9.1 \cdot 10^{-3}\ kg \cdot s^{-1}$

P3, flow cross sectional area, energy per unit length:

$P3 := P2 - \Delta P23$

$CrossAreaFlow := Height \cdot Width$

$QperLength := \frac{Qelectric}{Length}$ $\quad QperLength = 19.7 \frac{W}{cm}$

P across the heat exchanger (assume that $\frac{dP}{dx} := constant \cdot \rho \cdot \frac{V^2}{2}$ ***and that ΔT is small):***

$i := 0 .. NumberIntervals$

$x_i := i \cdot \frac{Length}{NumberIntervals}$

$P_i := \left(\frac{P3^2 - P2^2}{Length} x_i + P2^2 \right)^{0.5}$

V across the heat exchanger (using $massflowrate := \rho \cdot V \cdot CrossAreaFlow$ ***):***

$V_i := \frac{massflowrate \cdot R \cdot T2}{CrossAreaFlow \cdot P_i}$

Kinetic energy term ΔKE per unit length in each interval:

$j := 1 .. NumberIntervals$

$\Delta KE_j := massflowrate \cdot \frac{(V_j)^2 - (V_{j-1})^2}{2 \cdot (x_j - x_{j-1})}$

Temperature change ΔTIE corresponding to internal energy increase in each interval:

$\Delta TIE_j := \frac{(QperLength - \Delta KE_j) \cdot (x_j - x_{j-1})}{massflowrate \cdot Cp}$

Temperature change ΔTKE equivalent to kinetic energy increase in each interval:

$\Delta TKE_j := \frac{\Delta KE_j \cdot (x_j - x_{j-1})}{massflowrate \cdot Cp}$

Overal static temperature change corresponding to internal energy increase:

$Sum\Delta Tstatic := \sum_j \Delta TIE_j$ $\quad Sum\Delta Tstatic = 4.08\ K$

Overal dynamic temperature change equivalent to kinetic energy increase:

$$\text{Sum}\Delta\text{Tdynamic} := \sum_{j} \Delta\text{TKE}_j \qquad \text{Sum}\Delta\text{Tdynamic} = 6.96\ \text{K}$$

Static temperature Tstatic as a function of dowstream location:

$$\text{Tstatic}_0 := \text{T2}$$

$$\text{Tstatic}_j := \text{Tstatic}_{j-1} + \Delta\text{TIE}_j$$

Dynamic temperature Tdynamic as a function of dowstream location:

$$\text{Tdynamic}_0 := 0\ \text{K}$$ (***Consider V2 as reference velocity)***

$$\text{Tdynamic}_j := \text{Tdynamic}_{j-1} + \Delta\text{TKE}_j$$

Total temperature Ttotal as a function of dowstream location:

$$\text{Ttotal}_0 := \text{Tstatic}_0 + \text{Tdynamic}_0$$

$$\text{Ttotal}_j := \text{Tstatic}_j + \text{Tdynamic}_j$$

Linear temperature profile leading from T2 to T3:

$$\text{Tlinear}_0 := \text{Tstatic}_0$$

$$\text{Tlinear}_j := \text{Tlinear}_0 + x_j \cdot \frac{\left(\text{Tstatic}_{\text{NumberIntervals}} - \text{Tstatic}_0\right)}{\left(x_{\text{NumberIntervals}} - x_0\right)}$$

Bulk temperature calculated using total temperature:

$$\text{Tbtotal} := \frac{\text{Ttotal}_0 + \text{Ttotal}_{\text{NumberIntervals}}}{2} \qquad \text{Tbtotal} - \text{T2} = 5.52\ \text{K}$$

Bulk temperature calculated using linear temperature:

$$\text{Tblinear} := \frac{\text{Tlinear}_0 + \text{Tlinear}_{\text{NumberIntervals}}}{2} \qquad \text{Tblinear} - \text{T2} = 2.04\ \text{K}$$

Bulk temperature calculated (integrated) using static temperature:

$$\text{Tbstatic} := \frac{\left[\frac{\text{Length}}{\text{NumberIntervals}} \cdot \left(\frac{\text{Tstatic}_0}{2} + \sum_{k=1}^{\text{NumberIntervals}-1} \text{Tstatic}_k + \frac{\text{Tstatic}_{\text{NumberIntervals}}}{2}\right)\right]}{\text{Length}}$$

$$\text{Tbstatic} - \text{T2} = 3.84\ \text{K}$$

$$\frac{Tbstatic + - Tblinear}{Tbtotal + - Tblinear} = 51.8\%$$

Tdynamic =

0
0.13
0.29
0.49
0.73
1.04
1.45
2.02
2.87
4.26
6.96

K

Tstatic – T2 =

0
0.97
1.92
2.82
3.69
4.48
5.17
5.71
5.96
5.67
4.08

K

Ttotal – T2 =

0
1.1
2.21
3.31
4.42
5.52
6.62
7.73
8.83
9.94
11.04

K

Tlinear – T2 =

0
0.41
0.82
1.22
1.63
2.04
2.45
2.86
3.27
3.67
4.08

K

Plot of Tstatic, Tdynamic and Ttotal as a function of dowstream location:

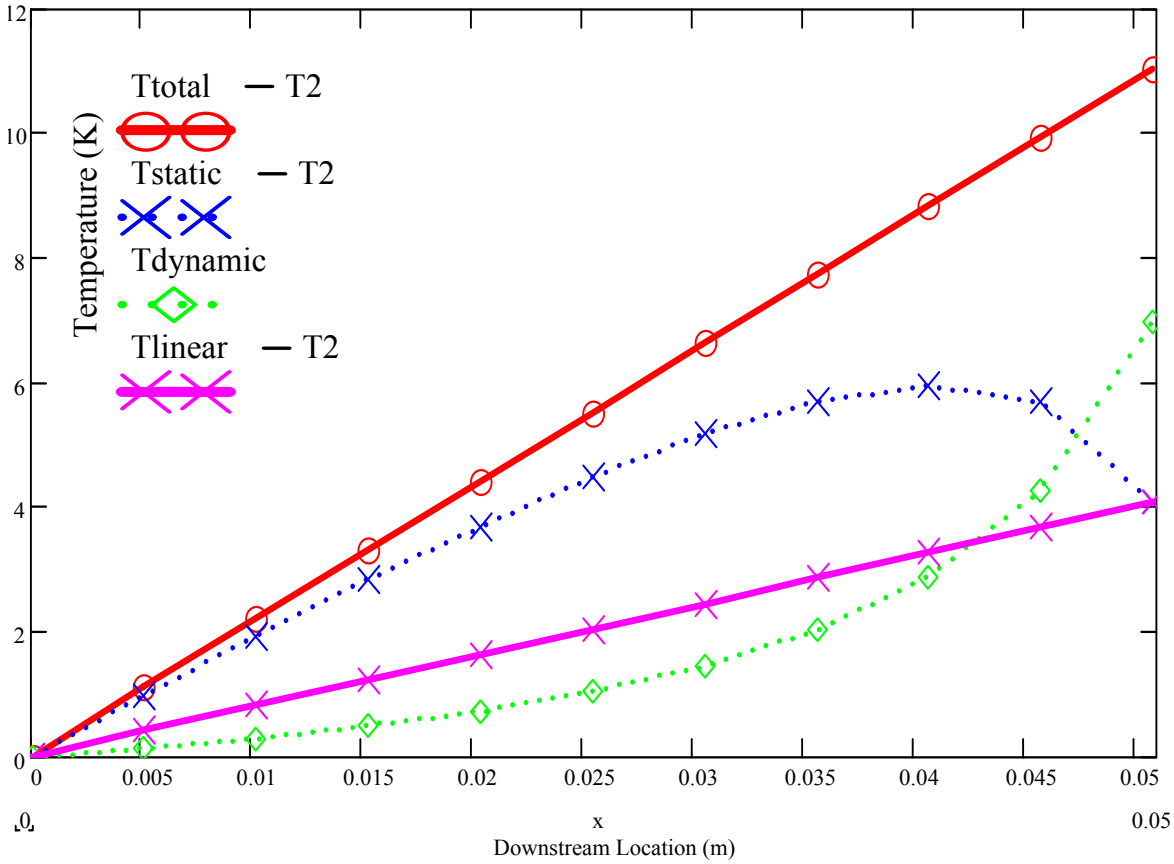

APPENDIX F: PARALLEL PLATE HEAT EXCHANGER MATHCAD CALCULATIONS

Pressure Loss Experiments

Experimental Data:

Notes: April 30th 2002
Five 500 um-thick stainless shims are used as spacers

$$Num := 8 \qquad scfm := \begin{bmatrix} 3 \\ 5 \\ 7 \\ 9 \\ 11 \\ 13 \\ 15 \\ 17 \end{bmatrix} \frac{ft^3}{min} \qquad T1 := \left[273.2 + \begin{bmatrix} 20.6 \\ 20.6 \\ 20.6 \\ 20.5 \\ 20.4 \\ 20.5 \\ 20.3 \\ 20.5 \end{bmatrix} \right] K \qquad T4 := \left[273.2 + \begin{bmatrix} 20.8 \\ 20.8 \\ 20.7 \\ 20.6 \\ 20.7 \\ 20.7 \\ 20.6 \\ 21.0 \end{bmatrix} \right] K$$

$$P1 := \left[14.7 + \begin{bmatrix} 2.5 \\ 5 \\ 8 \\ 12.5 \\ 16 \\ 21 \\ 28 \\ 34.5 \end{bmatrix} \right] psi \qquad P2 := \left[14.7 + \begin{bmatrix} 1 \\ 3 \\ 6 \\ 10 \\ 13 \\ 17 \\ 24 \\ 30 \end{bmatrix} \right] psi \qquad \Delta P23 := \begin{bmatrix} 0.5 \\ 1.5 \\ 2.6 \\ 3.8 \\ 4.6 \\ 5.6 \\ 6.6 \\ 7.5 \end{bmatrix} psi \qquad P4 := \left[14.7 + \begin{bmatrix} 0 \\ 0 \\ 3 \\ 5 \\ 7.5 \\ 11 \\ 16.5 \\ 22 \end{bmatrix} \right] psi$$

Coolant properties as a function of temperature:

$$Cp(T) := \text{linterp}(\text{Temperature\_data}, Cp\_data, T)\ \frac{J}{kg \cdot K}$$

$$\mu(T) := \text{linterp}(\text{Temperature\_data}, \mu\_data, T)\ N \cdot \frac{sec}{m^2}$$

$$k(T) := \text{linterp}(\text{Temperature\_data}, k\_data, T)\ \frac{W}{m \cdot K}$$

$$Pr(T) := \frac{\mu(T) \cdot Cp(T)}{k(T)}$$

$$Cp := 1000 \frac{J}{kg \cdot K}$$

Other properties and constants:

$$R := 287 \frac{J}{kg \cdot K}$$

$Po := 1\ atm$

$To := 294.3\ K$

$Tconversion := \frac{1}{K}$ (this constant used later to remove the units from the temperature)

Geometric parameters:

$Height := 0.5\ mm$ $Height2 := 0.5\ mm$ $Height3 := 0.5\ mm$

$Width := 2\ in$

$Length := 2\ in$

$TapToTapLength := 3\ in$

Calculations:

hydraulic diameter, flow cross sectional area in the HE:

$$Dh := 2 \cdot Height$$

$$CrossAreaFlow := Height \cdot Width$$

density at standard conditions, mass flow rate:

$$\rho o := \frac{Po}{R \cdot To}$$

$$massflowrate := scfm \cdot \rho o \qquad massflowrate = \begin{bmatrix} 0.0017 \\ 0.0028 \\ 0.004 \\ 0.0051 \\ 0.0062 \\ 0.0074 \\ 0.0085 \\ 0.0096 \end{bmatrix} \frac{kg}{s}$$

flow cross sectional area, temperature and velocity at location 2:

$$A2 := Width \cdot Height2$$

$$T2 := \frac{-2 \cdot Cp + \sqrt{(2 \cdot Cp)^2 - 4 \cdot \left(\frac{massflowrate \cdot R}{P2 \cdot A2}\right)^2 \cdot (-2 \cdot Cp \cdot T1)}}{2 \cdot \left(\frac{massflowrate \cdot R}{P2 \cdot A2}\right)^2} \qquad T2 - 273.2\,K = \begin{bmatrix} 19.3 \\ 17.7 \\ 16.5 \\ 15.7 \\ 14.8 \\ 14.5 \\ 14.9 \\ 15.3 \end{bmatrix} K$$

flow cross sectional area, pressure, temperature and velocity at location

$$A3 := Width \cdot Height3$$

$$P3 := P2 - \Delta P23$$

$$T3 := \frac{-2 \cdot Cp + \sqrt{(2 \cdot Cp)^2 - 4 \cdot \left(\frac{massflowrate \cdot R}{P3 \cdot A3}\right)^2 \cdot (-2 \cdot Cp \cdot T4)}}{2 \cdot \left(\frac{massflowrate \cdot R}{P3 \cdot A3}\right)^2} \qquad T3 - 273.2\,K = \begin{bmatrix} 19.4 \\ 17.3 \\ 15.3 \\ 14 \\ 12.7 \\ 12 \\ 12.9 \\ 13.6 \end{bmatrix} K$$

bulk temperature, pressure, density and velocity:

$$Tb := \frac{T2 + T3}{2} \qquad Tbconv := Tb \cdot Tconversion \qquad Tb - 273.2\,K = \begin{bmatrix} 19.3 \\ 17.5 \\ 15.9 \\ 14.9 \\ 13.7 \\ 13.3 \\ 13.9 \\ 14.5 \end{bmatrix} K$$

$$Pb := \frac{P2 + P3}{2}$$

$$\rho b := \frac{\overrightarrow{Pb}}{R \cdot Tb}$$

$$Vb := \frac{\overrightarrow{massflowrate}}{\rho b \cdot CrossAreaFlow}$$

pressure drop across the heat exchanger:

$$\Delta PHE := \Delta P23 \cdot \frac{Length}{TapToTapLength} \qquad \Delta PHE = \begin{bmatrix} 0.3 \\ 1 \\ 1.7 \\ 2.5 \\ 3.1 \\ 3.7 \\ 4.4 \\ 5 \end{bmatrix} psi$$

Friction Factor and Reynolds number:

$$f := \overrightarrow{\left[\frac{\Delta PHE}{\left(\frac{\rho b \cdot Vb^2}{2} \right)} \cdot \frac{Dh}{Length} \right]}$$

$$i := 0 .. (Num - 1)$$

$$Re_i := \frac{massflowrate_i \cdot Dh}{CrossAreaFlow \cdot \mu\left(Tbconv_i\right)}$$

$$Re = \begin{bmatrix} 3693 \\ 6184 \\ 8694 \\ 11209 \\ 13741 \\ 16260 \\ 18729 \\ 21195 \end{bmatrix} \qquad f = \begin{bmatrix} 0.026 \\ 0.031 \\ 0.031 \\ 0.032 \\ 0.029 \\ 0.029 \\ 0.032 \\ 0.032 \end{bmatrix}$$

Comparison between results and Incropera DeWitt Textbook:

Incropera's friction factor:

$fINCRO := 0.316 \cdot Re^{-0.25}$ (*valid for 0.5<Pr<2,000 and 3,000<Re<5,000,000)*

$$fINCRO = \begin{bmatrix} 0.041 \\ 0.036 \\ 0.033 \\ 0.031 \\ 0.029 \\ 0.028 \\ 0.027 \\ 0.026 \end{bmatrix}$$

Comparison Incropera and present results:

$$\overrightarrow{\left(\frac{fINCRO}{f}\right)} = \begin{bmatrix} 1.58 \\ 1.16 \\ 1.05 \\ 0.95 \\ 0.99 \\ 0.96 \\ 0.85 \\ 0.81 \end{bmatrix} \qquad \overrightarrow{\left(\frac{fINCRO}{f}\right)} - 1 = \begin{bmatrix} 58 \\ 16 \\ 5 \\ -5 \\ -1 \\ -4 \\ -15 \\ -19 \end{bmatrix} \%$$

Additional calculations:

Velocity, Mach number at location 2:

$$V2 := \overrightarrow{\frac{massflowrate \cdot T2 \cdot R}{P2 \cdot A2}} \qquad M2 := \overrightarrow{\left[\frac{V2}{\left[\sqrt{(1.4 \cdot R \cdot T2)}\right]}\right]} \qquad M2 = \begin{bmatrix} 0.15 \\ 0.22 \\ 0.27 \\ 0.29 \\ 0.31 \\ 0.32 \\ 0.3 \\ 0.3 \end{bmatrix}$$

Velocity, Mach number at location 3:

$$V3 := \overrightarrow{\frac{massflowrate \cdot T3 \cdot R}{P3 \cdot A3}} \qquad M3 := \overrightarrow{\left[\frac{V3}{\left[\sqrt{(1.4 \cdot R \cdot T3)}\right]}\right]} \qquad M3 = \begin{bmatrix} 0.16 \\ 0.24 \\ 0.3 \\ 0.34 \\ 0.37 \\ 0.39 \\ 0.37 \\ 0.36 \end{bmatrix}$$

Heat Transfer Experiments

Experimental Data:

Notes: May 23rd 2002
Five 500 um-thick stainless shims are used as spacers
100 um of thermally conductive silicone grease is applied

$$Num := 4 \qquad scfm := \begin{bmatrix} 4.0 \\ 8.0 \\ 12.0 \\ 16.0 \end{bmatrix} \frac{ft^3}{min} \qquad T1 := \begin{bmatrix} 273.2 + \begin{bmatrix} 20.1 \\ 18 \\ 18 \\ 18.2 \end{bmatrix} \end{bmatrix} K \qquad T4 := \begin{bmatrix} 273.2 + \begin{bmatrix} 55.5 \\ 37.9 \\ 31.8 \\ 28.7 \end{bmatrix} \end{bmatrix} K$$

$$P1 := \begin{bmatrix} 14.7 + \begin{bmatrix} 4.0 \\ 12 \\ 21 \\ 33 \end{bmatrix} \end{bmatrix} psi \qquad P2 := \begin{bmatrix} 14.7 + \begin{bmatrix} 3.0 \\ 10 \\ 18 \\ 30 \end{bmatrix} \end{bmatrix} psi \qquad \Delta P23 := \begin{bmatrix} 1.5 \\ 4.7 \\ 7.4 \\ 9.7 \end{bmatrix} psi \qquad P4 := \begin{bmatrix} 14.7 + \begin{bmatrix} 0 \\ 4 \\ 10 \\ 19 \end{bmatrix} \end{bmatrix} psi$$

$$Qelectric := \begin{bmatrix} 99 \\ 102 \\ 103 \\ 103 \end{bmatrix} W \qquad Tbot := \begin{bmatrix} 273.2 + \begin{bmatrix} 145.1 \\ 86.7 \\ 70.1 \\ 61.2 \end{bmatrix} \end{bmatrix} K \qquad Ttop := \begin{bmatrix} 273.2 + \begin{bmatrix} 147.5 \\ 89.1 \\ 72.4 \\ 63.5 \end{bmatrix} \end{bmatrix} K$$

Coolant properties as a function of temperature:

$Cp(T) := \text{linterp}(Temperature\_data, Cp\_data, T)\ \frac{J}{kg \cdot K}$

$\mu(T) := \text{linterp}(Temperature\_data, \mu\_data, T)\ N \cdot \frac{sec}{m^2}$

$k(T) := \text{linterp}(Temperature\_data, k\_data, T)\ \frac{W}{m \cdot K}$

$Pr(T) := \frac{\mu(T) \cdot Cp(T)}{k(T)}$

$Cp := 1000 \frac{J}{kg \cdot K}$

Other properties and constants:

$R := 287 \frac{J}{kg \cdot K}$

$kAl := 165 \frac{W}{m \cdot K}$

$kSS := 13.5 \frac{W}{m \cdot K}$

$ksilicone := 2.3 \frac{W}{m \cdot K}$

$Po := 1\ atm$

$To := 294.3\ K$

$Tconversion := \frac{1}{K}$ *(this constant is used later to remove the units from the temperature)*

Geometric parameters:

$Height := 0.5\ mm$ $Height2 := 0.5\ mm$ $Height3 := 0.5\ mm$

$Width := 2\ in$

Length := 2 in

distanceAl := .22 in

distanceSS := 0.1 in

distancetopbot := $\frac{3}{8}$ in

tcontact := 0.1 mm

Calculations:

hydraulic diameter, flow cross sectional area in the HE:

Dh := 2·Height

CrossAreaFlow := Height·Width

reference area for heat transfer

Aheat := Length·Width

density at standard conditions, mass flow rate:

$\rho o := \frac{Po}{R \cdot To}$

massflowrate := scfm·ρo

$$massflowrate = \begin{bmatrix} 0.0023 \\ 0.0045 \\ 0.0068 \\ 0.0091 \end{bmatrix} \circ \frac{kg}{s}$$

flow cross sectional area, temperature and velocity at location 2:

A2 := Width·Height2

$$T2 := \frac{-2 \cdot Cp + \overrightarrow{\sqrt{(2 \cdot Cp)^2 - 4 \cdot \left(\frac{massflowrate \cdot R}{P2 \cdot A2}\right)^2 \cdot (-2 \cdot Cp \cdot T1)}}}{2 \cdot \left(\frac{massflowrate \cdot R}{P2 \cdot A2}\right)^2} \qquad T2 - 273.2\,K = \begin{bmatrix} 18.2 \\ 14.3 \\ 13.2 \\ 13.7 \end{bmatrix} K$$

$$V2 := \overrightarrow{\left(\frac{massflowrate \cdot T2 \cdot R}{P2 \cdot A2}\right)} \qquad V2 = \begin{bmatrix} 61 \\ 86 \\ 98 \\ 95 \end{bmatrix} \circ \frac{m}{s}$$

flow cross sectional area, pressure, temperature and velocity at location 3

$$A3 := Width \cdot Height3$$

$$P3 := P2 - \Delta P23$$

$$T3 := \frac{-2\cdot Cp + \sqrt{\overrightarrow{(2\cdot Cp)^2 - 4\cdot\left(\frac{massflowrate\cdot R}{P3\cdot A3}\right)^2\cdot(-2\cdot Cp\cdot T4)}}}{2\cdot\left(\frac{massflowrate\cdot R}{P3\cdot A3}\right)^2} \qquad T3 - 273.2\,K = \begin{bmatrix} 52.7 \\ 31.5 \\ 23.3 \\ 20.9 \end{bmatrix} K$$

$$V3 := \overrightarrow{\left(\frac{massflowrate\cdot T3\cdot R}{P3\cdot A3}\right)} \qquad V3 = \begin{bmatrix} 75 \\ 113 \\ 130 \\ 125 \end{bmatrix} \circ \frac{m}{s}$$

total temperature at location 3 (location 2 is reference for velocity):

$$T3total := \overrightarrow{\left[T3 + \frac{1}{2\cdot Cp}\cdot\left(V3^2 - V2^2\right)\right]} \qquad T3total - 273.2\,K = \begin{bmatrix} 53.6 \\ 34.2 \\ 27 \\ 24.2 \end{bmatrix} K$$

total thermal resistance, heat exchanger wall temperature:

$$Rthermal := \frac{distanceAl}{kAl} + \frac{distanceSS}{kSS} + \frac{tcontact}{ksilicone} \qquad Rthermal = 2.7\cdot 10^{-4} \circ \frac{m^2\cdot K}{W}$$

$$Tw := Tbot - \frac{Qelectric}{Aheat}\cdot Rthermal \qquad Tw - 273.2\,K = \begin{bmatrix} 134.9 \\ 76.2 \\ 59.5 \\ 50.6 \end{bmatrix} K$$

bulk temperature, film temperature:

$$Tb := \frac{T2 + T3total}{2} \qquad Tbconv := Tb\cdot Tconversion \qquad Tb - 273.2\,K = \begin{bmatrix} 35.9 \\ 24.2 \\ 20.1 \\ 18.9 \end{bmatrix} K$$

$$Tf := \frac{Tw + Tb}{2} \qquad Tfconv := Tf\cdot Tconversion \qquad Tf - 273.2\,K = \begin{bmatrix} 85.4 \\ 50.2 \\ 39.8 \\ 34.8 \end{bmatrix} K$$

heat transferred by conduction to the top plate of the heat exchanger:

$$Qconduction := Aheat \cdot kAl \cdot \frac{(Ttop - Tbot)}{distancetopbot} \qquad Qconduction = \begin{bmatrix} 107 \\ 107 \\ 103 \\ 103 \end{bmatrix} \circ W \qquad \overrightarrow{\left(\frac{Qconduction}{Qelectric}\right)} = \begin{bmatrix} 108 \\ 105 \\ 100 \\ 100 \end{bmatrix} \circ \%$$

heat transferred by convection to the coolant:

$$Qconvection := \overrightarrow{(massflowrate \cdot Cp \cdot (T4 - T1))} \qquad Qconvection = \begin{bmatrix} 80 \\ 90 \\ 94 \\ 95 \end{bmatrix} \circ W \qquad \overrightarrow{\left(\frac{Qconvection}{Qelectric}\right)} = \begin{bmatrix} 81 \\ 88 \\ 91 \\ 92 \end{bmatrix} \circ \%$$

convective heat transfer coefficient for uniform heat flux (UHF) at wall:

$$Q := Qelectric$$

$$hUHF := \frac{\overrightarrow{Qelectric}}{Aheat \cdot (Tw - Tb)} \qquad hUHF = \begin{bmatrix} 388 \\ 760 \\ 1014 \\ 1259 \end{bmatrix} \circ \frac{W}{m^2 \cdot K}$$

Nusselt number for UHF and Reynolds number:

$$i := 0 .. (Num - 1)$$

$$NuUHF_i := \frac{(hUHF)_i \cdot Dh}{k\left(Tfconv_i\right)}$$

$$Re_i := \frac{massflowrate_i \cdot Dh}{CrossAreaFlow \cdot \mu\left(Tfconv_i\right)}$$

$$Re = \begin{bmatrix} 4206 \\ 9114 \\ 14023 \\ 18934 \end{bmatrix} \qquad NuUHF = \begin{bmatrix} 12.6 \\ 27.1 \\ 37.2 \\ 46.8 \end{bmatrix}$$

Comparison UHF results with Incropera DeWitt Textbook:

Incropera's friction factor and Nusselt number:

$$fINCRO := 0.316 \cdot Re^{-0.25}$$ (*valid for 0.5<Pr<2,000 and 3,000<Re<5,000,000)*

$$NuINCRO := \overrightarrow{\frac{\left(\frac{fINCRO}{8}\right) \cdot (Re - 1000) \cdot Pr(300)}{1 + 12.7 \cdot \left(\frac{fINCRO}{8}\right)^{\frac{1}{2}} \cdot \left(Pr(300)^{\frac{2}{3}} - 1\right)}} \qquad NuINCRO = \begin{bmatrix} 13.6 \\ 27.8 \\ 39.7 \\ 50.3 \end{bmatrix}$$

Comparison Incropera and present results:

$$\overrightarrow{\left(\frac{NuINCRO}{NuUHF}\right)} = \begin{bmatrix} 1.08 \\ 1.03 \\ 1.07 \\ 1.07 \end{bmatrix} \qquad \overrightarrow{\left(\frac{NuINCRO}{NuUHF}\right)} - 1 = \begin{bmatrix} 8 \\ 3 \\ 7 \\ 7 \end{bmatrix} \%$$

Additional calculations:

Mach number at location 2:

$$M2 := \overrightarrow{\left[\frac{V2}{\left[\sqrt{(1.4 \cdot R \cdot T2)}\right]}\right]} \qquad M2 = \begin{bmatrix} 0.18 \\ 0.25 \\ 0.29 \\ 0.28 \end{bmatrix}$$

Mach number at location 3:

$$M3 := \overrightarrow{\left[\frac{V3}{\left[\sqrt{(1.4 \cdot R \cdot T3)}\right]}\right]} \qquad M3 = \begin{bmatrix} 0.21 \\ 0.32 \\ 0.38 \\ 0.36 \end{bmatrix}$$

APPENDIX G: MICRO PIN FIN HEAT EXCHANGER MATHCAD CALCULATIONS

Pressure Loss Experiments

Experimental Data:

Notes: May 10th 2002
Use the parallel plate pressure experimental results from
April 30th 2002 to determine inlet and exit pressure drop

$$Num := 7 \qquad scfm := \begin{bmatrix} 3 \\ 5 \\ 7 \\ 9 \\ 11 \\ 13.5 \\ 15.5 \end{bmatrix} \frac{ft^3}{min} \qquad T1 := \begin{bmatrix} 273.2 + \begin{bmatrix} 20.3 \\ 20.0 \\ 19.9 \\ 19.9 \\ 20.1 \\ 20.1 \\ 20.1 \end{bmatrix} \end{bmatrix} K \qquad T4 := \begin{bmatrix} 273.2 + \begin{bmatrix} 20.5 \\ 21.1 \\ 20.5 \\ 20.4 \\ 20.0 \\ 19.7 \\ 19.7 \end{bmatrix} \end{bmatrix} K$$

$$P1 := \begin{bmatrix} 14.7 + \begin{bmatrix} 8.5 \\ 15 \\ 24 \\ 34.5 \\ 43 \\ 59 \\ 66 \end{bmatrix} \end{bmatrix} psi \qquad P2 := \begin{bmatrix} 14.7 + \begin{bmatrix} 7.5 \\ 14 \\ 23 \\ 33 \\ 41 \\ 56 \\ 64 \end{bmatrix} \end{bmatrix} psi \qquad \Delta P23 := \begin{bmatrix} 7.0 \\ 12.5 \\ 20.1 \\ 27.9 \\ 33.6 \\ 43.2 \\ 47.5 \end{bmatrix} psi \qquad P4 := \begin{bmatrix} 14.7 + \begin{bmatrix} 0 \\ 0 \\ 2 \\ 4 \\ 8 \\ 12 \\ 16.5 \end{bmatrix} \end{bmatrix} psi$$

Pressure results from Parallel Plate experiment on April 30 2002:

$$Rechannel := \begin{bmatrix} 3.693 \cdot 10^3 \\ 6.184 \cdot 10^3 \\ 8.694 \cdot 10^3 \\ 1.121 \cdot 10^4 \\ 1.374 \cdot 10^4 \\ 1.626 \cdot 10^4 \\ 1.873 \cdot 10^4 \\ 2.12 \cdot 10^4 \end{bmatrix} \qquad \Delta Pchannel := \begin{bmatrix} 0.5 \\ 1.5 \\ 2.6 \\ 3.8 \\ 4.6 \\ 5.6 \\ 6.6 \\ 7.5 \end{bmatrix} psi$$

Coolant properties as a function of temperature:

$$Cp(T) := \text{linterp}(\text{Temperature\_data}, Cp\_data, T)\ \frac{J}{kg \cdot K}$$

$$\mu(T) := \text{linterp}(\text{Temperature\_data}, \mu\_data, T)\ N \cdot \frac{sec}{m^2}$$

$$k(T) := \text{linterp}(\text{Temperature\_data}, k\_data, T)\ \frac{W}{m \cdot K}$$

$$Pr(T) := \frac{\mu(T) \cdot Cp(T)}{k(T)}$$

$$Cp := 1000 \frac{J}{kg \cdot K}$$

Other properties and constants:

$$R := 287 \frac{J}{kg \cdot K}$$

$$Po := 1\ atm$$

$$To := 294.3\ K$$

$$Tconversion := \frac{1}{K}$$ (this constant used later to remove the units from the temperature)

Geometric parameters:

$Height := 0.5\ mm$ $Height2 := 0.5\ mm$ $Height3 := 0.5\ mm$

$Width := 2\ in$

$Length := 2\ in$

$TapToTapLength := 3\ in$

Calculations:

hydraulic diameter, flow cross sectional area in the HE:

$Dh := 2 \cdot Height$

$CrossAreaFlow := Height \cdot Width$

density at standard conditions, mass flow rate:

$$\rho o := \frac{Po}{R \cdot To}$$

$massflowrate := scfm \cdot \rho o$

$$massflowrate = \begin{bmatrix} 0.0017 \\ 0.0028 \\ 0.004 \\ 0.0051 \\ 0.0062 \\ 0.0076 \\ 0.0088 \end{bmatrix} \frac{kg}{s}$$

flow cross sectional area, temperature and velocity at location 2:

$A2 := Width \cdot Height2$

$$T2 := \frac{-2 \cdot Cp + \sqrt{(2 \cdot Cp)^2 - 4 \cdot \left(\frac{massflowrate \cdot R}{P2 \cdot A2}\right)^2 \cdot (-2 \cdot Cp \cdot T1)}}{2 \cdot \left(\frac{massflowrate \cdot R}{P2 \cdot A2}\right)^2}$$

$$T2 - 273.2\,K = \begin{bmatrix} 19.6 \\ 18.9 \\ 18.6 \\ 18.6 \\ 18.7 \\ 18.8 \\ 18.7 \end{bmatrix} K$$

flow cross sectional area, pressure, temperature and velocity at location 3:

$A3 := Width \cdot Height3$

$P3 := P2 - \Delta P23$

$$T3 := \frac{-2 \cdot Cp + \sqrt{(2 \cdot Cp)^2 - 4 \cdot \left(\frac{massflowrate \cdot R}{P3 \cdot A3}\right)^2 \cdot (-2 \cdot Cp \cdot T4)}}{2 \cdot \left(\frac{massflowrate \cdot R}{P3 \cdot A3}\right)^2}$$

$$T3 - 273.2\,K = \begin{bmatrix} 19.1 \\ 17.6 \\ 14.9 \\ 13.1 \\ 11.4 \\ 11.3 \\ 11.1 \end{bmatrix} K$$

bulk temperature, pressure, density and velocity:

$$Tb := \frac{T2 + T3}{2} \qquad Tbconv := Tb \cdot Tconversion \qquad Tb - 273.2\,K = \begin{bmatrix} 19.3 \\ 18.3 \\ 16.7 \\ 15.9 \\ 15 \\ 15 \\ 14.9 \end{bmatrix} K$$

$$Pb := \frac{P2 + P3}{2}$$

$$\rho b := \frac{\overrightarrow{Pb}}{R \cdot Tb}$$

$$Vb := \frac{\overrightarrow{massflowrate}}{\rho b \cdot CrossAreaFlow}$$

pressure drop per unit length in entry and exit channel:

$$i := 0 .. (Num - 1)$$

$$Re_i := \frac{massflowrate_i \cdot Dh}{CrossAreaFlow \cdot \mu\left(Tbconv_i\right)}$$

$$\Delta PchannelPerUnitLength_i := \frac{linterp\left(Rechannel, \Delta Pchannel, Re_i\right)}{TapToTapLength}$$

pressure drop across the heat exchanger:

$$\Delta PHE := \Delta P23 - \Delta PchannelPerUnitLength \cdot (TapToTapLength - Length) \qquad \Delta PHE = \begin{bmatrix} 6.8 \\ 12 \\ 19.2 \\ 26.6 \\ 32.1 \\ 41.3 \\ 45.2 \end{bmatrix} psi$$

Friction Factor and Reynolds number:

$$f := \overrightarrow{\left[\frac{\Delta PHE}{\left(\frac{\rho b \cdot Vb^2}{2}\right)} \cdot \frac{Dh}{Length}\right]}$$

$$i := 0 .. (Num - 1)$$

$$Re_i := \frac{massflowrate_i \cdot Dh}{CrossAreaFlow \cdot \mu\left(Tbconv_i\right)}$$

$$Re = \begin{bmatrix} 3693 \\ 6172 \\ 8675 \\ 11180 \\ 13695 \\ 16806 \\ 19303 \end{bmatrix} \qquad f = \begin{bmatrix} 0.637 \\ 0.485 \\ 0.491 \\ 0.504 \\ 0.47 \\ 0.506 \\ 0.471 \end{bmatrix}$$

Additional calculations:

Velocity, Mach number at location 2:

$$V2 := \overrightarrow{\frac{massflowrate \cdot T2 \cdot R}{P2 \cdot A2}}$$

$$M2 := \overrightarrow{\left[\frac{V2}{\left[\sqrt{(1.4 \cdot R \cdot T2)}\right]}\right]} \qquad M2 = \begin{bmatrix} 0.11 \\ 0.14 \\ 0.15 \\ 0.15 \\ 0.16 \\ 0.15 \\ 0.16 \end{bmatrix}$$

Velocity, Mach number at location 3:

$$V3 := \overrightarrow{\frac{massflowrate \cdot T3 \cdot R}{P3 \cdot A3}}$$

$$M3 := \overrightarrow{\left[\frac{V3}{\left[\sqrt{(1.4 \cdot R \cdot T3)}\right]}\right]} \qquad M3 = \begin{bmatrix} 0.16 \\ 0.24 \\ 0.31 \\ 0.36 \\ 0.39 \\ 0.38 \\ 0.39 \end{bmatrix}$$

Heat Transfer Experiments

Experimental Data:

Notes: May 10th 2002
Experiments done in the order 12,8,4,6 scfm
100 um of thermally conductive silicone grease is applied

$$Num := 4 \qquad scfm := \begin{bmatrix} 4 \\ 8 \\ 12 \\ 16 \end{bmatrix} \frac{ft^3}{min} \qquad T1 := \begin{bmatrix} 273.2 + \begin{bmatrix} 20.5 \\ 20.3 \\ 20.4 \\ 20.6 \end{bmatrix} \end{bmatrix} K \qquad T4 := \begin{bmatrix} 273.2 + \begin{bmatrix} 58.7 \\ 40.4 \\ 34.1 \\ 31.5 \end{bmatrix} \end{bmatrix} K$$

$$P1 := \begin{bmatrix} 14.7 + \begin{bmatrix} 11 \\ 31.5 \\ 51 \\ 67 \end{bmatrix} \end{bmatrix} psi \qquad P2 := \begin{bmatrix} 14.7 + \begin{bmatrix} 10 \\ 30 \\ 49 \\ 65 \end{bmatrix} \end{bmatrix} psi \qquad \Delta P23 := \begin{bmatrix} 9.2 \\ 25.6 \\ 39 \\ 46.3 \end{bmatrix} psi \qquad P4 := \begin{bmatrix} 14.7 + \begin{bmatrix} 0 \\ 4 \\ 10 \\ 19 \end{bmatrix} \end{bmatrix} psi$$

$$Qelectric := \begin{bmatrix} 99 \\ 98 \\ 100 \\ 100 \end{bmatrix} W \qquad Tbot := \begin{bmatrix} 273.2 + \begin{bmatrix} 73.0 \\ 46.6 \\ 39.5 \\ 36.9 \end{bmatrix} \end{bmatrix} K \qquad Ttop := \begin{bmatrix} 273.2 + \begin{bmatrix} 75.5 \\ 49.0 \\ 41.7 \\ 39.2 \end{bmatrix} \end{bmatrix} K$$

Coolant properties as a function of temperature:

$$Cp(T) := \text{linterp}(Temperature\_data, Cp\_data, T)\ \frac{J}{kg \cdot K}$$

$$\mu(T) := \text{linterp}(Temperature\_data, \mu\_data, T)\ N \cdot \frac{sec}{m^2}$$

$$k(T) := \text{linterp}(Temperature\_data, k\_data, T)\ \frac{W}{m \cdot K}$$

$$Pr(T) := \frac{\mu(T) \cdot Cp(T)}{k(T)}$$

$$Cp := 1000 \frac{J}{kg \cdot K}$$

Other properties and constants:

$$R := 287 \frac{J}{kg \cdot K}$$

$$kAl := 165 \frac{W}{m \cdot K}$$

$$kNi := 90 \frac{W}{m \cdot K}$$

$$ksilicone := 2.3 \frac{W}{m \cdot K}$$

$$Po := 1\ atm$$

$$To := 294.3\ K$$

$$Tconversion := \frac{1}{K}$$ *(this constant is used later to remove the units from the temperature)*

Geometric parameters:

Dpost := 0.5 mm

Npost := 1580

Height := 0.5 mm Height2 := 0.5 mm Height3 := 0.5 mm

Width := 2 in

Length := 2 in

distanceAl := .22 in

distanceNi := 0.1 in

distancetopbot := $\frac{3}{8}$ in

tcontact := 0.1 mm

Calculations:

hydraulic diameter, flow cross sectional area in the HE:

Dh := 2·Height

CrossAreaFlow := Height·Width

reference area for heat transfer

Aheat := Length·Width

density at standard conditions, mass flow rate:

$\rho o := \frac{Po}{R \cdot To}$

massflowrate := scfm·ρo

$$massflowrate = \begin{bmatrix} 0.0023 \\ 0.0045 \\ 0.0068 \\ 0.0091 \end{bmatrix} \circ \frac{kg}{s}$$

flow cross sectional area, temperature and velocity at location 2:

$$A2 := Width \cdot Height2$$

$$T2 := \overrightarrow{\frac{-2\cdot Cp + \sqrt{(2\cdot Cp)^2 - 4\cdot\left(\frac{massflowrate\cdot R}{P2\cdot A2}\right)^2\cdot(-2\cdot Cp\cdot T1)}}{2\cdot\left(\frac{massflowrate\cdot R}{P2\cdot A2}\right)^2}} \qquad T2 - 273.2\,K = \begin{bmatrix}19.5\\19.1\\19.1\\19.1\end{bmatrix} K$$

$$V2 := \overrightarrow{\left(\frac{massflowrate\cdot T2\cdot R}{P2\cdot A2}\right)} \qquad V2 = \begin{bmatrix}44\\49\\51\\54\end{bmatrix}\circ\frac{m}{s}$$

flow cross sectional area, pressure, temperature and velocity at location 3:

$$A3 := Width \cdot Height3$$

$$P3 := P2 - \Delta P23$$

$$T3 := \overrightarrow{\frac{-2\cdot Cp + \sqrt{(2\cdot Cp)^2 - 4\cdot\left(\frac{massflowrate\cdot R}{P3\cdot A3}\right)^2\cdot(-2\cdot Cp\cdot T4)}}{2\cdot\left(\frac{massflowrate\cdot R}{P3\cdot A3}\right)^2}} \qquad T3 - 273.2\,K = \begin{bmatrix}55.6\\33.3\\25.1\\22.8\end{bmatrix} K$$

$$V3 := \overrightarrow{\left(\frac{massflowrate\cdot T3\cdot R}{P3\cdot A3}\right)} \qquad V3 = \begin{bmatrix}79\\119\\134\\132\end{bmatrix}\circ\frac{m}{s}$$

total temperature at location 3 (location 2 is reference for velocity):

$$T3total := \overrightarrow{\left[T3 + \frac{1}{2\cdot Cp}\cdot\left(V3^2 - V2^2\right)\right]} \qquad T3total - 273.2\,K = \begin{bmatrix}57.7\\39.2\\32.8\\30\end{bmatrix} K$$

total thermal resistance, heat exchanger wall temperature:

$$Rthermal := \frac{distanceAl}{kAl} + \frac{distanceNi}{kNi} + \frac{tcontact}{ksilicone} \qquad Rthermal = 1.1\cdot10^{-4}\circ\frac{m^2\cdot K}{W}$$

$$Tw := Tbot - \frac{Qelectric}{Aheat}\cdot Rthermal \qquad Tw - 273.2\,K = \begin{bmatrix}69\\42.6\\35.4\\32.8\end{bmatrix} K$$

bulk temperature, film temperature:

$$Tb := \frac{T2 + T3total}{2} \qquad Tbconv := Tb \cdot Tconversion \qquad Tb - 273.2\,K = \begin{bmatrix} 38.6 \\ 29.2 \\ 25.9 \\ 24.6 \end{bmatrix} K$$

$$Tf := \frac{Tw + Tb}{2} \qquad Tfconv := Tf \cdot Tconversion \qquad Tf - 273.2\,K = \begin{bmatrix} 53.8 \\ 35.9 \\ 30.7 \\ 28.7 \end{bmatrix} K$$

heat transferred by conduction to the top plate of the heat exchanger:

$$Qconduction := Aheat \cdot kAl \cdot \frac{(Ttop - Tbot)}{distancetopbot} \qquad Qconduction = \begin{bmatrix} 112 \\ 107 \\ 98 \\ 103 \end{bmatrix} \circ W \qquad \overrightarrow{\left(\frac{Qconduction}{Qelectric}\right)} = \begin{bmatrix} 113 \\ 109 \\ 98 \\ 103 \end{bmatrix} \circ \%$$

heat transferred by convection to the coolant:

$$Qconvection := \overrightarrow{(massflowrate \cdot Cp \cdot (T4 - T1))} \qquad Qconvection = \begin{bmatrix} 87 \\ 91 \\ 93 \\ 99 \end{bmatrix} \circ W \qquad \overrightarrow{\left(\frac{Qconvection}{Qelectric}\right)} = \begin{bmatrix} 87 \\ 93 \\ 93 \\ 99 \end{bmatrix} \circ \%$$

convective heat transfer coefficient for uniform heat flux (UHF) at wall:

$$Q := Qelectric$$

$$hUHF := \frac{\overrightarrow{Qelectric}}{Aheat \cdot (Tw - Tb)} \qquad hUHF = \begin{bmatrix} 1265 \\ 2830 \\ 4094 \\ 4702 \end{bmatrix} \circ \frac{W}{m^2 \cdot K}$$

Nusselt number for UHF and Reynolds number:

$$i := 0 .. (Num - 1)$$

$$NuUHF_i := \frac{(hUHF)_i \cdot Dh}{k\left(Tfconv_i\right)}$$

$$Re_i := \frac{massflowrate_i \cdot Dh}{CrossAreaFlow \cdot \mu\left(Tfconv_i\right)} \qquad Re = \begin{bmatrix} 4518 \\ 9440 \\ 14347 \\ 19227 \end{bmatrix} \qquad NuUHF = \begin{bmatrix} 44.7 \\ 104.9 \\ 154 \\ 177.8 \end{bmatrix}$$

Comparison UHF results with Chyu (1999):

Chyu's actual reference heat transfer area:

$$AChyu := Aheat - Npost \cdot \pi \cdot \frac{Dpost^2}{4} + \frac{Npost \cdot \pi \cdot Dpost \cdot Height}{2}$$

Chyu's Nusselt number using our length scales and surface reference:

(*valid for 6,000<Re<30,000)*

$a := 0.320 \qquad b := 0.583 \qquad SpanwiseRatio := 2.5$

$$NuChyu := a \cdot Re^{b} \cdot Pr(300)^{0.4} \cdot \left(\frac{Dpost}{Dh}\right)^{(b-1)} \cdot \left(\frac{SpanwiseRatio}{SpanwiseRatio - 1}\right)^{0.583} \cdot \frac{AChyu}{Aheat} \quad NuChyu = \begin{bmatrix} 75.8 \\ 116.5 \\ 148.7 \\ 176.4 \end{bmatrix}$$

Comparison Chyu(1999) and present results:

$$\overrightarrow{\left(\frac{NuChyu}{NuUHF}\right)} = \begin{bmatrix} 1.7 \\ 1.11 \\ 0.97 \\ 0.99 \end{bmatrix} \qquad \overrightarrow{\left(\frac{NuChyu}{NuUHF}\right)} - 1 = \begin{bmatrix} 70 \\ 11 \\ -3 \\ -1 \end{bmatrix} \%$$

Additional calculations:

Mach number at location 2:

$$M2 := \overrightarrow{\left[\frac{V2}{\left[\sqrt{(1.4 \cdot R \cdot T2)}\right]}\right]} \qquad M2 = \begin{bmatrix} 0.13 \\ 0.14 \\ 0.15 \\ 0.16 \end{bmatrix}$$

Mach number at location 3:

$$M3 := \overrightarrow{\left[\frac{V3}{\left[\sqrt{(1.4 \cdot R \cdot T3)}\right]}\right]} \qquad M3 = \begin{bmatrix} 0.22 \\ 0.34 \\ 0.39 \\ 0.38 \end{bmatrix}$$

APPENDIX H: MATHCAD MODEL PREDICTION FOR GAS TURBINE BLADE COOLING

Experimental Results of Nusselt number and Reynolds number:

Notes: Experiments done on May 10th 2002
Pin Fin Heat Exchanger

$Num := 4$

$$Re := \begin{bmatrix} 2617 \\ 5910 \\ 8602 \\ 9804 \end{bmatrix} \qquad Nu := \begin{bmatrix} 44.7 \\ 104.9 \\ 154 \\ 177.8 \end{bmatrix}$$

Coolant properties as a function of temperature:

$$Cp(T) := linterp(Temperature\_data, Cp\_data, T)\ \frac{J}{kg \cdot K}$$

$$\mu(T) := linterp(Temperature\_data, \mu\_data, T)\ N \cdot \frac{sec}{m^2}$$

$$k(T) := linterp(Temperature\_data, k\_data, T)\ \frac{W}{m \cdot K}$$

$$Pr(T) := \frac{\mu(T) \cdot Cp(T)}{k(T)}$$

Given properties:

$hexternal := 2500 \frac{W}{m^2 \cdot K}$ $\quad x1 := 1\ cm$ $\quad x3 := 3\ cm$

$Tc := 700\ K$ $\quad x2 := 2\ cm$ $\quad x4 := 4\ cm$

$Tg := 2200\ K$ $\quad x5 := 5\ cm$

$$Tb := \begin{bmatrix} 827 \\ 780 \\ 770 \\ 755 \end{bmatrix}$$ ***(Tb is calculated by iteration)***

Geometric parameters:

Dpost := 0.5 mm

Width := 1 m

Height := 0.5 mm

Calculations:

hydaulic diameter, flow cross sectional area in the HE:

Dh := 2·Height

CrossAreaFlow := Height·Width

convective heat transfer coefficient and mass flow rate of coolant:

i := 0.. (Num – 1)

$$heffective_i := \frac{Nu_i \cdot k\left(Tb_i\right)}{Dh} \qquad heffective = \begin{bmatrix} 2617 \\ 5910 \\ 8602 \\ 9804 \end{bmatrix} \circ \frac{W}{m^2 \cdot K}$$

$$massflowrate_i := \frac{Re_i \cdot CrossAreaFlow \cdot \mu\left(Tb_i\right)}{Dh} \qquad massflowrate = \begin{bmatrix} 0.049 \\ 0.107 \\ 0.155 \\ 0.175 \end{bmatrix} \circ \frac{kg}{s}$$

average overal heat transfer coefficient:

$$U := \frac{\overrightarrow{Width}}{\frac{1}{hexternal} + \frac{1}{heffective}} \qquad U = \begin{bmatrix} 1279 \\ 1757 \\ 1937 \\ 1992 \end{bmatrix} \circ \frac{W}{m \cdot K}$$

coolant temperature at various downstream locations:

$$Tcoolantx1 := Tg - (Tg - Tc)\ \overrightarrow{\exp\left(\frac{-U \cdot x1}{massflowrate \cdot Cp(Tb)}\right)} \qquad Tcoolantx1 = \begin{bmatrix} 1013 \\ 908 \\ 862 \\ 849 \end{bmatrix} K$$

$$Tcoolantx2 := Tg - (Tg - Tc)\ \overrightarrow{\exp\left(\frac{-U \cdot x2}{massflowrate \cdot Cp(Tb)}\right)} \qquad Tcoolantx2 = \begin{bmatrix} 1261 \\ 1087 \\ 1007 \\ 984 \end{bmatrix} K$$

$$Tcoolantx3 := Tg - (Tg - Tc)\ \overrightarrow{\exp\left(\frac{-U \cdot x3}{massflowrate \cdot Cp(Tb)}\right)} \qquad Tcoolantx3 = \begin{bmatrix} 1457 \\ 1242 \\ 1136 \\ 1105 \end{bmatrix} K$$

$$Tcoolantx4 := Tg - (Tg - Tc)\ \overrightarrow{\exp\left(\frac{-U \cdot x4}{massflowrate \cdot Cp(Tb)}\right)} \qquad Tcoolantx4 = \begin{bmatrix} 1612 \\ 1375 \\ 1251 \\ 1214 \end{bmatrix} K$$

$$Tcoolantx5 := Tg - (Tg - Tc)\ \overrightarrow{\exp\left(\frac{-U \cdot x5}{massflowrate \cdot Cp(Tb)}\right)} \qquad Tcoolantx5 = \begin{bmatrix} 1735 \\ 1489 \\ 1353 \\ 1312 \end{bmatrix} K$$

shroud temperature at various downstream locations:

$$Tshroudx1 := \overrightarrow{\frac{Tcoolantx1 \cdot heffective + Tg \cdot hexternal}{heffective + hexternal}} \qquad Tshroudx1 = \begin{bmatrix} 1593 \\ 1292 \\ 1163 \\ 1124 \end{bmatrix} K$$

$$Tshroudx2 := \overrightarrow{\frac{Tcoolantx2 \cdot heffective + Tg \cdot hexternal}{heffective + hexternal}} \qquad Tshroudx2 = \begin{bmatrix} 1720 \\ 1418 \\ 1275 \\ 1231 \end{bmatrix} K$$

$$Tshroudx3 := \overrightarrow{\frac{Tcoolantx3 \cdot heffective + Tg \cdot hexternal}{heffective + hexternal}} \qquad Tshroudx3 = \begin{bmatrix} 1820 \\ 1527 \\ 1375 \\ 1327 \end{bmatrix} K$$

$$Tshroudx4 := \overrightarrow{\frac{Tcoolantx4 \cdot heffective + Tg \cdot hexternal}{heffective + hexternal}} \qquad Tshroudx4 = \begin{bmatrix} 1899 \\ 1620 \\ 1464 \\ 1414 \end{bmatrix} K$$

$$Tshroudx5 := \overrightarrow{\frac{Tcoolantx5 \cdot heffective + Tg \cdot hexternal}{heffective + hexternal}} \qquad Tshroudx5 = \begin{bmatrix} 1962 \\ 1701 \\ 1544 \\ 1492 \end{bmatrix} K$$

cooling effectiveness at various downstream locations:

$$\varepsilon x1 := \overrightarrow{\left(\frac{Tg - Tshroudx1}{Tg - Tc}\right)} \qquad \varepsilon x1 = \begin{bmatrix} 40 \\ 61 \\ 69 \\ 72 \end{bmatrix} \%$$

$$\varepsilon x2 := \overrightarrow{\left(\frac{Tg - Tshroudx2}{Tg - Tc}\right)} \qquad \varepsilon x2 = \begin{bmatrix} 32 \\ 52 \\ 62 \\ 65 \end{bmatrix} \%$$

$$\varepsilon x3 := \overrightarrow{\left(\frac{Tg - Tshroudx3}{Tg - Tc}\right)} \qquad \varepsilon x3 = \begin{bmatrix} 25 \\ 45 \\ 55 \\ 58 \end{bmatrix} \%$$

$$\varepsilon x4 := \overrightarrow{\left(\frac{Tg - Tshroudx4}{Tg - Tc}\right)} \qquad \varepsilon x4 = \begin{bmatrix} 20 \\ 39 \\ 49 \\ 52 \end{bmatrix} \%$$

$$\varepsilon x5 := \overrightarrow{\left(\frac{Tg - Tshroudx5}{Tg - Tc}\right)} \qquad \varepsilon x5 = \begin{bmatrix} 16 \\ 33 \\ 44 \\ 47 \end{bmatrix} \%$$

APPENDIX I: CURVED METAL HEAT EXCHANGER MATHCAD CALCULATIONS

Heat Transfer Experiments

Recorded experimental values:

Temperatures:

$$Tg := \left[273.2 + \begin{bmatrix} 205.1 & 298.1 & 392.4 \\ 209.2 & 303.3 & 406.7 \\ 210.1 & 306.1 & 407.8 \\ 203.8 & 307.3 & 406.4 \end{bmatrix} \right] K \qquad Tw := \left[273.2 + \begin{bmatrix} 76.6 & 103.9 & 137.8 \\ 59.8 & 81.3 & 100.8 \\ 50.7 & 67.2 & 81.7 \\ 44.1 & 58.6 & 71.0 \end{bmatrix} \right] K$$

$$Tc := \left[273.2 + \begin{bmatrix} 25.5 & 26.0 & 28.0 \\ 24.3 & 25.3 & 26.3 \\ 23.0 & 24.3 & 25.2 \\ 22.6 & 24.3 & 24.8 \end{bmatrix} \right] K$$

Flow rates of gases and coolant:

$$massflowrategases := 0.202 \frac{kg}{s}$$

$$volumetricratecoolant := \begin{bmatrix} 4.0 \\ 7.0 \\ 10.7 \\ 14.5 \end{bmatrix} \frac{ft^3}{min} \qquad volumetricratecoolant = \begin{bmatrix} 1.888 \cdot 10^{-3} \\ 3.304 \cdot 10^{-3} \\ 5.05 \cdot 10^{-3} \\ 6.843 \cdot 10^{-3} \end{bmatrix} \frac{m^3}{s}$$

Constants, standard density:

$$R := 287\,\frac{J}{kg\cdot K}$$

$$Po := 1\ atm$$

$$To := 294.3\,K$$

$$\rho o := \frac{Po}{R\cdot To}$$

Cooling effectiveness ε:

$$\varepsilon := \overrightarrow{\left(\frac{Tg - Tw}{Tg - Tc}\right)} \qquad \varepsilon = \begin{bmatrix} 71.5 & 71.4 & 69.9 \\ 80.8 & 79.9 & 80.4 \\ 85.2 & 84.8 & 85.2 \\ 88.1 & 87.9 & 87.9 \end{bmatrix} \%$$

Coolant to mainstream gas mass flow rate ratio (MR):

$$volumetricrategases := \frac{massflowrategases}{\rho o}$$

$$MR := \overrightarrow{\left(\frac{volumetricratecoolant}{volumetricrategases}\right)} \qquad MR = \begin{bmatrix} 1.1 \\ 2 \\ 3 \\ 4.1 \end{bmatrix} \%$$

Coolant to mainstream gas temperature ratio (TR):

Complete TR matrix:

$$TR := \overrightarrow{\left(\frac{Tg}{Tc}\right)} \qquad TR = \begin{bmatrix} 1.601 & 1.909 & 2.21 \\ 1.622 & 1.931 & 2.27 \\ 1.632 & 1.947 & 2.282 \\ 1.613 & 1.951 & 2.281 \end{bmatrix}$$

Averaged columns of TR matrix:

$$j := 0..\,2$$

$$TRaveraged_j := \frac{\sum_{i=0}^{3} TR_{i,j}}{4} \qquad TRaveraged = \begin{bmatrix} 1.62 \\ 1.93 \\ 2.26 \end{bmatrix}$$

VITA

Christophe was born on August, 3rd 1973, in Le Creusot, France. In July 1991, he obtained his "Baccalauréat C" (High School degree in mathematics and physics) with distinctions.

In September 1991, he entered INSA de Lyon, a famous engineering school located in Lyon, France. He studied four of the five year college program with a specialty in Mechanical Engineering and Development. To complete his last year, he decided to become an exchange student in Mechanical Engineering at Louisiana State University (LSU) with International Student Exchange Program (ISEP) from 1995 to May 1996. He received his engineering college degree called "Diplôme d'ingénieur en Génie Mécanique et Développement" from INSA in July 1996 with honors.

Christophe enrolled a Master of Science program in Mechanical Engineering in January 1996 as a member of the Microsystems Engineering Team (μSET) at LSU with Dr. Kevin Kelly as graduate advisor. His research focused on manufacturing microstructures on the surface of a cylinder and testing the heat transfer enhancement. He earned his Master of Science degree on August, 1st 1997.

Following his French military service duty from August 1997 to May 1998, he returned to LSU in fall of 1998 to start a doctoral program in mechanical engineering with a minor in mathematics. His research project supervised by Dr. Kelly focused on the manufacturing and testing of a micro pin fin heat exchanger for a turbine blade. During

the course his doctoral studies, he was led to be the liaison with the U.S. Navy on microstructure testing and the liaison with Praxair on developing new plating alloys for MEMS. He will be awarded with his Doctor of Philosophy degree at the spring 2003 commencement.